

REPORT DOCUMENTATION PAGE			Form Approved OMB No. 0704-0188	
Public reporting burden for this collection of information is estimated to average 1 hour per response, including the time for reviewing instructions, searching existing data sources, gathering and maintaining the data needed, and completing and reviewing the collection of information. Send comments regarding this burden estimate or any other aspect of this collection of information, including suggestions for reducing this burden, to Washington Headquarters Services, Directorate for Information Operations and Reports, 1215 Jefferson Davis Highway, Suite 1204, Arlington, VA 22202-4302, and to the Office of Management and Budget, Paperwork Reduction Project (0704-0188), Washington, DC 20503.				
1. AGENCY USE ONLY (Leave blank)		2. REPORT DATE 20 Sep 95		3. REPORT TYPE AND DATES COVERED
4. TITLE AND SUBTITLE Adsorbed Water Layer Thickness On Quartz Fibers As A Function Of Humidity As Measured By Light Scattering			5. FUNDING NUMBERS	
6. AUTHOR(S)  Joseph Patrick Kendall				
7. PERFORMING ORGANIZATION NAME(S) AND ADDRESS(ES) AFIT Students Attending:  University of Arizona			8. PERFORMING ORGANIZATION REPORT NUMBER  95-081	
9. SPONSORING/MONITORING AGENCY NAME(S) AND ADDRESS(ES) DEPARTMENT OF THE AIR FORCE AFIT/CI 2950 P STREET, BLDG 125 WRIGHT-PATTERSON AFB OH 45433-7765			10. SPONSORING/MONITORING AGENCY REPORT NUMBER	
11. SUPPLEMENTARY NOTES				
12a. DISTRIBUTION/AVAILABILITY STATEMENT Approved for Public Release IAW AFR 190-1 Distribution Unlimited BRIAN D. GAUTHIER, MSgt, USAF Chief of Administration			12b. DISTRIBUTION CODE	
13. ABSTRACT (Maximum 200 words)				
<div style="position: absolute; top: 100px; left: 500px; border: 2px solid black; padding: 10px; transform: rotate(-5deg);"> DTIC SELECTED OCT 23 1995 G </div>				
<div style="font-size: 48px; font-weight: bold; margin-top: 20px;">19951019 136</div>				
DTIC QUALITY INSPECTED 8				
14. SUBJECT TERMS			15. NUMBER OF PAGES 95	
			16. PRICE CODE	
17. SECURITY CLASSIFICATION OF REPORT		18. SECURITY CLASSIFICATION OF THIS PAGE		19. SECURITY CLASSIFICATION OF ABSTRACT
				20. LIMITATION OF ABSTRACT

## GENERAL INSTRUCTIONS FOR COMPLETING SF 298

The Report Documentation Page (RDP) is used in announcing and cataloging reports. It is important that this information be consistent with the rest of the report, particularly the cover and title page. Instructions for filling in each block of the form follow. It is important to *stay within the lines* to meet *optical scanning requirements*.

### Block 1. Agency Use Only (Leave blank).

**Block 2. Report Date.** Full publication date including day, month, and year, if available (e.g. 1 Jan 88). Must cite at least the year.

**Block 3. Type of Report and Dates Covered.** State whether report is interim, final, etc. If applicable, enter inclusive report dates (e.g. 10 Jun 87 - 30 Jun 88).

**Block 4. Title and Subtitle.** A title is taken from the part of the report that provides the most meaningful and complete information. When a report is prepared in more than one volume, repeat the primary title, add volume number, and include subtitle for the specific volume. On classified documents enter the title classification in parentheses.

**Block 5. Funding Numbers.** To include contract and grant numbers; may include program element number(s), project number(s), task number(s), and work unit number(s). Use the following labels:

<b>C</b> - Contract	<b>PR</b> - Project
<b>G</b> - Grant	<b>TA</b> - Task
<b>PE</b> - Program Element	<b>WU</b> - Work Unit Accession No.

**Block 6. Author(s).** Name(s) of person(s) responsible for writing the report, performing the research, or credited with the content of the report. If editor or compiler, this should follow the name(s).

**Block 7. Performing Organization Name(s) and Address(es).** Self-explanatory.

**Block 8. Performing Organization Report Number.** Enter the unique alphanumeric report number(s) assigned by the organization performing the report.

**Block 9. Sponsoring/Monitoring Agency Name(s) and Address(es).** Self-explanatory.

**Block 10. Sponsoring/Monitoring Agency Report Number.** (If known)

**Block 11. Supplementary Notes.** Enter information not included elsewhere such as: Prepared in cooperation with...; Trans. of...; To be published in.... When a report is revised, include a statement whether the new report supersedes or supplements the older report.

**Block 12a. Distribution/Availability Statement.** Denotes public availability or limitations. Cite any availability to the public. Enter additional limitations or special markings in all capitals (e.g. NOFORN, REL, ITAR).

**DOD** - See DoDD 5230.24, "Distribution Statements on Technical Documents."

**DOE** - See authorities.

**NASA** - See Handbook NHB 2200.2.

**NTIS** - Leave blank.

### Block 12b. Distribution Code.

**DOD** - Leave blank.

**DOE** - Enter DOE distribution categories from the Standard Distribution for Unclassified Scientific and Technical Reports.

**NASA** - Leave blank.

**NTIS** - Leave blank.

**Block 13. Abstract.** Include a brief (*Maximum 200 words*) factual summary of the most significant information contained in the report.

**Block 14. Subject Terms.** Keywords or phrases identifying major subjects in the report.

**Block 15. Number of Pages.** Enter the total number of pages.

**Block 16. Price Code.** Enter appropriate price code (*NTIS only*).

**Blocks 17. - 19. Security Classifications.** Self-explanatory. Enter U.S. Security Classification in accordance with U.S. Security Regulations (i.e., UNCLASSIFIED). If form contains classified information, stamp classification on the top and bottom of the page.

**Block 20. Limitation of Abstract.** This block must be completed to assign a limitation to the abstract. Enter either UL (unlimited) or SAR (same as report). An entry in this block is necessary if the abstract is to be limited. If blank, the abstract is assumed to be unlimited.

**ADSORBED WATER LAYER THICKNESS  
ON QUARTZ FIBERS  
AS A FUNCTION OF HUMIDITY  
AS MEASURED BY LIGHT SCATTERING**

by

2LT Joseph Patrick Kendall, USAF

A Thesis Submitted to the Faculty of the

DEPARTMENT OF PHYSICS

In Partial Fulfillment of the Requirements

For the Degree of

MASTER OF SCIENCE

In the Graduate College

THE UNIVERSITY OF ARIZONA

1995

Accession For	
NTIS CRA&I	<input checked="" type="checkbox"/>
DTIC TAB	<input type="checkbox"/>
Unannounced	<input type="checkbox"/>
Justification	
By	
Distribution /	
Availability Codes	
Dist	Avail and/or Special
A-1	

## STATEMENT BY AUTHOR

This thesis has been submitted in partial fulfillment of requirements for an advanced degree at the University of Arizona and is deposited in the University Library to be made available to borrowers under the rules of the library. In addition, a copy is being maintained at the Air Force Institute of Technology in fulfillment of my academic agreement with the United States Air Force.

Brief quotations from this thesis are allowable without special permission, provided that accurate acknowledgment of the source is made. Requests for permission for extended quotation from or reproduction of thesis manuscript in whole or in part may be granted by the head of the major department or the Dean of the Graduate College when in his or her judgment the proposed use of the material is in the interests of scholarship. In all other instances, however, permission must be obtained from the author or the Air Force Institute of Technology.

SIGNED: *Paul H. Bickel, 307, 2547*

## APPROVAL BY THESIS DIRECTOR

This thesis has been approved on the date shown below:

*William S. Bickel*  
William S. Bickel  
Professor of Physics

*Aug 3/95*  
Date

## ACKNOWLEDGMENTS

Dr. William Bickel, my thesis advisor, was a constant source of support, advise, patience, and wisdom. I do not like to think about how things might have turned out without him. I would recommend his tutelage to anyone considering the University of Arizona as a postgraduate school for physics. He is one of a kind.

On the technical side, I would also like to thank Dr. Stanley Bashkin and Dr. Ke-Chiang Hsieh, who offered their valuable time to read and comment on this paper; Dr. James Dugan, who gave a great deal of advise on the equipment, experimentation in general, and good restaurants in town; and John Patteson, who designed the circuit for the Vaisala probe. Thanks also goes to the Air Force Institute of Technology, who funded my year-long Master's program.

On the social side, ..... did I have one of those? Wildcat Rugby and OPRFC helped me stay sane, as did Mike, Jim, Robert, Dave and everyone else here in Arizona (hey, Megan, how about that nanometer?). Thanks also to mom & dad, Lew, Kyleen & Mary, Padre, the lunch table gang,  $\Sigma\Delta T$ , Ed (suffering similarly in Canada, eh?), and everyone else who'll probably be mad that I didn't mention them in this certain-to-be-widely-read document.

Finally, as always, thanks to God, for everything.

## TABLE OF CONTENTS

<b>LIST OF FIGURES .....</b>	<b>5</b>
<b>ABSTRACT .....</b>	<b>9</b>
<b>1. INTRODUCTION .....</b>	<b>10</b>
<b>2. LIGHT SCATTERING .....</b>	<b>13</b>
2.1 Diffraction and Scattering .....	13
2.2 Polarization Relations .....	16
2.3 Stokes Vectors .....	17
2.4 Mueller Matrices .....	21
<b>3. THE POLAR NEPHELOMETER .....</b>	<b>28</b>
3.1 Overview .....	28
3.2 The Photoelastic Modulator .....	30
3.3 The Lock-In Amplifier .....	33
3.4 Nephelometer Calibration .....	34
<b>4. THE SCATTERER .....</b>	<b>36</b>
4.1 Fiber Manufacture .....	36
4.2 Experiment versus Theory for Five Fibers .....	39
<b>5. ADSORPTION AND HUMIDITY .....</b>	<b>43</b>
5.1 Adsorption Theory .....	43
5.2 The Humidity Chamber .....	50
<b>6. THE MEASUREMENTS .....</b>	<b>55</b>
6.1 The Thick Fiber (Fiber F, 2.460 $\mu\text{m}$ ) .....	56
6.2 The Intermediate Fibers (Fibers C, 1.3525 $\mu\text{m}$ and D, 1.3890 $\mu\text{m}$ ) .....	70
6.3 The Thin Fiber (Fiber X, 0.6280 $\mu\text{m}$ ) .....	81
<b>7. CONCLUSION .....</b>	<b>89</b>
<b>REFERENCES .....</b>	<b>94</b>

## LIST OF FIGURES

Figure 2.1 Diagram of Diffraction Setup .....	14
Figure 2.2 Diffraction versus Scattering Intensity Patterns .....	15
Figure 2.3 Optics Combinations for the Experimental Mueller Scattering Matrix .....	26
Figure 3.1 Experimental Setup of the Polar Nephelometer .....	29
Figure 4.1 Diagram of the Fiber Mounting Procedure .....	38
Figure 4.2 Fiber K, Experiment vs. Theoretical 0.2305 $\mu\text{m}$ Fiber .....	40
Figure 4.3 Fiber A, Experiment vs. Theoretical 0.2900 $\mu\text{m}$ Fiber .....	40
Figure 4.4 Fiber E, Experiment vs. Theoretical 0.4415 $\mu\text{m}$ Fiber .....	41
Figure 4.5 Fiber D, Experiment vs. Theoretical 0.7305 $\mu\text{m}$ Fiber .....	41
Figure 4.6 Fiber C, Experiment vs. Theoretical 1.3525 $\mu\text{m}$ Fiber .....	42
Figure 5.1 Change in Gibbs Free Energy versus Water Droplet Radius .....	44
Figure 5.2 Curve for the Kelvin Equation .....	45
Figure 5.3 Curves Solving the Köhler Equation for NaCl and $(\text{NH}_4)_2\text{SO}_4$ .....	46
Figure 5.4 Water Layer Thickness versus Relative Humidity for a Planar Surface and a Thin Quartz Fiber .....	48
Figure 5.5 Scattering Curves of a Theoretical 1 $\mu\text{m}$ Quartz Fiber with 3nm and 6nm Water Sheath Thicknesses .....	49
Figure 5.6 Scattering Curves of a Theoretical 1 $\mu\text{m}$ Quartz Fiber with 10nm Sheath of $n = 1.3130$ Water and $n = 1.3330$ Water .....	49
Figure 5.7 Diagram of Humidity Chamber .....	52

Figure 5.8 Response of the Vaisala Humidity Probe .....	53
Figure 6.1.1 The Four Experimental Scattering Curves for Test Fiber F .....	57
Figure 6.1.2 The Four Theoretical Scattering Curves for a 2.460 $\mu\text{m}$ Quartz Fiber .....	57
Figure 6.1.3 The Four Theoretical Scattering Curves for a 2.460 $\mu\text{m}$ Quartz Fiber with No Cladding, a 2.5 nm and a 5.0 nm Thick Water Layer .....	58
Figure 6.1.4 The Experimental $S_{12}^*$ Scattering Curves for Fiber F Cleaned in Acetone and Dipped in Water .....	58
Figure 6.1.5 The Four Theoretical Curves for Changes in Total Intensity and Percent Polarization at a Fixed Angle as a Function of Water Layer Thickness on a 2.460 $\mu\text{m}$ Quartz Fiber .....	61
Figure 6.1.6 The Experimental $S_{12}^*$ Scattering Curves for Fiber F Cleaned in Ace- tone and Exposed to High Static Humidity .....	61
Figure 6.1.7 The Four Experimental Scattering Curves for Fiber F Exposed to 0% RH and 95% RH .....	62
Figure 6.1.8 The Four Experimental Scattering Curves for Fiber F Exposed to 0% RH Initially and 0% RH After Three Consecutive 95% RH Exposures .....	62
Figure 6.1.9 The Experimental $S_{12}^*$ Scattering Curves for Fiber F Exposed to 37% RH and 93% RH (Second Test) .....	65
Figure 6.1.10 The Experimental $S_{12}^*$ Scattering Curves for Fiber F Exposed to 37% RH and 96% RH (Second Test) .....	65
Figure 6.1.11 The Experimental $S_{12}^*$ Scattering Curves for Fiber F Exposed to 37% RH and 40% RH after a 96% RH Exposure (Second Test) .....	66
Figure 6.1.12 The $S_{12}^*$ Percent Polarization Response of Fiber F at $\theta = 88^\circ$ to Variable Humidities .....	68
Figure 6.1.13 The Corrected $S_{12}^*$ Percent Polarization Response of Fiber F at $\theta = 88^\circ$ to Variable Humidities .....	69
Figure 6.1.14 The Corrected $S_{12}^*$ Percent Polarization Response of Fiber F at $\theta = 170^\circ$ to Variable Humidities (Second Test) .....	69

Figure 6.1.15 The Corrected $S_{12}^*$ Percent Polarization Response of Fiber F at $\theta = 170^\circ$ to Variable Flow Rates .....	70
Figure 6.2.1 The Experimental $S_{12}^*$ Scattering Curve for Test Fiber D .....	71
Figure 6.2.2 The Theoretical $S_{12}^*$ Scattering Curve for a 1.3890 $\mu\text{m}$ Quartz Fiber .....	71
Figure 6.2.3 The Experimental $S_{12}^*$ Scattering Curves for Fiber D Cleaned in Acetone and Dipped in Water .....	73
Figure 6.2.4 The Theoretical $S_{12}^*$ Scattering Curves for a 1.3890 $\mu\text{m}$ Quartz Fiber with No Cladding, a 2.5 nm and a 5.0 nm Thick Water Layer .....	73
Figure 6.2.5 The Theoretical $S_{12}^*$ Scattering Curves for a 1.3740 $\mu\text{m}$ Quartz Fiber with No Cladding and a 10 nm Thick Water Layer .....	74
Figure 6.2.6 The Experimental $S_{12}^*$ Scattering Curves for Fiber D Cleaned in Acetone and Exposed to High Static Humidity .....	74
Figure 6.2.7 The Four Experimental Scattering Curves for Fiber C Exposed to 15% RH and 96.5% RH. ....	76
Figure 6.2.8 The Four Experimental Scattering Curves for Fiber C Exposed to 15% RH Initially and 15% RH After Two Consecutive 96.5% RH Exposures .....	76
Figure 6.2.9 The Four Theoretical Scattering Curves for a 1.3525 $\mu\text{m}$ Quartz Fiber with No Cladding, a 2.5 nm and a 5.0 nm Thick Water Layer .....	77
Figure 6.2.10 The Experimental $S_{12}^*$ Scattering Curves for Fiber D Exposed to 28% RH and 98.5% RH .....	77
Figure 6.2.11 The Experimental $S_{12}^*$ Scattering Curves for Fiber D at 20% Initially and 37% RH After a 98.5% RH Exposure .....	78
Figure 6.2.12 The $S_{12}^*$ Percent Polarization Response of Fiber C at $\theta = 131^\circ$ to Variable Humidities .....	78
Figure 6.2.13 The Corrected $S_{12}^*$ Percent Polarization Response of Fiber C at $\theta = 131^\circ$ to Variable Humidities .....	80
Figure 6.2.14 The Corrected $S_{12}^*$ Percent Polarization Response of Fiber D at $\theta = 170^\circ$ to Variable Humidities .....	80

Figure 6.2.15 The Corrected $S_{12}^*$ Percent Polarization Response of Fiber D at $\theta = 170^\circ$ to Variable Flow Rates .....	81
Figure 6.3.1 The Four Experimental Scattering Curves for Test Fiber X .....	83
Figure 6.3.2 The Four Theoretical Scattering Curves for a 0.6280 $\mu\text{m}$ Quartz Fiber .....	83
Figure 6.3.3 The Experimental $S_{12}^*$ Scattering Curves for Fiber X Cleaned in Acetone and Dipped in Water .....	84
Figure 6.3.4 The Theoretical $S_{12}^*$ Scattering Curves for a 0.6415 $\mu\text{m}$ Quartz Fiber with No Cladding, a 2.5 nm and a 5.0 nm Water Layer .....	84
Figure 6.3.5 The Theoretical $S_{12}^*$ Scattering Curves for a 0.6415 $\mu\text{m}$ Quartz Fiber with No Cladding and a 10 nm Water Layer .....	85
Figure 6.3.6 The Experimental $S_{12}^*$ Scattering Curves for Fiber X Cleaned in Acetone and Exposed to High Static Humidity .....	85
Figure 6.3.7 The Experimental $S_{12}^*$ Scattering Curves for Fiber X Exposed to 21%RH and 98% RH .....	86
Figure 6.3.8 The Experimental $S_{12}^*$ Scattering Curves for Fiber X at 20% RH Initially and 18% RH After a 98% RH Exposure .....	86
Figure 6.3.9 The Corrected $S_{12}^*$ Percent Polarization Response of Fiber X at $\theta = 85^\circ$ to Variable Humidities .....	88
Figure 6.3.10 The Corrected $S_{12}^*$ Percent Polarization Response of Fiber X at $\theta = 85^\circ$ to Variable Flow Rates .....	88
Figure 7.1 Adsorbed Water Layer Thickness as a Function of Relative Humidity for a Planar Surface and Quartz Fibers of Different Radii .....	90
Figure 7.2 Summary of Findings Involving Three Sizes of Test Fibers Receiving Water Sheaths by Various Means .....	91

## ABSTRACT

This paper applies the Mueller scattering matrix for cylindrical quartz fibers to determine the buildup of thin water sheaths on the fibers as a function of humidity. We created four quartz fibers of various sizes and used a controlled-humidity environment to establish a relationship between relative humidity and water sheath thickness. We determined the thickness by measuring a particular Mueller scattering matrix at a single angle and relating changes in polarized light scattering ( $S_{ij}$ ) directly to the thickness of the water layer. We report an accelerated growth of a water sheath on quartz fibers at humidities above 90% and an irregular relationship between the fiber radius and the maximum size for a water layer.

## CHAPTER 1

### INTRODUCTION

Light scattering is an effective technique for determining many optical and geometric characteristics of microscopic systems. Precise measurements can be made without destroying the sample. Experimentalists have been able to observe new phenomena by measuring the critical elements of the Mueller scattering matrix and comparing the elements to theoretical results. Bickel and Stafford (1980) scattered laser light off of bacteria to determine their cause of death. Bickel, Davidson, *et al.* (1976) observed spores and established their classification by their scattering signals alone, and in 1984 Gilliar, Bickel, and Bailey observed the microscopic response of excited muscle fiber bundles in frogs. Clearly, this technique has great potential for revealing properties of objects which cannot be seen with a microscope.

Airborne particles are a concern in many areas. Pollen, for instance, is a plague for allergy-prone individuals when it becomes plentiful in the spring. Dust particles can be catastrophic to VLSI (very large scale integration) laboratories in their attempt to concentrate as much circuitry as possible onto a silicon wafer. Why these particles adhere to surfaces is still a mystery. The attractive force could be a consequence of static electricity or a type of Van-der-Waals force which can easily be orders of magnitude greater than the weight of the particle.

Water vapor also falls into this category. When water molecules condense onto a surface, they build up at a certain rate determined by factors such as temperature, pressure, and

humidity, and just how much builds up is an important question to laboratory technicians, meteorologists, aviators, and others who work in or with high-humidity environments.

This question was recently addressed in an experiment involving the adhesion force between two crossed fibers as they are pulled apart in a given humidity. Wentzel (1994) found that the fibers will gain layers of water vapor in high-humidity environments. In his experiments, these layers produced a meniscus between two crossed fibers as they were pulled apart; the meniscus increased the amount of force required to separate the fibers. In addition, he showed that the radius of a thin cylindrical fiber in a high humidity environment significantly increased due to adsorbed water layers. Our experiment extends these findings by determining the response of different sizes of fibers to humidity.

In the experiment, the beam from a helium cadmium laser is prepared to a definite polarization state and directed toward the fiber. The light scattered from the fiber passes through another polarizer and then enters a photomultiplier tube (PMT). The PMT measures the light scattered from the fibers as a function of scattering angle  $\theta$ . These scattering patterns are compared to the theoretical solutions to Maxwell's equations for a cylindrical fiber to determine the radius. Details of the experiment are discussed in the following chapters. Chapter Two introduces Stokes vectors and Mueller matrices, the mathematical conventions which describe polarized light and the scatterer. Chapter Three explains the measurement device, the polar nephelometer. Chapter Four discusses the preparation of the quartz fibers for use in the experiments. Chapter Five discusses elementary theory on humidity and water

adsorption, and describes way we controlled relative humidity. The measurements are presented in the Chapter Six and discussed in the conclusion.

## CHAPTER 2

### LIGHT SCATTERING

#### 2.1 Diffraction and Scattering

Coherent radiation incident upon an aperture whose width approaches that of the radiation wavelength will produce a diffraction pattern in the far field which is the Fourier transform of the aperture. This phenomenon is the result of wavefront interference due to the influence of the edges of the aperture. We obtain a solution by solving for the Green's function set at zero along the aperture plane except for the aperture itself. After applying approximations that assume an observation point far from the aperture, the solution for the intensity was shown by Barrett (1994) to be

$$\begin{aligned}
 I_z(\mathbf{r}) &= |E_z(\mathbf{r})|^2 \approx \frac{1}{\lambda^2 z^2} \left| \int_{\infty} d^2 \mathbf{r}_o \exp\left(\frac{-2\pi i(\mathbf{r} \cdot \mathbf{r}_o)}{z\lambda}\right) E_o(\mathbf{r}_o) \right|^2 \\
 &= \frac{1}{\lambda^2 z^2} \left| \mathfrak{F} \left\{ E_o \left( \frac{\mathbf{r}}{z\lambda} \right) \right\} \right|^2
 \end{aligned}$$

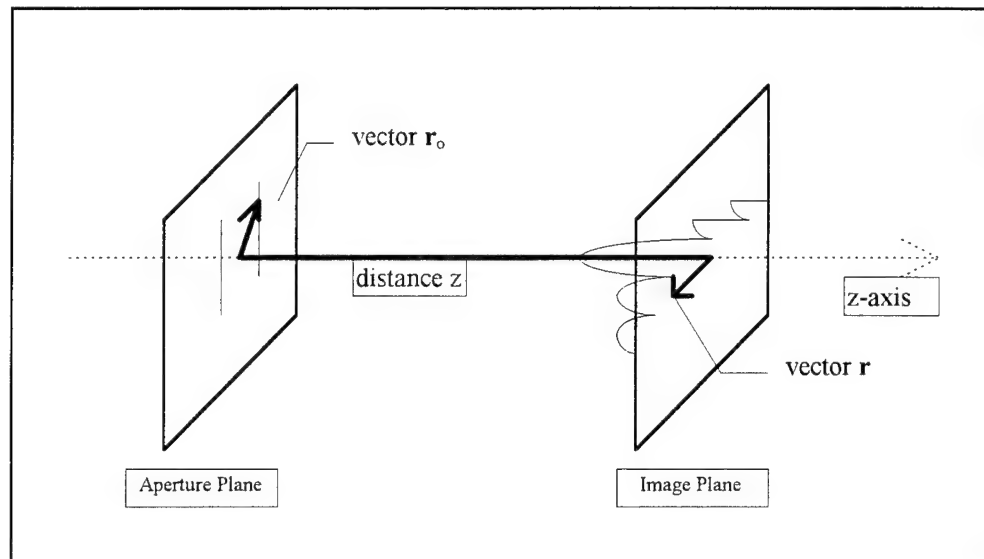


Figure 2.1. Diagram of Diffraction Setup. The labeled parts of the figure correspond to the diffraction equation on the previous page.

In the previous equations,  $\mathbf{r}$  is the vector from the beam propagation axis to a point in the image plane,  $\mathbf{r}_0$  is the vector from the beam propagation axis to a point in the aperture plane,  $\lambda$  is the wavelength of the incident radiation,  $z$  is the distance from the aperture plane to the image plane, and  $\mathbf{E}_0$  is the electric field immediately beyond the aperture (see Figure 2.1 above). The Fourier transform of the weighted electric field vector gives the "image" seen in the far field. Applying this to a single slit (represented in equation form as a rect function) gives the well-known  $(\sin x / x)^2$  intensity solution for Fraunhofer diffraction. The equation also gives the solution for Young's double-slit diffraction experiment when the single rect function is replaced by two rect functions in one dimension.

Scattering is similar to diffraction, but differs mainly because the target is three instead of two dimensional, the index of refraction of the target is not that of air, and the target can be absorbing. Therefore, while the scattering pattern is still a Fourier transform of the target, it is

far more complex than a diffraction pattern. Maxwell's equations predict how light will scatter off a quartz fiber, if that fiber is perfectly cylindrical. Figure 2.2 (taken from Gilliar, 1986) shows the difference between the theoretical scattering patterns produced by a 1  $\mu\text{m}$  slit and a 1  $\mu\text{m}$  quartz cylindrical fiber. The diffraction pattern extends only 90 degrees about the aperture, while the scattering pattern extends through all 180° (into all  $4\pi$  steradians). Slit diffraction has minima which are zero, but the scattering pattern does not. Diffraction data can give the geometry of the target. For example, the distance between maxima or minima in the single slit experiment gives the width of the slit.

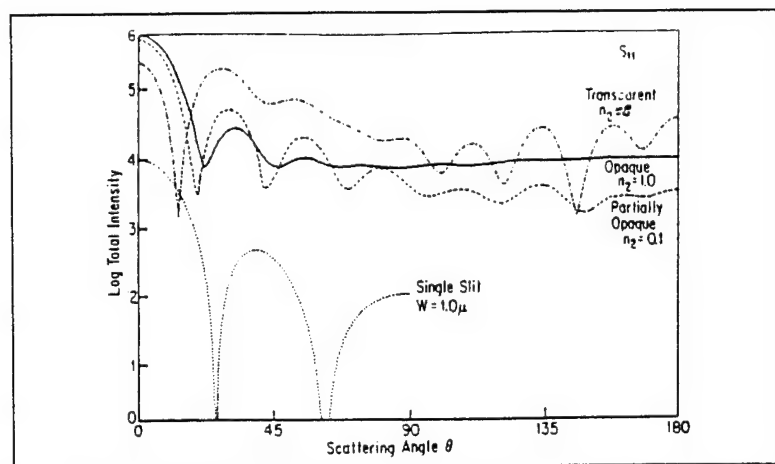


Figure 2.2. Diffraction versus Scattering Intensity Patterns. The three curves at the top of the plot are theoretical intensity scattering patterns for fibers of various degrees of absorption. Both the slit and the fibers are 1  $\mu\text{m}$  wide and are illuminated by  $\lambda = 4417 \text{ \AA}$  laser light. The quartz fibers have a real index of refraction  $n_1 = 1.466$ .

Scattering patterns, however, are less easily categorized. No simple formula relates the distance between the intensity minima of a perfectly cylindrical quartz fiber scattering pattern and its radius. To get the radius or any other information about the scatterer, measurements

must be made over all 180 degrees of scatter and the data compared to the solutions of Maxwell's equations for a cylindrical interface.

## 2.2 Polarization Relations

Information about the scattering target is contained in the polarized light. When considering scatterers and scattered light, the unpolarized light incident upon the scatterer is usually given horizontal or vertical polarization, or some combination of the two (circular/elliptical or 45 degree). The Mueller matrices characterize optical elements and scatterers. The Stokes vectors describe the incoming or outgoing radiation. These two mathematical constructs completely describe polarized light and the scattering properties of any scatterer.

Consider a laser beam propagating in the z-direction with an electric field described by

$$\mathbf{E} = \mathbf{E}_0 \exp i (\mathbf{k} \cdot \mathbf{r} - \omega t)$$

where  $\mathbf{k}$  is the wavenumber ( $2\pi / \lambda$ , in the direction of propagation) and  $\omega$  is the angular frequency of the laser. The electric field vector  $\mathbf{E}$  has two components:  $\mathbf{e}_1$  and  $\mathbf{e}_2$ , which correspond to the x and y axes of the laser's coordinate system. Unpolarized laser light will have no preferred direction for the  $\mathbf{E}$  vector.

Therefore,  $\mathbf{E}_0$  can be expressed as

$$\mathbf{E}_0 = E_1 \mathbf{e}_1 + E_2 \mathbf{e}_2$$

$$E_1 = A \exp (-i \delta_1)$$

$$E_2 = B \exp (-i \delta_2)$$

where  $A$  and  $B$  are the maximum amplitudes of the electric fields in the  $\mathbf{e}_1$  and  $\mathbf{e}_2$  directions, and  $\delta_1$  and  $\delta_2$  give the phase of each of the components. If the components are in phase, the direction of  $\mathbf{E}_0$  will not change, and the resultant electric field will oscillate along a single line in the x-y plane. This is referred to as linear polarization. If  $\delta_1$  and  $\delta_2$  are not in phase  $\mathbf{E}_0$  will rotate about the propagation axis, giving elliptical polarization. Circular polarization occurs for the special case when  $A$  and  $B$  are equal and the components are exactly 90 degrees out of phase.

### 2.3 Stokes Vectors

In 1852 G.G. Stokes established a formalism for describing polarization which is still in use today. The Stokes vector uses four measurements from four filters to characterize completely the polarization of an electromagnetic wave. The first filter passes all incident light. The second and third filter both pass linearly polarized light, with the former passing only horizontally polarized light and the latter passing only light polarized at a  $45^\circ$  angle (in other words, the  $\mathbf{e}_1$  and  $\mathbf{e}_2$  vectors are in phase, and  $A$  and  $B$  are equal in amplitude). The fourth filter transmits only right-hand circular polarization. Each filter is opaque to the opposite polarizations. Stokes used the filtered intensities to give these quantities (from Hecht, 1979)

$$I = I_0$$

$$Q = 2 I_1 - I_0$$

$$U = 2 I_2 - I_0$$

$$V = 2 I_3 - I_0$$

$I_0$ ,  $I_1$ ,  $I_2$ , and  $I_3$  are the intensities measured when filters 1, 2, 3, and 4 respectively are placed between the electric field source and the detector.

Each of these quantities can be related to the amplitudes and phase difference of the two axes  $\mathbf{e}_1$  and  $\mathbf{e}_2$ . Starting with total intensity,

$$\begin{aligned}
 I &= \langle \mathbf{E} \mathbf{E}^* \rangle = \mathbf{E}_0 \mathbf{E}_0^* \\
 &= (\mathbf{E}_1 \mathbf{e}_1 + \mathbf{E}_2 \mathbf{e}_2) \cdot (\mathbf{E}_1 \mathbf{e}_1 + \mathbf{E}_2 \mathbf{e}_2)^* \\
 &= E_1 E_1^* + E_2 E_2^* \\
 &= A^2 + B^2
 \end{aligned}$$

The next quantity is the horizontal polarization.

$$\begin{aligned}
 Q &= 2 I_1 - I_0 = 2 (\mathbf{E}_1 \mathbf{E}_1^*) - E_1 E_1^* - E_2 E_2^* \\
 &= E_1 E_1^* - E_2 E_2^* \\
 &= A^2 - B^2
 \end{aligned}$$

The third quantity,  $+45^\circ$  polarization, requires a trick to make the mathematics of the problem tractable. The electric field can be represented not only by the  $\mathbf{e}_1 - \mathbf{e}_2$  axis system, but by any linear combination of the two which are still orthogonal. Hsu (1992) noted that the two vectors which will solve the problem for  $+45^\circ$  polarization are:

$$\begin{aligned}
 U &= 2 I_2 - I_0 = 2 \left( \frac{1}{\sqrt{2}} (E_1 + E_2) \right) \frac{1}{\sqrt{2}} (E_1 + E_2)^* - I_0 \\
 &= E_1 E_1^* + E_2 E_2^* + E_1 E_2^* + E_2 E_1^* - E_1 E_1^* - E_2 E_2^* \\
 &= E_1 E_2^* + E_2 E_1^* \\
 &= A \exp(-i \delta_1) B \exp(i \delta_2) + B \exp(-i \delta_2) A \exp(i \delta_1)
 \end{aligned}$$

$$= A B \{ \exp -i (\delta_1 - \delta_2) + \exp i (\delta_1 - \delta_2) \}$$

$$= 2 A B \cos \delta$$

$$\text{where } \delta = \delta_1 - \delta_2$$

The same procedure is followed for the V element, except that the two orthogonal elements are now right and left circular polarization. The rotation of the resultant field vector will be right-handed if the vector turns counterclockwise when the  $\mathbf{k}$  vector is pointed directly at the observer. Therefore, the  $\mathbf{e}_1$  component leads the  $\mathbf{e}_2$ . This phase difference can be represented by the imaginary  $i$ . Hsu used the following orthogonal basis vectors:

$$\begin{aligned} V &= 2 I_3 - I_0 = 2 \left( \frac{1}{\sqrt{2}} (E_1 - iE_2) \right) \frac{1}{\sqrt{2}} (E_1 - iE_2)^* - I_0 \\ &= E_1 E_1^* + E_2 E_2^* - i E_2 E_1^* + i E_1 E_2^* - E_1 E_1^* - E_2 E_2^* \\ &= i (E_1 E_2^* - E_2 E_1^*) \\ &= i \{ A \exp (-i \delta_1) B \exp (i \delta_2) - B \exp (-i \delta_2) A \exp (i \delta_1) \} \\ &= i A B \{ \exp (-i \delta) - \exp (i \delta) \} \\ &= 2 A B \sin \delta \end{aligned}$$

$$\text{Again, } \delta = \delta_1 - \delta_2.$$

The total intensity may be represented as a vector in a fictional "polarization space." In this three-dimensional space, the axes are the Q, U, and V elements of the Stokes vector. The intensity of a general polarized beam is described by these three orthogonal vectors.

$$I^2 \geq Q^2 + U^2 + V^2$$

For a completely polarized beam, the equality holds.

$$I^2 = Q^2 + U^2 + V^2$$

$$(A^2 + B^2)^2 = (A^2 - B^2)^2 + (2AB \cos \delta)^2 + (2AB \sin \delta)^2$$

$$A^4 + B^4 + 2A^2B^2 = A^4 + B^4 - 2A^2B^2 + 4A^2B^2(\cos^2 \delta + \sin^2 \delta)$$

$$4A^2B^2 = 4A^2B^2$$

A partially unpolarized beam (i.e. a mixture of pure states and an unpolarized component) will not be completely described by the polarization terms, so in this case,  $I$  can be greater than the sum of the other three Stokes vector components.

The complete form of the Stokes vector is the following:

$$|V| = \begin{vmatrix} I \\ Q \\ U \\ V \end{vmatrix} = \begin{vmatrix} \langle E_1 E_1^* + E_2 E_2^* \rangle \\ \langle E_1 E_1^* - E_2 E_2^* \rangle \\ \langle E_1 E_2^* + E_2 E_1^* \rangle \\ \langle i(E_1 E_2^* - E_2 E_1^*) \rangle \end{vmatrix}$$

where  $E_1$  and  $E_2$  are the electric field components perpendicular to the direction of propagation in the horizontal and vertical directions ( $\mathbf{e}_1$  and  $\mathbf{e}_2$ ), respectively.

The following relationships exist for the Stokes vector:

$$|V_h| = \begin{vmatrix} 1 \\ 1 \\ 0 \\ 0 \end{vmatrix} = \text{Horizontally polarized light}$$

$$\begin{aligned}
 |V_+\rangle &= \begin{pmatrix} 1 \\ 0 \\ 1 \\ 0 \end{pmatrix} = +45^\circ \text{ linear polarized light} \\
 |V_r\rangle &= \begin{pmatrix} 1 \\ 0 \\ 0 \\ 1 \end{pmatrix} = \text{Right-hand circularly polarized light}
 \end{aligned}$$

## 2.4 Mueller Matrices

For almost a century, the Stokes vector alone was used to describe the polarization of light. However, in 1943 an MIT professor named Hans Mueller developed a mathematical device to complement the Stokes vector. The Mueller scattering matrix predicts how any optical system affects the polarization of light incident upon it. The scatterer is represented by a 4 x 4 Mueller matrix. Its elements ( $S_{ij}$ ) relate the way that the target will change the polarization of the light incident on it. The  $S_{ij}$  are  $\theta$  and  $\phi$  dependent. An object such as a horizontal polarizer has only one value per matrix element for a given orientation. A "scatterer" sends light in all directions, but the cylindrical target will scatter light only in the  $\theta$  direction (i.e. - confined to the plane perpendicular to the cylinder).

We can derive the Mueller scattering matrix of any optical device. As an example, consider an arbitrary linear polarizer which can be rotated to any angle  $\Phi$  in the electric vector ( $\mathbf{e}_1$ - $\mathbf{e}_2$ )

plane. When illuminated with completely unpolarized light, the output beam has 1/2 the incident intensity. The output polarization has a horizontal component which varies as  $\cos 2\Phi$  and a  $+45^\circ$  component which varies as  $\sin 2\Phi$ . Mathematically, this appears as:

$$[S_{ij}] |V_i| = |V_f|$$

$$\begin{bmatrix} S_{11} & S_{12} & S_{13} & S_{14} \\ S_{21} & S_{22} & S_{23} & S_{24} \\ S_{31} & S_{32} & S_{33} & S_{34} \\ S_{41} & S_{42} & S_{43} & S_{44} \end{bmatrix} \begin{bmatrix} 1 \\ 0 \\ 0 \\ 0 \end{bmatrix} = \frac{1}{2} \begin{bmatrix} 1 \\ \cos 2\Phi \\ \sin 2\Phi \\ 0 \end{bmatrix}$$

$$S_{11} = 1/2$$

$$S_{21} = 1/2 \cos 2\Phi$$

$$S_{31} = 1/2 \sin 2\Phi$$

$$S_{41} = 0$$

These results are substituted into the first column of the matrix. Next we illuminate the target with completely horizontally polarized light. In this case, two variables will change in the output beam: the polarization and the intensity. The polarization will vary exactly as it did in the unpolarized case. The intensity varies from full value to zero as shown below.

$$\begin{bmatrix} 1/2 & S_{12} & S_{13} & S_{14} \\ 1/2 \cos 2\Phi & S_{22} & S_{23} & S_{24} \\ 1/2 \sin 2\Phi & S_{32} & S_{33} & S_{34} \\ 0 & S_{42} & S_{43} & S_{44} \end{bmatrix} \begin{bmatrix} 1 \\ 1 \\ 0 \\ 0 \end{bmatrix} = \frac{1}{2} + \frac{1}{2} \cos 2\Phi \begin{bmatrix} 1 \\ \cos 2\Phi \\ \sin 2\Phi \\ 0 \end{bmatrix}$$

$$1/2 + S_{12} = 1/2 + 1/2 \cos 2\Phi$$

$$1/2 \cos 2\Phi + S_{22} = 1/2 \cos 2\Phi + 1/2 \cos^2 2\Phi$$

$$1/2 \sin 2\Phi + S_{32} = 1/2 \sin 2\Phi + 1/2 \sin 2\Phi \cos 2\Phi$$

$$S_{42} = 0$$

Illuminating the target with  $+45^\circ$  polarized light gives an output polarization which varies as before and output intensity which varies as before, but is shifted by  $45^\circ$  (because the polarizer is shifted  $+45^\circ$ ).

$$\begin{bmatrix} 1/2 & 1/2 \cos 2\Phi & S_{13} & S_{14} \\ 1/2 \cos 2\Phi & 1/2 \cos^2 2\Phi & S_{23} & S_{24} \\ 1/2 \sin 2\Phi & 1/2 \cos 2\Phi \sin 2\Phi & S_{33} & S_{34} \\ 0 & 0 & S_{43} & S_{44} \end{bmatrix} \begin{vmatrix} 1 \\ 0 \\ 0 \\ 0 \end{vmatrix} = \begin{vmatrix} 1 & 1 \\ 2 & 2 \end{vmatrix} \begin{vmatrix} 1 \\ \cos 2\Phi \\ \sin 2\Phi \\ 0 \end{vmatrix}$$

$$1/2 + S_{13} = 1/2 + 1/2 \sin 2\Phi$$

$$1/2 \cos 2\Phi + S_{23} = 1/2 \cos 2\Phi + 1/2 \sin 2\Phi \cos 2\Phi$$

$$1/2 \sin 2\Phi + S_{33} = 1/2 \sin 2\Phi + 1/2 \sin^2 2\Phi$$

$$S_{43} = 0$$

Finally, a completely right handed circularly polarized input beam will change to a beam with half the incident intensity and an output polarization which varies as before.

$$\begin{bmatrix} 1/2 & 1/2 \cos 2\Phi & 1/2 \sin 2\Phi & S_{14} \\ 1/2 \cos 2\Phi & 1/2 \cos^2 2\Phi & 1/2 \cos 2\Phi \sin 2\Phi & S_{24} \\ 1/2 \sin 2\Phi & 1/2 \cos 2\Phi \sin 2\Phi & 1/2 \sin^2 2\Phi & S_{34} \\ 0 & 0 & 0 & S_{44} \end{bmatrix} \begin{vmatrix} 1 \\ 0 \\ 0 \\ 1 \end{vmatrix} = \begin{vmatrix} 1 \\ 2 \end{vmatrix} \begin{vmatrix} 1 \\ \cos 2\Phi \\ \sin 2\Phi \\ 0 \end{vmatrix}$$

$$1/2 + S_{14} = 1/2$$

$$1/2 \cos 2\Phi + S_{24} = 1/2 \cos 2\Phi$$

$$1/2 \sin 2\Phi + S_{34} = 1/2 \sin 2\Phi$$

$$S_{44} = 0$$

This leads to the full matrix for the linear polarizer with an arbitrary orientation in the plane of the electric field (solved first by Bickel and Bailey, 1984):

$$[lp] = \frac{1}{2} \begin{bmatrix} 1 & \cos 2\Phi & \sin 2\Phi & 0 \\ \cos 2\Phi & \cos^2 2\Phi & \cos 2\Phi \sin 2\Phi & 0 \\ \sin 2\Phi & \cos 2\Phi \sin 2\Phi & \sin^2 2\Phi & 0 \\ 0 & 0 & 0 & 0 \end{bmatrix}$$

where  $\Phi$  is the angle that the polarizer's orientation makes with respect to the horizontal plane of the beam.

The primary goal in light scattering experiments is to determine the 16 scattering matrix elements  $S_{ij}(\theta)$  for any scatterer. However, a photomultiplier tube (PMT) can only detect and count photons and not analyze polarizations. We use all variations of input and output polarizers in various orientations to place information from all sixteen elements into the total intensity component. The final result of all combinations is put into another "matrix" (shown in Figure 2.3).

Consider a scatterer with an arbitrary, unknown Mueller matrix

$$[S] = \begin{bmatrix} S_{11} & S_{12} & S_{13} & S_{14} \\ S_{21} & S_{22} & S_{23} & S_{24} \\ S_{31} & S_{32} & S_{33} & S_{34} \\ S_{41} & S_{42} & S_{43} & S_{44} \end{bmatrix}$$

Illuminating the scatterer with right hand circularly polarized light gives

$$\begin{bmatrix} S_{11} & S_{12} & S_{13} & S_{14} \\ S_{21} & S_{22} & S_{23} & S_{24} \\ S_{31} & S_{32} & S_{33} & S_{34} \\ S_{41} & S_{42} & S_{43} & S_{44} \end{bmatrix} \begin{bmatrix} 1 \\ 0 \\ 0 \\ 1 \end{bmatrix} = \begin{bmatrix} S_{11} + S_{14} \\ S_{21} + S_{24} \\ S_{31} + S_{34} \\ S_{41} + S_{44} \end{bmatrix}$$

Now, analyze the scattered light with a horizontal polarizer [ h ].

$$\begin{bmatrix} 1 & 1 & 0 & 0 \\ 1 & 1 & 0 & 0 \\ 0 & 0 & 0 & 0 \\ 0 & 0 & 0 & 0 \end{bmatrix} \begin{bmatrix} S_{11} + S_{14} \\ S_{21} + S_{24} \\ S_{31} + S_{34} \\ S_{41} + S_{44} \end{bmatrix} = \begin{bmatrix} S_{11} + S_{14} + S_{21} + S_{24} \\ S_{11} + S_{14} + S_{21} + S_{24} \\ 0 \\ 0 \end{bmatrix}$$

The output beam is completely horizontally polarized and the total intensity contains information from four of the Mueller matrix elements  $S_{ij}$ . This procedure gives all sixteen optics combinations given in Figure 2.3. These matrix elements are distinguished from the original single  $S_{ij}$  elements by an asterisk. These sixteen experimental matrix components characterize our fibers with regard to radius, refractive index, and absorption.

$S_{11}^*$ * * * * $S_{11}$	$S_{12}^*$ * → * → * $S_{11} + S_{12}$ ↑ * $S_{11} - S_{12}$	$S_{13}^*$ * / * / * $S_{11} + S_{13}$ \ * $S_{11} - S_{13}$	$S_{14}^*$ * ○ * ○ * $S_{11} + S_{14}$ ○ * $S_{11} - S_{14}$
$S_{21}^*$ * * → * → $S_{11} + S_{21}$ * ↓ $S_{11} - S_{21}$	$S_{22}^*$ * ↔ * ↔ * $S_{11} + S_{12} + S_{21} + S_{22}$ → * $S_{11} + S_{12} - S_{21} - S_{22}$ ↓ * $S_{11} - S_{12} + S_{21} - S_{22}$ ↑ * $S_{11} - S_{12} - S_{21} + S_{22}$	$S_{23}^*$ * / → / → $S_{11} + S_{13} + S_{21} + S_{23}$ / ↓ $S_{11} + S_{13} - S_{21} - S_{23}$ \ → $S_{11} - S_{13} + S_{21} - S_{23}$ \ ↓ $S_{11} - S_{13} - S_{21} + S_{23}$	$S_{24}^*$ * ○ → ○ → $S_{11} + S_{14} + S_{21} + S_{24}$ ○ ↓ $S_{11} + S_{14} - S_{21} - S_{24}$ ○ → $S_{11} - S_{14} + S_{21} - S_{24}$ ○ ↓ $S_{11} - S_{14} - S_{21} + S_{24}$
$S_{31}^*$ * * / * / $S_{11} + S_{31}$ * \ $S_{11} - S_{31}$	$S_{32}^*$ * → / → / $S_{11} + S_{12} + S_{31} + S_{32}$ → \ $S_{11} + S_{12} - S_{31} - S_{32}$ ↓ / $S_{11} - S_{12} + S_{31} - S_{32}$ ↓ \ $S_{11} - S_{12} - S_{31} + S_{32}$	$S_{33}^*$ * / / / / $S_{11} + S_{13} + S_{31} + S_{33}$ / \ $S_{11} + S_{13} - S_{31} - S_{33}$ \ / $S_{11} - S_{13} + S_{31} - S_{33}$ \ \ $S_{11} - S_{13} - S_{31} + S_{33}$	$S_{34}^*$ * ○ / ○ / $S_{11} + S_{14} + S_{31} + S_{34}$ ○ \ $S_{11} + S_{14} - S_{31} - S_{34}$ ○ / $S_{11} - S_{14} + S_{31} - S_{34}$ ○ \ $S_{11} - S_{14} - S_{31} + S_{34}$
$S_{41}^*$ * * ○ * ○ $S_{11} + S_{41}$ * ○ $S_{11} - S_{41}$	$S_{42}^*$ * → ○ → ○ $S_{11} + S_{12} + S_{41} + S_{42}$ → \ ○ $S_{11} + S_{12} - S_{41} - S_{42}$ ↓ ○ $S_{11} - S_{12} + S_{41} - S_{42}$ ↑ ○ $S_{11} - S_{12} - S_{41} + S_{42}$	$S_{43}^*$ * / ○ / ○ $S_{11} + S_{13} + S_{41} + S_{43}$ / \ ○ $S_{11} + S_{13} - S_{41} - S_{43}$ \ / ○ $S_{11} - S_{13} + S_{41} - S_{43}$ \ \ ○ $S_{11} - S_{13} - S_{41} + S_{43}$	$S_{44}^*$ * ○ ○ ○ ○ $S_{11} + S_{14} + S_{41} + S_{44}$ ○ \ ○ $S_{11} + S_{14} - S_{41} - S_{44}$ ○ ○ $S_{11} - S_{14} + S_{41} - S_{44}$ ○ \ ○ $S_{11} - S_{14} - S_{41} + S_{44}$

Figure 2.3. Optics Combinations for the Experimental Mueller Scattering Matrix. Each part of the above matrix contains the scattering elements  $S_{ij}$  which comprise the experimental elements  $S_{ij}^*$ .

Our scatterers are perfect cylinders and, because of symmetry, the cylindrical fibers will have a simple matrix. Symmetric scatter does not mix the electric field vectors in the  $\mathbf{e}_1$  and  $\mathbf{e}_2$  direction. Iafelice (1987) noted that this geometry forces

$$S_{31} = S_{32} = S_{41} = S_{42} = 0 \quad \text{and} \quad S_{22} = 1$$

The only elements which are unique in the entire matrix are

$$\begin{aligned}
 S_{11}^* &= S_{11} & S_{12}^* &= \frac{S_{12} + S_{11}}{S_{11}} \\
 S_{33}^* &= \frac{S_{13} + S_{33}}{S_{31} + S_{11}} & S_{34}^* &= \frac{S_{14} + S_{34}}{S_{31} + S_{11}}
 \end{aligned}$$

Exact solutions for each of these matrix elements for certain geometries can be obtained by solving Maxwell's equations. The cylinder we use to solve Maxwell's equations has a precise

and uniform radius, index of refraction and absorption. It is illuminated with  $\lambda 4417\text{\AA}$  wavelength radiation propagating through a vacuum. Although these perfect fibers and perfect conditions do not exist in reality, we can manufacture high quality quartz fibers whose experimental scattering curves match theory very closely.

## CHAPTER 3

### THE POLAR NEPHELOMETER

#### 3.1 System Overview

A polar nephelometer measures the entire scattering matrix of any scatterer. A diagram of this device is shown in Figure 3.1. A helium-cadmium laser (HeCd,  $\lambda 4417\text{\AA}$ ) illuminates the sample. The laser beam initially passes through a variable neutral density filter (to reduce the light intensity) and a spatial filter. The beam then passes through a Morvue Electronic Systems PEM-3 photoelastic modulator, which can be adjusted to give the beam horizontal, vertical, 45 degree, or circular polarization. Finally the beam passes through a small aperture before illuminating the sample.

The sample holder can move in three dimensions (x, y, and z) and rotate about the fiber's axis. In addition, it can control the tilt angle of the stage to direct scattering into the x-y plane. A motor swings an eighteen inch long metal arm around the fiber at a speed of three degrees per second. This arm contains the PMT, linear polarizer, quarter wave plate and a bandpass filter peaking at the laser wavelength to reduce ambient light.

To measure the total intensity ( $S_{11}$  of the Mueller matrix elements), the PMT signal goes directly to a logarithmic picoammeter. The high voltage to the tube (from 0 to 1200 volts) is selected to adjust the PMT signal at maximum laser scattering intensity to  $10^{-6}$  amperes.

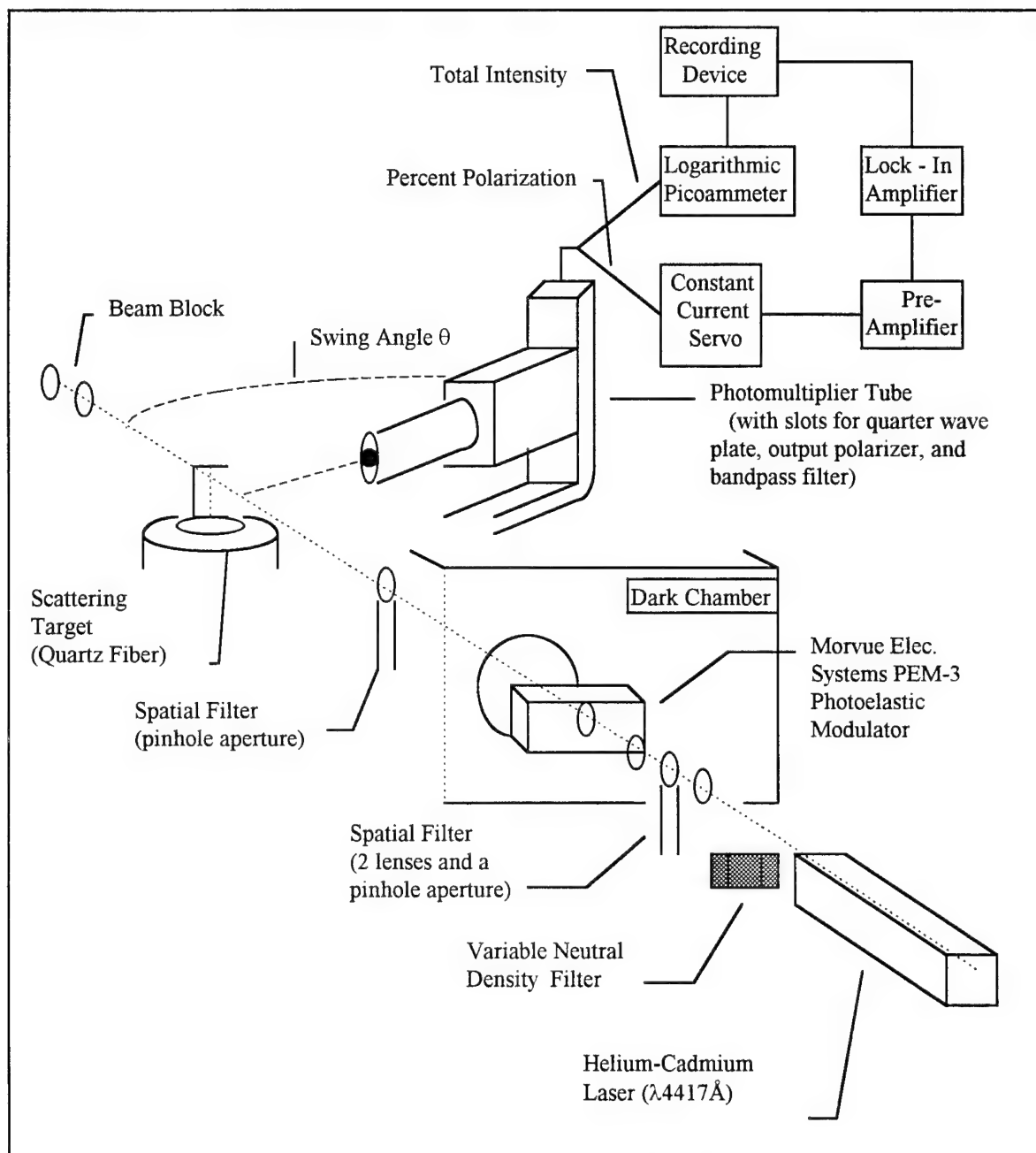


Figure 3.1. Experimental Setup of the Polar Nephelometer. The direction of the PMT signal (to the picoammeter or the constant current servo) is controlled with a toggle switch.

At 1200 volts, the dark current is  $10^{-9}$  amperes. All scattering signals have to be between these two extremes. The DC output from the ammeter is sent to a strip chart. The DC signals can also be sent to VIS 550 terminal and Motorola VME-10 computer. The data, stored in the computer, can be compared with theory, saved on hard drive, and printed to paper.

To measure the polarization matrix elements  $S_{12}^*$ ,  $S_{33}^*$ , or  $S_{34}^*$ , the PMT signal is sent first to a constant current servo (CCS) to control the amount of voltage on the PMT. With the high voltage set to about 700 V, the CCS adjusts the PMT voltage to keep the DC current constant as the intensity of the scattered laser light changes at certain angles. The DC portion of the polarization signal is separated from the AC (which contains the information about  $S_{ij}^*$ ). The AC signal goes to a lock-in amplifier, which measures the percent polarization of the output signal.

### 3.2 The Photoelastic Modulator

The Morvue Electronic Systems PEM-3 photoelastic modulator is used to induce periodic phase differences in the  $e_1$  and  $e_2$  components of the laser's electric field. This periodic phase difference (50 kHz) produces the resultant AC signal along with higher frequency harmonics which can be measured with the lock-in amplifier.

The PEM-3 is essentially a very fast quarter wave plate with a linear polarizer mounted on the optical axis between it and the laser. In the PEM-3, an amorphous block of quartz is vibrated via another piece of crystalline quartz at its resonant frequency of 50 kHz. The quartz is electronically stressed and relaxed along one axis, periodically changing the index of

refraction along that axis by small amounts. This gives a time-dependence in the phase difference between the two electric field vectors. The amplitude of the crystal modulation can be adjusted to give phase differences which vary by a quarter wave as a function of time. Therefore, the output wave will oscillate between right-hand and left-hand circular polarization.

The equation for the phase difference  $\delta$  is

$$\delta(t) = \frac{2\pi d}{\lambda} s \sin \omega t$$

In this equation,  $d$  is the thickness of the modulator crystal,  $\lambda$  is the laser beam wavelength ( $\lambda 4417\text{\AA}$ ),  $s$  is the stress coefficient for the crystal, and  $\omega$  is the mechanical resonant frequency of the crystal (50 kHz).

Now we will follow the laser beam along its entire path to the PMT. The following procedure can be used to find which  $S_{ij}$  elements comprise any of the 16 experimental  $S_{ij}^*$  elements. Consider the measurement of the  $S_{33}(\theta)^*$  matrix element. Figure 2.3 shows that measuring this element requires a  $+45^\circ$  polarizer in the input and output beams. The unpolarized beam, upon entering the PEM-3, passes through the  $+45^\circ$  linear polarizer. The PEM-3 crystal's fast axis is  $45^\circ$  to the linear polarizer's direction, so the crystal will be oriented at  $90^\circ$ . The mathematical setup is as follows.

$$[M_{90^\circ}] [lp_{45^\circ}] |V_{in}| = |V_{tgt}|$$

$$\begin{bmatrix} 1 & 0 & 0 & 0 \\ 0 & 1 & 0 & 0 \\ 0 & 0 & \cos \delta & -\sin \delta \\ 0 & 0 & \sin \delta & \cos \delta \end{bmatrix} \frac{1}{2} \begin{bmatrix} 1 & 0 & 1 & 0 \\ 0 & 0 & 0 & 0 \\ 1 & 0 & 1 & 0 \\ 0 & 0 & 0 & 0 \end{bmatrix} \begin{vmatrix} 1 \\ 0 \\ 0 \\ 0 \end{vmatrix} = \frac{1}{2} \begin{vmatrix} 1 \\ 0 \\ \cos \delta \\ \sin \delta \end{vmatrix}$$

The resultant vector  $|V_{tgt}|$  strikes the target, which is represented by an arbitrary Mueller matrix  $S_{ij}(\theta)$ .

$$\frac{1}{2} \begin{bmatrix} S_{11} & S_{12} & S_{13} & S_{14} \\ S_{21} & S_{22} & S_{23} & S_{24} \\ S_{31} & S_{32} & S_{33} & S_{34} \\ S_{41} & S_{42} & S_{43} & S_{44} \end{bmatrix} \begin{vmatrix} 1 \\ 0 \\ \cos \delta \\ \sin \delta \end{vmatrix} = \frac{1}{2} \begin{vmatrix} S_{11} + S_{13} \cos \delta + S_{14} \sin \delta \\ S_{21} + S_{23} \cos \delta + S_{24} \sin \delta \\ S_{31} + S_{33} \cos \delta + S_{34} \sin \delta \\ S_{41} + S_{43} \cos \delta + S_{44} \sin \delta \end{vmatrix}$$

After scattering the beam passes through another  $+45^\circ$  polarizer.

$$\frac{1}{2} \begin{bmatrix} 1 & 0 & 1 & 0 \\ 0 & 0 & 0 & 0 \\ 1 & 0 & 1 & 0 \\ 0 & 0 & 0 & 0 \end{bmatrix} \begin{vmatrix} S_{11} + S_{13} \cos \delta + S_{14} \sin \delta \\ S_{21} + S_{23} \cos \delta + S_{24} \sin \delta \\ S_{31} + S_{33} \cos \delta + S_{34} \sin \delta \\ S_{41} + S_{43} \cos \delta + S_{44} \sin \delta \end{vmatrix}$$

$$= \frac{1}{4} \begin{vmatrix} (S_{11} + S_{31}) + (S_{13} + S_{33}) \cos \delta + (S_{14} + S_{34}) \sin \delta & 0 \\ (S_{11} + S_{31}) + (S_{13} + S_{33}) \cos \delta + (S_{14} + S_{34}) \sin \delta & 0 \end{vmatrix}$$

The total intensity now consists of two parts: the DC, given by  $(S_{11} + S_{31})$ , and the AC, which contains the phase terms.

### 3.3 The Lock-In Amplifier

Polarization measurements are made using a lock-in amplifier to detect the AC signal at certain frequencies. First the DC is separated from the AC signal. The CCS controls the PMT high voltage, increasing it when the scattered light intensity is low, and decreasing it when the light intensity is high. The DC signal, which before varied with angle, is now held constant while the AC portions are measured by the lock-in and effectively divided by the DC value. The resulting current from the PMT is

$$i = K \left( 1 + \frac{S_{13} + S_{33}}{S_{11} + S_{31}} \cos \delta + \frac{S_{14} + S_{34}}{S_{11} + S_{31}} \sin \delta \right)$$

where K is an arbitrary constant accounting for the PMT response parameters.

The AC current is sent to the lock-in amplifier where it must be detected by tuning the amplifier, much like an AM radio, to the proper frequency. The scattering information is contained in the amplitudes of the cosine and sine functions of the PMT output current. This can be seen by expanding the phase difference terms into Bessel functions.

$$\cos \delta = \cos (C \sin \omega t) = J_0(C) + 2 J_2(C) \cos 2 \omega t + \dots$$

$$\sin \delta = \sin (C \sin \omega t) = 2 J_1(C) \sin \omega t + 2 J_3(C) \sin 3 \omega t + \dots$$

Tuning the carrier frequency of the lock-in amplifier to the fundamental (50 kHz) picks up the signal attached to the sine portion of the detected current. This signal is the  $S_{34}^*$  matrix element. Tuning to the first harmonic (100 kHz) locks the amplifier to the signal:

$$S_{33}^* = \frac{S_{13} + S_{33}}{S_{11} + S_{31}} A$$

A is a constant term combining K and the value of the Bessel function. Because  $S_{13}$  and  $S_{31}$  are zero, we get:

$$S_{33}^* = \frac{S_{33}}{S_{11}} A$$

The other three matrix elements can be determined in the same manner using Figure 2.3.

### 3.4 Nephelometer Calibration

The matrix element signals were normalized so that +/- 100% polarizations correspond to +/- 100% deflections on the lock-in meter, strip chart recorder and computer. A beam block placed at  $\theta = 0^\circ$  absorbed the direct beam and unscattered laser signals. The PMT was set at  $\theta = 5^\circ$  (the maximum intensity point) and the PMT voltage was increased to get a PMT current of one microamp. The PMT was then placed behind the beam block, the computer set to receive a start signal and the motor turned on. As the arm passed  $\theta = 0^\circ$ , a trigger pulse started the data collection program.

Polarization calibrations were made in the same way. First, the beam was attenuated with a 10% transmitting optic and variable neutral density filter. With the fiber and the beam block removed, the input and exit polarization optics were adjusted to get the desired polarization states. To get  $S_{12}^*$  the input polarizer was set at horizontal and the lock-in amplifier set to detect 100 kHz. The exit polarizer was removed. The lock-in signal was then adjusted to give

a full scale meter deflection which corresponded to one hundred percent negative or positive polarization. This was done by inserting a linear polarizer into the exit beam to simulate 100% polarization by the fiber. Calibrations were fine tuned by adjusting the relative phase of the photoelastic modulator and the lock-in, the amplitude of the modulator oscillations, and the amount of current from the PMT. When calibrated, the needle gave a full scale signal for +/- 100% horizontal and vertical polarization, and a zero signal for 0% polarization.

To measure the  $S_{33}^*$  matrix element 45 degree polarizers were placed in the input and exit beam. Calibration was accomplished by switching the exit polarizer between +/- 45 degree orientations to get full scale needle deflections of +/- 100% for each 45 degree PMT alignment and a zero for the horizontal and vertical cases. To measure the  $S_{34}^*$  matrix element the input polarizer was horizontal and the lock-in set to detect a 50 kHz signal. The exit polarization was 45 degrees. Calibration was achieved by rotating the exit polarizer between +/- 45 degree orientations to get full scale deflections, but with a quarter wave plate in front of the polarizer. The quarter wave plate was removed before the fiber scattering measurements were made.

## CHAPTER 4

### THE SCATTERER

The scatterer we use is a thin "perfect" circularly cross-sectioned quartz fiber. Maxwell's equations are easily solved for a cylinder. Creating quartz fibers is straightforward and quartz, unlike glass, has an exact, well known index of refraction throughout its structure. These small fibers ( $\sim 1$ -5 cm long, 0.1-100  $\mu\text{m}$  diameter) are easily stored, mounted, and manipulated for scattering experiments.

#### 4.1 Fiber Manufacture

First we had to construct a number of suitable quartz fibers. The criteria for suitability included:

- a. Fibers which were so close to perfectly cylindrical that their scattering pattern matched the solutions to Maxwell's equations for cylindrical boundary conditions. This was measured by comparing experimental curves with theory.
- b. Fibers which had a relatively uniform radius along their length, at least uniform within the diameter of the laser beam. Fibers whose diameters varied along larger vertical distances were used at one recorded position.

We made our fibers using two quartz rods and a butane-oxygen torch. Black cloth covered the adjacent walls and a very bright lamp illuminated the area to make it easier to see produced fibers. We mounted one rod in a clamp near the torch such that the rod's tip protruded into the hottest part of the flame. When it was close to molten, the tip of the other rod was also heated and placed on the other tip. The tips were then separated vigorously, creating a thin fiber stretched between the two tips.

We found that the vigor of the separation was essential in making high quality fibers. If the ends were pulled apart too slowly, the molten quartz cooled too quickly, and the sample solidified, giving fibers far too thick for our experiment. On the other hand, if the ends were pulled apart too fast, they either separated completely while still molten, produce a fiber too thin, or break the cooled fiber from one or both rods. The most effective pulls created a fiber about two to three feet long between the rods. The loose fibers were then collected with a wide, wooden fork whose prongs were lightly coated with glue.

The fibers were then transferred to small C-mounts. These mounts were paper clips which had been thoroughly cleaned and bent into a C-shaped bracket one inch high with arms one-half inch long. These were fastened to the inside of the lid of a small glass jar. We designed this system to store the fibers, keep them clean when not in use, and to fit securely in the target holder of the polar nephelometer.

Figure 4.1 shows how the fiber, stretched taut between the prongs of the fork, was transferred to the C-mounts. The C-mount ends were coated with rubber cement and placed on a segment of a uniform fiber. After the fiber was stuck to the cement, it was cut just above

and below the edges of the C-mount. The assembly was screwed into the glass jar and left to dry. About twenty-five samples were created in this way.

To test the fibers, the jar lid with fiber sample was placed in the center of the nephelometer. The sample holder was moved to place the fiber in the laser beam and the tilt adjusted to send the pattern into the PMT aperture at all scattering angles  $\theta$ . The fiber itself (and not simply the pattern) was aligned with the PMT aperture, and we ensured that the laser beam struck the middle, clean sections of the fiber.

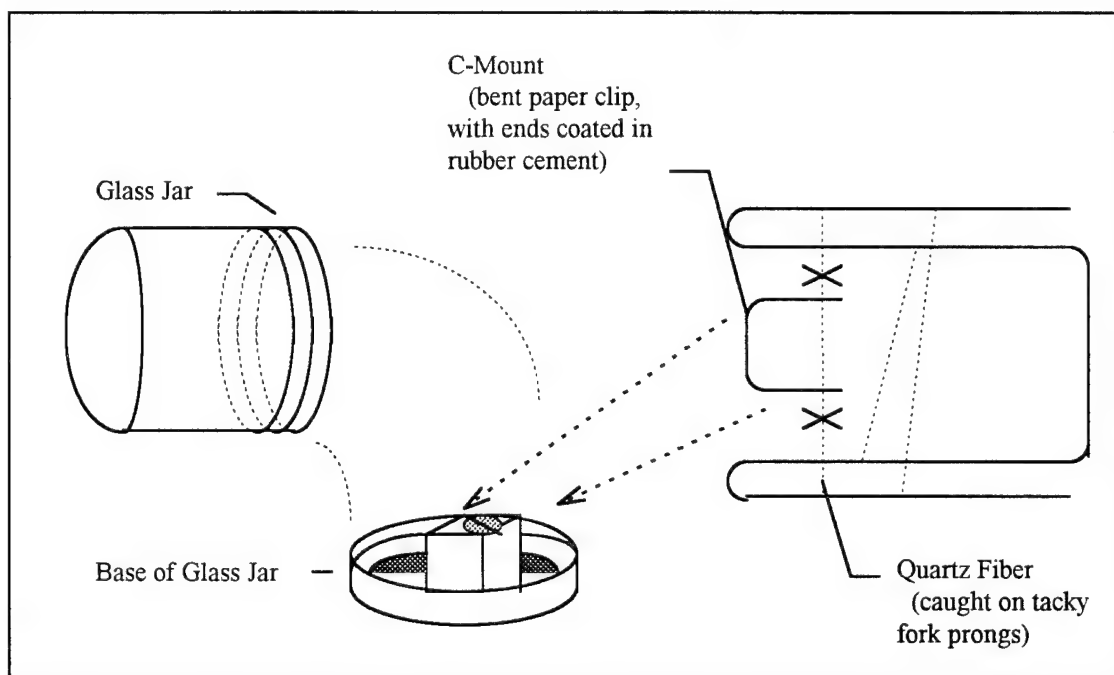


Figure 4.1. Diagram of the Fiber Mounting Procedure. The fiber is initially captured with the tacky prongs of a makeshift wooden fork. A C-mount with its ends coated with rubber cement is stuck to an exposed fiber and the ends of the fiber trimmed. The C-mount is reattached to the lid, and the jar screwed onto the lid to allow the assembly to dry.

## 4.2 Experiment versus Theory for Five Fibers

We measured the scattering pattern from five fibers (radii ranging from 200 to 1350 nm) and compared them with theory. All four Mueller matrix elements ( $S_{11}$ ,  $S_{12}^*$ ,  $S_{33}^*$ , and  $S_{34}^*$ ) were used. Both the theoretical and the experimental  $S_{ij}^*$  are shown in Figures 4.2 through 4.6. The fitting process is like trying on a shoe; we overlaid sets of theory curves until the fit did not improve. Theory requires three parameters - index of refraction, absorption, and radius of the fiber - to get a curve. The index of refraction ( $n$ ) and absorption ( $\mu$ ) are known for quartz, so the only parameter to vary was the radius. Increments in fiber diameters as low as a half of a nanometer were used to fit the curves. The previous best fit gave an accuracy of one nanometer in a micron. The most accurate guesses are made when all four matrix elements are fit to the theoretical changes in intensity and polarization phase and amplitude. Even though all scattering elements could detect radius changes, some were more sensitive than others.

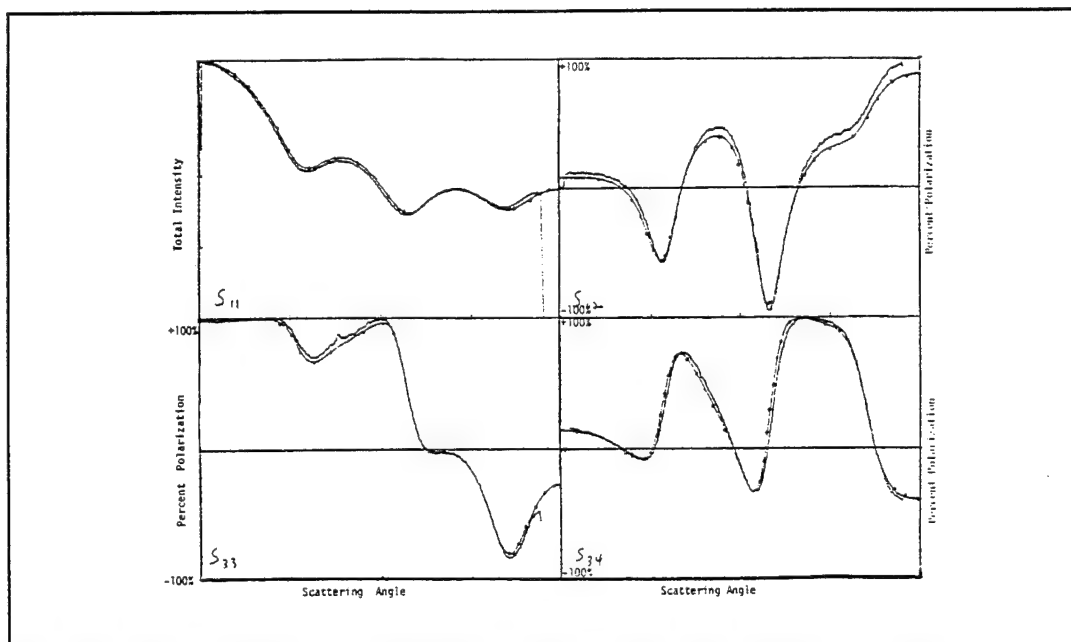


Figure 4.2. Fiber K, Experiment vs. Theoretical 0.2305  $\mu\text{m}$  Fiber. The solid line is the experimental curve, and the dotted line is the theory curve.

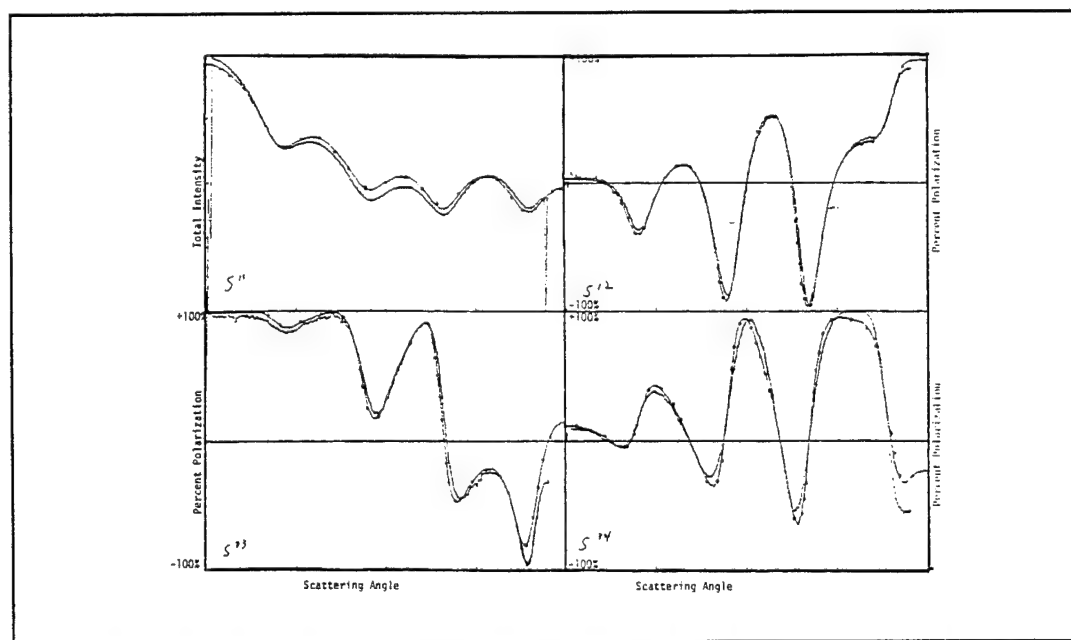


Figure 4.3. Fiber A, Experiment vs. Theoretical 0.2900  $\mu\text{m}$  Fiber. The solid line is the experimental curve, and the dotted line is the theory curve.

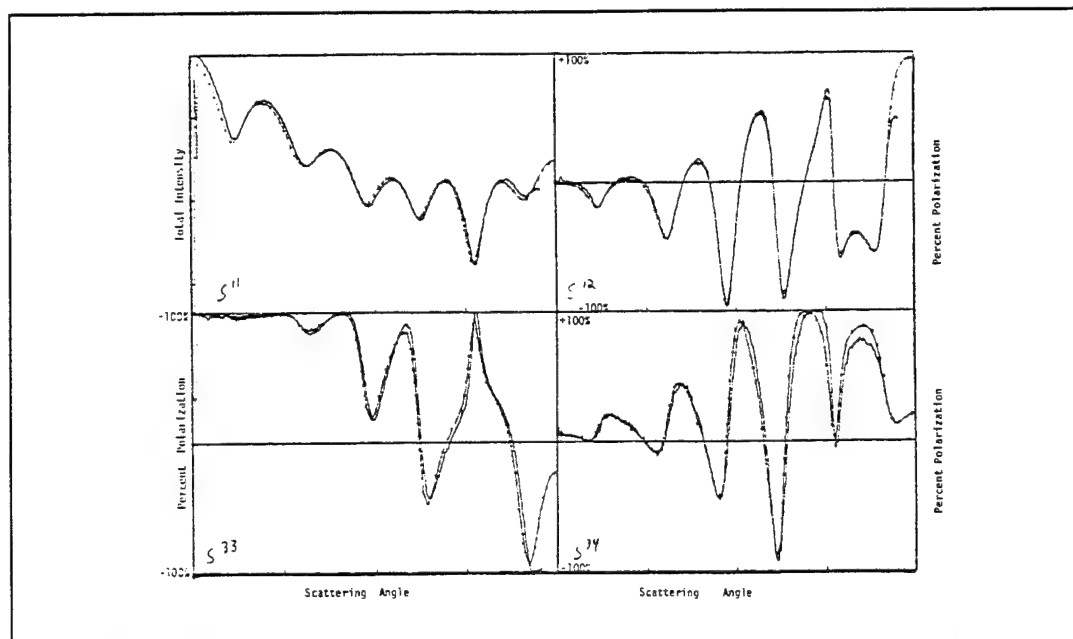


Figure 4.4. Fiber E, Experiment vs. Theoretical 0.4415  $\mu\text{m}$  Fiber. The solid line is the experimental curve, and the dotted line is the theory curve.

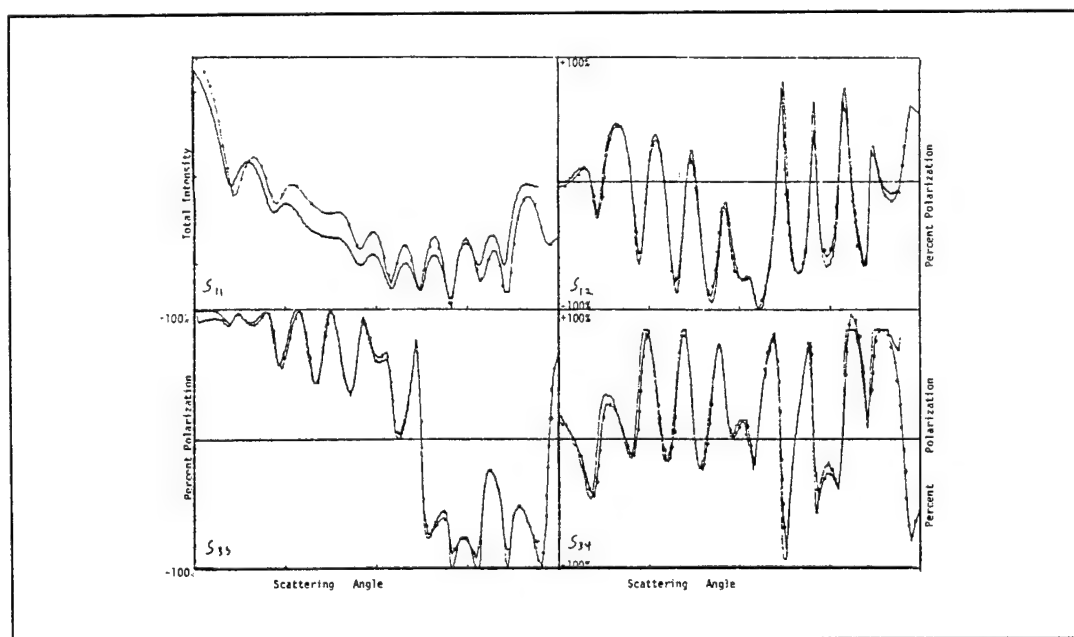


Figure 4.5. Fiber D, Experiment vs. Theoretical 0.7305  $\mu\text{m}$  Fiber. The solid line is the experimental curve, and the dotted line is the theory curve.

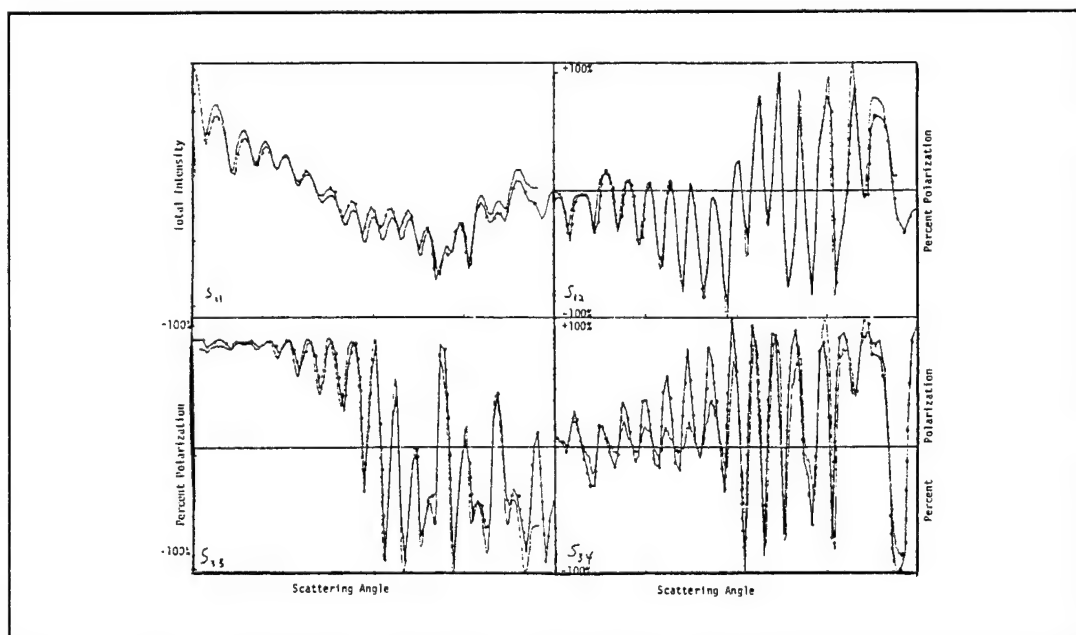


Figure 4.6. Fiber C, Experiment vs. Theoretical 1.3525  $\mu\text{m}$  Fiber. The solid line is the experimental curve, and the dotted line is the theory curve.

## CHAPTER 5

### ADSORPTION AND HUMIDITY

#### 5.1 Adsorption Theory

Even in Arizona, air contains a certain amount of water vapor. Its concentration is usually expressed in terms of the relative partial pressure of water in the atmosphere, called the relative humidity. When the relative humidity is less than 100%, and no particles are present in the atmosphere, any droplet which forms from water molecules will quickly evaporate. In supersaturated environments ( $RH > 100\%$ ), a water drop is in the unstable equilibrium shown graphically in Figure 5.1. A droplet with a radius smaller than a critical value will evaporate, while one with a radius greater than critical will grow. This "winner takes all" radius depends on the relative humidity. The greater the humidity, the smaller the drop needs to be to survive.

This behavior is based on thermodynamic theory and minimum energy. When water molecules collide they experience a change in the Gibbs free energy. Changing from a vapor to a liquid causes a decrease in the chemical potential of each molecule, which lowers the system's energy and causes nucleation. However, increasing the system's surface area requires energy to keep the unit together. This frustrates nucleation. Wallace and Hobbs (1977) describe the change of energy as

$$\Delta E = \sigma A - n V (u_v - u_l)$$

where  $\sigma$  is the work done per unit surface area of the water droplet,  $A$  is the surface area,  $n$  is the number of water molecules per unit volume,  $V$  is the droplet volume, and  $u_v$  and  $u_l$  are the chemical potentials of water in vapor

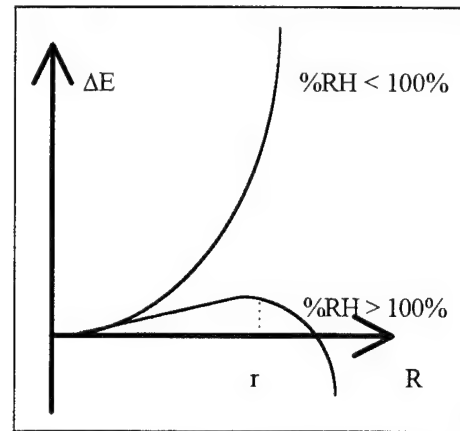


Figure 5.1. Change in Gibbs Free Energy versus Water Droplet Radius.

and liquid form. The difference in chemical potentials can be written in terms of relative humidity, and the surface area and volume in terms of the spherical droplet radius.

$$\Delta E = 4 \pi R^2 \sigma - 4/3 \pi R^3 n k T \ln (e / e_s)$$

Here  $R$  is the droplet radius,  $T$  is the temperature in degrees Kelvin,  $k$  is the Boltzmann constant, and  $e$  and  $e_s$  are the vapor pressure and saturation vapor pressure of water at temperature  $T$ , respectively. The term  $e / e_s$ , when multiplied by 100, is the percent relative humidity (%RH) of the system.

This equation has critical ramifications for cloud physics. If the %RH is under 100%, the second term in the energy equation will be negative, and  $\Delta E$  will always be positive. A system will not move toward a position of higher energy, so droplets break apart at these humidities. If the %RH is over 100% ("supersaturated"),  $\Delta E$  will start increasing, but then reach a point (shown in Figure 5.1) where it is maximized. Past this point, it becomes a favorable energy change for droplets accept more gaseous molecules, thus forming macroscopic drops. The radius  $r$  at which  $\Delta E$  is a maximum can be determined by differentiating the energy equation, resulting in Kelvin's formula:

$$r = \frac{2\sigma}{n k T \ln(\%RH / 100)}$$

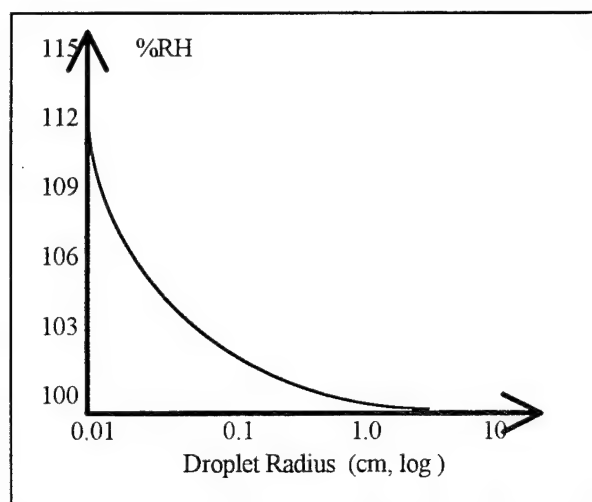


Figure 5.2. Curve for the Kelvin Equation. The relative humidity refers to pure water droplets at 5° C.

The curve for Kelvin's formula is shown in Figure 5.2.

The above process is referred to as homogeneous nucleation; that is, only water is involved in the drop formation. However, raindrops rarely form from this process because cloud humidities rarely exceed 101%. This would require a spontaneously formed droplet about 1

micron in radius, which is a very rare occurrence. Heterogeneous nucleation is the dominant process in drop formation and is the process used by the water as it is adsorbed onto the fiber surface.

The particles which water binds to in the atmosphere are called aerosols. Aerosols in nature mainly consist of sodium chloride, ash, silicon, or other dust-like materials. There are various subclassifications of aerosols. The first is wettability. If a particle is wettable, then the water molecules which bind to it will form a uniform layer over its entire surface, and not bunch into drops on it. The coated aerosol has a fixed surface area but in it are a much smaller number of water molecules than would be in a pure water droplet of the same size. Even so, the coated particle will still either grow or shrink based upon the combined radius of it and its water layer, and the amount of humidity in the air. Because there are fewer molecules making

the energetically favorable transition from vapor to liquid, the coated aerosol does not reach the Kelvin radius as quickly as a pure water droplet of the same radius. It is much easier for the water molecules to spontaneously form a critical radius droplet with wettable aerosols than without, but supersaturation is still a prerequisite for the formation of larger drops from droplets.

The second major subclassification is solubility. Many aerosols are bonded ion pairs, such as the salt NaCl. When water binds to a soluble aerosol, the aerosol partially dissolves, and the coating becomes a solution. This reduces the saturation vapor pressure  $e_s$  in the region immediately surrounding the aerosol, and the eventual result is that supersaturation with respect to pure water is no longer required for drop formation. The curves describing the

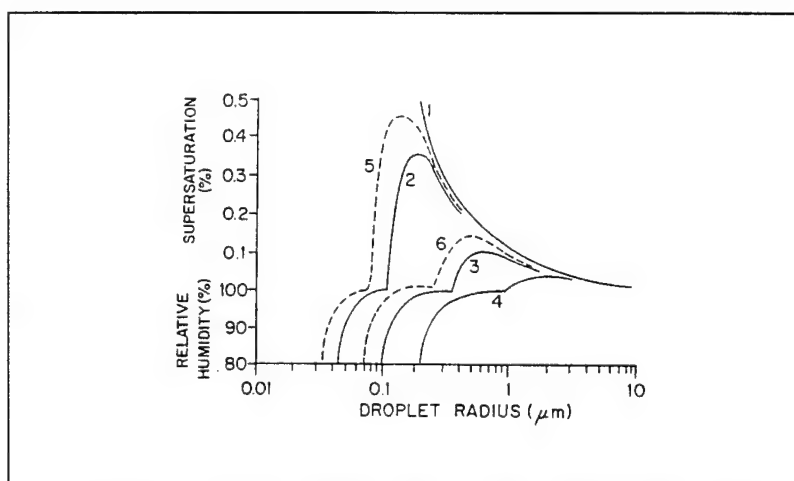


Figure 5.3. Curves Solving the Köhler Equation for NaCl and  $(\text{NH}_4)_2\text{SO}_4$ . Curve 1 shows pure water droplets (Kelvin curve). Curves 2, 3, and 4 solve for  $10^{-19}$ ,  $10^{-18}$ , and  $10^{-17}$  kg of NaCl per droplet respectively. Curves 5 and 6 solve for  $10^{-19}$  and  $10^{-18}$  kg of  $(\text{NH}_4)_2\text{SO}_4$  per droplet, in that order.

critical radii of soluble aerosol droplets are known as the Köhler curves (shown in Figure 5.3). As the drops become larger, the solutions on the surface become more dilute, and so behave more like pure water drops. Therefore, the Köhler curves converge to the Kelvin curves at larger droplet radii. The unfortunate fact about this behavior is that it makes acid rain much easier to form than any kind of pure rain. Clouds condense onto acidic nuclei and form rain because it is one of the most energetically favorable processes.

Our quartz fibers have dimensions similar to those of atmospheric aerosols. Fiber surfaces can be considered wettable but nonsoluble. Therefore, they should not begin accumulating water at a runaway pace, because the relative humidity will be less than 99%. We expect an equilibrium condition where the high humidities force water to bind to the layer at the same rate that the unfavorable energy conditions cause molecules to fly off.

Our experiment does not require drop formation, although the above energy equations offer insight to the basic layer formation process on surfaces. Water molecules can easily form on a surface exposed to high humidities. A supersaturated environment is not necessary. Fisher, Gamble and Middlehurst (1981) measured the growth of an absorbed water layer on a planar surface as a function of humidity. Their results are shown in Figure 5.4. Wentzel (1994) demonstrated that water vapor behaves similarly on a cylindrical quartz surface. His results, also shown in Figure 5.4, show that the growth rate of a water sheath on the cylinder is close to linear, while the adsorption on the planar surface increases by an order of magnitude between 97% and 99% RH. Intuitively, a water molecule on a flat surface has other molecules immediately to its side in all directions, whereas on small-radius cylinders the adherent water

molecules feel less of a containing force from two of its sides. Therefore we should expect a smaller film thickness on a fiber than for a flat plate at a given relative humidity. According to the argument, it should also follow that a sphere with radius equal that of the cylinder should have the smallest adsorbed water layer of all three cases.

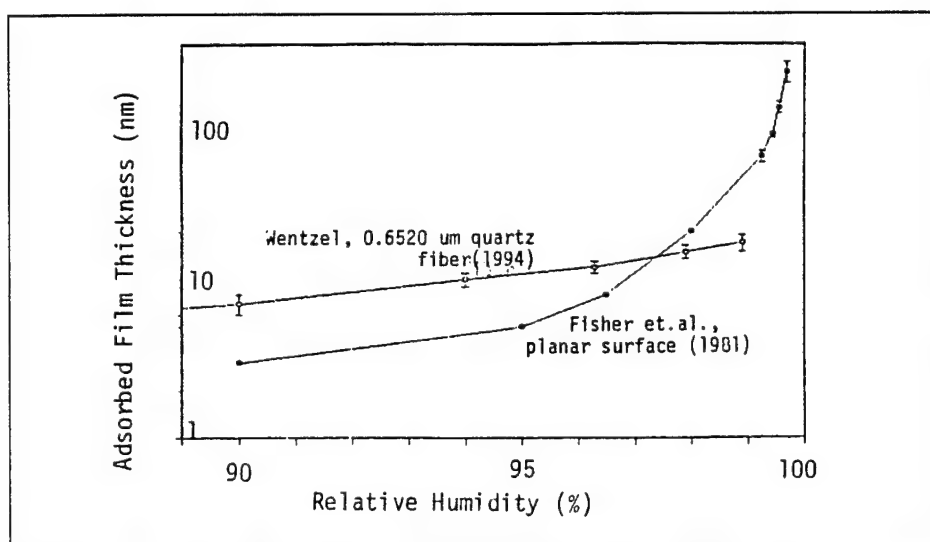


Figure 5.4. Water Layer Thickness vs. Relative Humidity for a Planar Surface and a Thin Quartz Fiber. The curve from Fisher, *et al.* shows rapid growth of the layer at high humidities, where Wentzel's curve shows a more modest growth at the same levels.

Figure 5.4 demonstrates that these adsorbed layers are extremely small. Wentzel's fiber gained a water layer thickness only about 1.5% the radius of the fiber. Most techniques used to measure the extremely small layers would involve altering, if destroying the sample. Laser scattering is non destructive. Figure 5.5 shows the theoretical  $S_{ij}^*$  curves for a 1.000  $\mu\text{m}$  quartz fiber coated by a thin water sheath. It demonstrates the response of the four scattering matrix elements -  $S_{11}$ ,  $S_{12}^*$ ,  $S_{33}^*$ , and  $S_{34}^*$  - to the addition of a 3 and 6 nm water layer to the fiber.

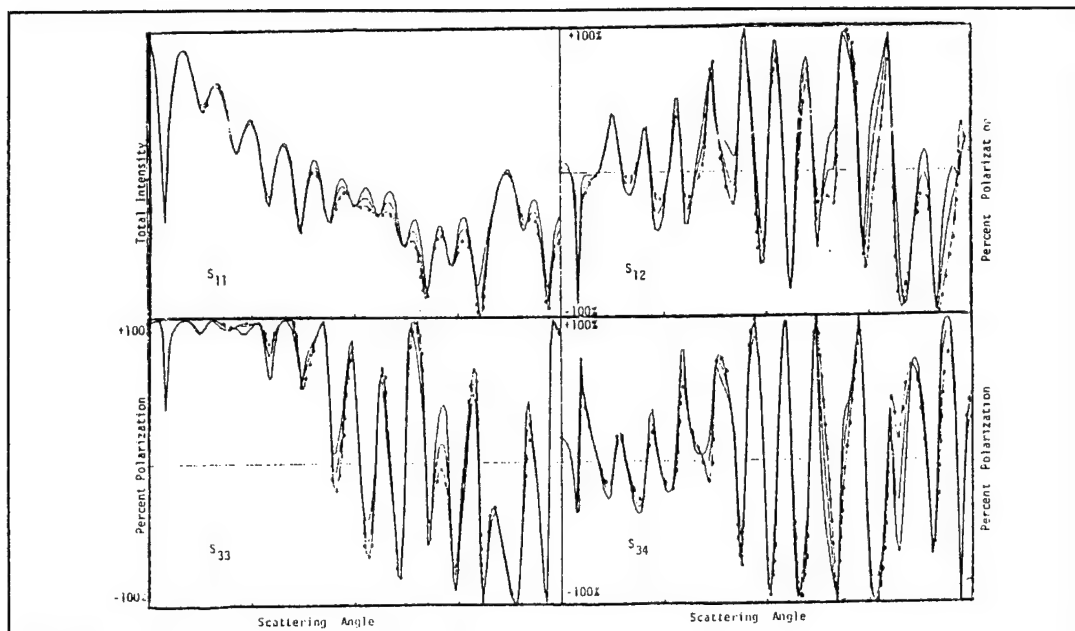


Figure 5.5. Scattering Curves of a Theoretical 1  $\mu$ m Quartz Fiber with 3 nm and 6 nm Water Sheaths. The curve with the dots overlayed is the unclad case. The 3 nm curve deviates less than the 6 nm curve from the curve representing the unclad fiber.

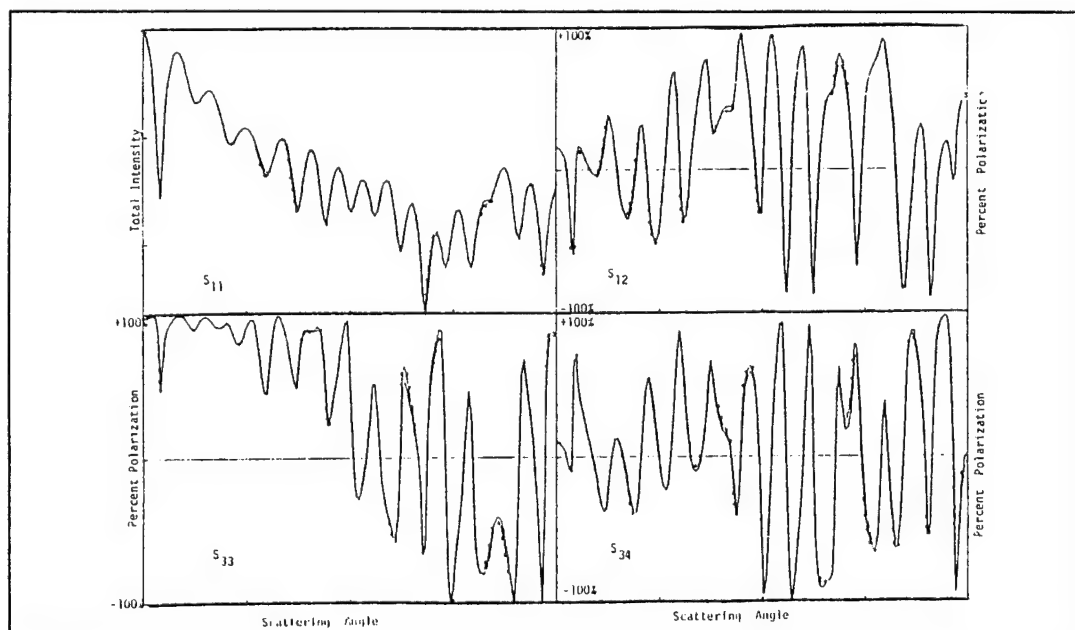


Figure 5.6. Scattering Curves of a Theoretical 1  $\mu$ m Quartz Fiber with a 10  $\mu$ m Sheath of  $n = 1.3130$  Water and  $n = 1.3330$  Water. The curve with the dots overlayed represents the lower index of refraction.

These calculations use the bulk index of refraction 1.3330 for the index of refraction of the water layer. An argument could be made that the layers are too thin to use  $n = 1.3330$ . Our experiments with near perfect fibers gives our best resolution ( $\Delta r$ ) at about 0.5 nm, or about 50 molecules of water in a line, assuming each has a diameter of  $10^{-11}$  m. At some thickness  $n$  will begin changing by small amounts, but the change would be small. In a water layer even fifty molecules (0.5 nm) thick, the inner forty should behave as a bulk material, because the outer sections would mask the boundary from the inner molecules. Figure 5.6 demonstrates the changes in the  $S_{ij}^*$  matrix elements for a one micron fiber if the index of a 10 nm layer of water were 1.3130 instead of 1.3330. Even this relatively large change causes only a small alteration in the  $S_{ij}^*$  elements (which tends toward the patterns of the uncoated fiber). Therefore we are not concerned about the possible minor changes in the index of refraction for very small sheath thicknesses.

## 5.2 The Humidity Chamber

After the best fibers were selected and calibrated, they were separately encased (one fiber at a time) within a controlled humidity environment. A schematic of this environment is shown in Figure 5.7. The chamber was a clear quartz cylinder with inner and outer radii equal those of the lid. The cylinder was attached to the lid rim with tape. A plastic lid, attached to the top of this cylinder, had three holes, one for the inlet for the water vapor and nitrogen or oxygen mixture, one for the egress of this flow, and one for the humidity probe. A latex sheath loosely enclosed the probe and its lid hole so that the gas and water vapor would flow through the

chamber and past the probe. The laser beam passed through the quartz chamber and struck the fiber, which scattered the beam into all angles  $\theta$ . The chamber did not change the phases or amplitudes of the fiber scattering patterns, except for a small but nearly uniform attenuation in the total intensity matrix element.

For humidity experiments, water vapor mixed with nitrogen or oxygen gas was sent into the chamber. The water vapor was produced by bubbling the carrier gas through a beaker filled with distilled water. The gas flow was controlled by valves before and after the beaker, and measured by a gauge located between the second valve and the chamber. The nitrogen was sent directly from its tank to the chamber to dry out the chamber. One or both gases in various mixtures could be sent into the chamber to create the desired humidities.

A Vaisala HM14 humidity probe and transmitting box recorded relative humidity levels within the chamber. The probe was calibrated with saturated LiCl, NaCl, and K<sub>2</sub>SO<sub>4</sub> solutions, each of which had a known humidity when in a sealed container at a certain temperature. The relative humidity for the lithium solution was 12.4%, for the sodium solution 75.5%, and for the potassium solution 97.2% at 20°C. A 0-20 mA output signal connected to a 500 ohm resistor produced a 0-10 V drop across the resistor which corresponded to a 0 to 100% humidity reading on a voltmeter. A strip chart recorded humidity during the  $\theta$ -scan.

The probe's response to rapid changes in humidity was not immediate, as shown in Figure 5.8. Its response time was measured by placing it in the jar containing the K<sub>2</sub>SO<sub>4</sub> solution (97.2% RH at 20°C). After it had reached a constant value, it was immediately placed in the jar containing the LiCl solution (12.4% RH at 20°C). The response was relatively linear, but

very slow (a decrease of 16% RH/min initially), because of the time needed to remove the small amount of water adsorbed onto the probe's capacitive plates. When the probe was pulled out of the  $K_2SO_4$  jar and left in room humidity, the response was immediate. We

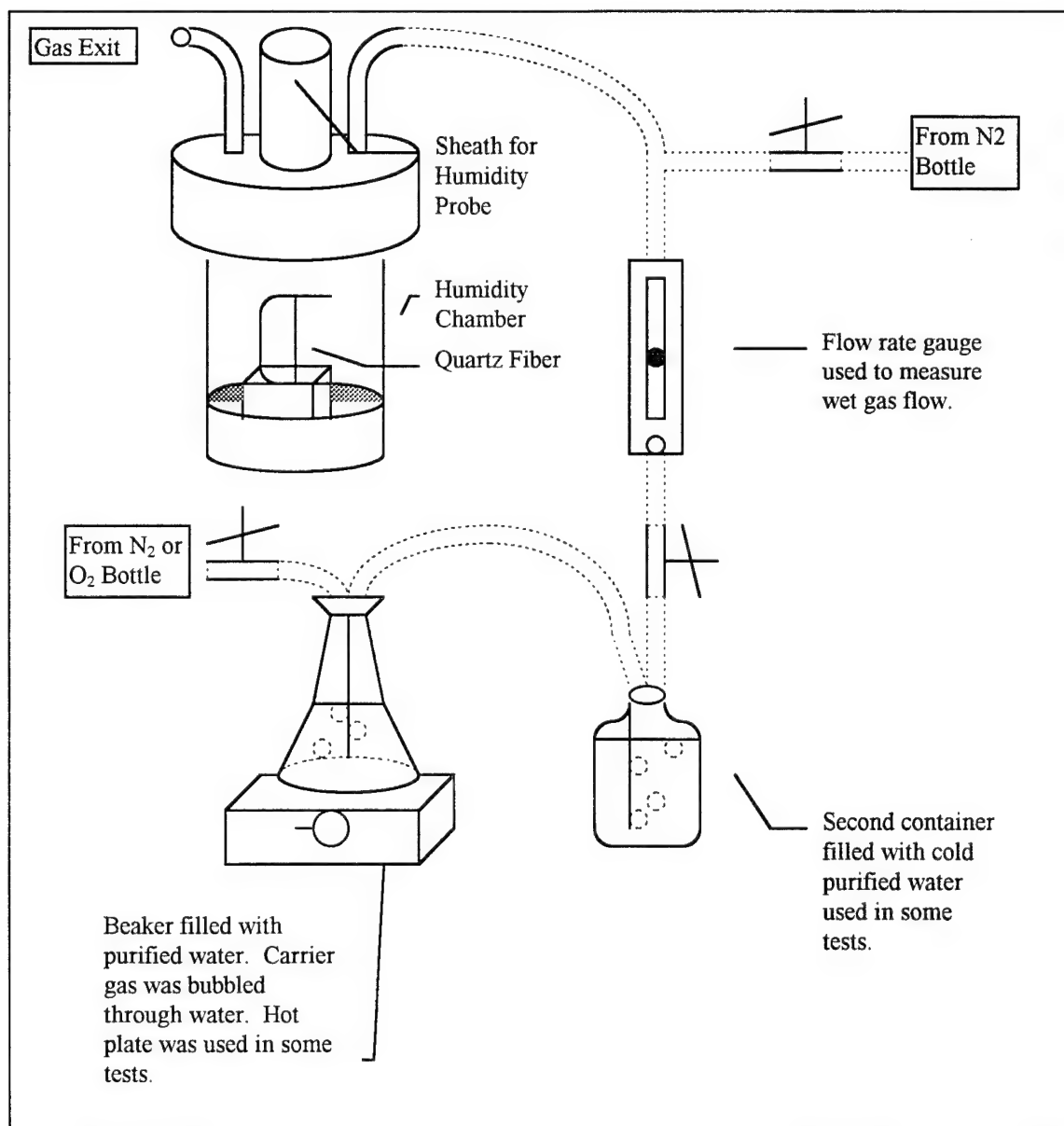


Figure 5.7. Diagram of Humidity Chamber. Two variations of the above arrangement were used. The first involved nitrogen as the carrier gas, no hot plate, no second container, and the first beaker filled with cotton balls. The second used oxygen as the carrier gas with all the equipment shown above.

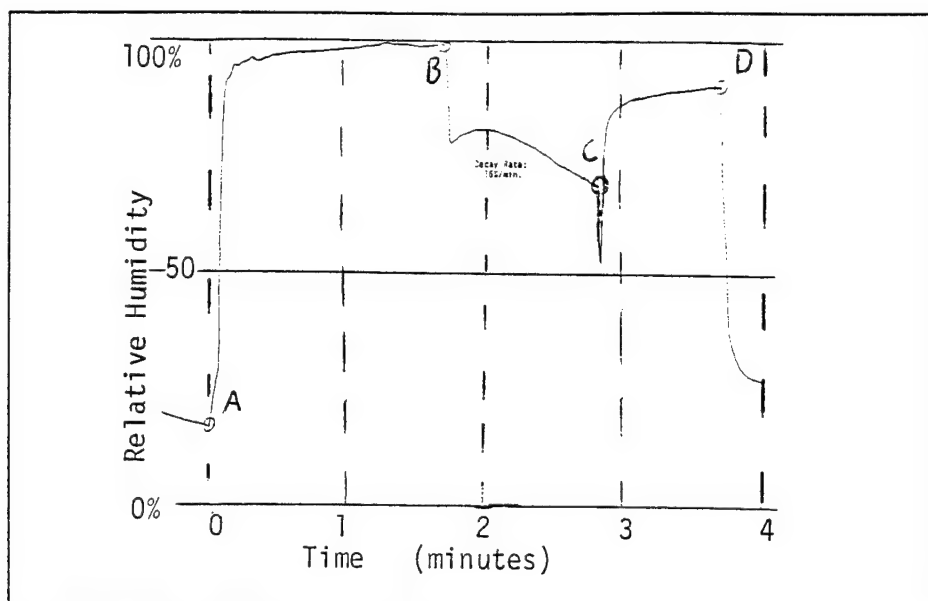


Figure 5.8. Response of Vaisala Probe to Static Humidity. The probe was placed in a saturated solution of  $K_2SO_4$  at 20°C (97.2% RH) at point A and a saturated solution of LiCl at the same temperature (12.4% RH) at point B. The probe went back in the potassium solution at point C, and then into air at point D.

expected that a constant flow of gas would rapidly carry the air away from the probe. This dynamic humidity system would be accurate because dry air would move water quickly off the plates, unlike the case of the lithium solution.

The probe was also sensitive to temperature differences. The Vaisala manual states that at a humidity of 90%, a one degree temperature difference between the measurement site and the site of interest (i.e. - right by the surface of the fiber) produces an error in the measurement of  $\pm 6\%$  RH. Since the fiber was located only two inches from the probe, and each was equidistant from the inlet port, the resulting temperature gradient was not large enough to influence the probe's measurement.

Scattering measurements of each fiber were now made again at different humidities. Before making measurements, we used the CLAD program to see where the theoretical  $S_{ij}(\theta)$  were

most sensitive to the sheath thickness. Each fiber was measured using a particular matrix element and angle which demonstrated significant change with increases in cladding thickness. First the  $S_{ij}^*$  matrix elements were measured at 30%-40% RH. Then dry nitrogen was passed through the chamber to clear it of water vapor and the same  $S_{ij}^*$  matrix elements were measured again. After this,  $S_{ij}^*$  matrix elements were measured at a humidity near 100%. We again measured the same matrix elements after the humidity was dropped below 50%. This produced curves corresponding to a fiber gaining a water sheath as a function of humidity. Another set of measurements were performed by setting the PMT at an angle known to be sensitive to changes in sheath thickness. The humidity was then slowly increased and decreased while measuring the  $S_{ij}^*$  matrix elements as a function of humidity.

## CHAPTER 6

### THE MEASUREMENTS

The radius of each fiber was determined by a best fit of the experimental  $S_{ij}^*(\theta)$  matrix elements (referred to as  $S_{ij}$  from this point forward) to the theoretical  $S_{ij}$  for Maxwell's equations. This gave us four fiber sizes (2.460  $\pm$  0.100  $\mu\text{m}$ , 1.3890  $\pm$  0.0005  $\mu\text{m}$ , 1.3525  $\pm$  0.0003  $\mu\text{m}$ , and 0.6215  $\pm$  0.0003  $\mu\text{m}$ ) for the humidity experiments. The  $S_{ij}$  were measured after dipping each fiber in purified water. This showed whether the fibers were wettable and would allow water to be adsorbed on them. Also, the  $S_{ij}$  were measured for each fiber before and after filling the base of the fiber mount with purified water and placing the fiber in the quartz chamber to see if the growth of a water sheath was possible from airborne water molecules ( $\sim$  94% RH).

The fiber was placed in the chamber and the humidity probe inserted. Dry nitrogen was cycled through the chamber and the  $S_{ij}$  were measured. Then the humidity in the chamber was raised close to 100% RH and the  $S_{ij}$  again measured. The humidity was then lowered below 40% RH by flowing dry nitrogen into the chamber, and the  $S_{ij}$  again measured to determine what long term effect the water layer had on the fiber. The  $S_{ij}$  at a certain fixed  $\theta$  were also measured as a function of humidity and flow rate.

## 6.1 The Thick Fiber (Fiber F, 2.460 $\mu\text{m}$ )

The thickest quartz fiber we used ( $2.460 \pm 0.100 \mu\text{m}$ ) was easily visible to the naked eye and a strong scatterer. The  $S_{ij}$ , shown in Figure 6.1.1, are characterized by a large number of oscillations within the 180 degree scan. These curves were compared to theoretical  $S_{ij}$  for fibers of differing radii. Figure 6.1.2 shows the theoretical  $S_{ij}$  for a 2.460  $\mu\text{m}$  quartz fiber (the best fit to the experiment). Matching the two  $S_{ij}$  gives the sheath thickness to within 0.100  $\mu\text{m}$ .

### 6.1.1 Technique of Comparing Experimental and Theoretical Results

Figure 6.1.3 shows the theoretical  $S_{ij}$  of a 2.460  $\mu\text{m}$  fiber with cladding layers, 2.5 nm and 5 nm thick. Even these small radius changes ( 0.1 and 0.2 %, respectively ) produced significant changes in the  $S_{ij}$ , especially for the  $S_{12}^*$ ,  $S_{33}^*$ , and  $S_{34}^*$  curves in the backscatter range of  $120^\circ$  to  $160^\circ$ .

Figure 6.1.4 shows the experimental  $S_{12}^*$  for Fiber F dry (solid line) and after being dipped in purified water (dashed line). Significant differences occur in the backscatter at about  $105^\circ$  and  $170^\circ$ . A unidirectional change of the entire  $S_{ij}$  would indicate an error in the normalization and not the growth of a water layer. Figure 6.1.4 shows substantial changes in polarization amplitudes between experiment and theory, indicating a substantial change in radius. Figure 6.1.4 also shows about a 10% increase in the percent polarization of six peaks located between  $75^\circ$  to  $95^\circ$  (region labeled A in the figure). Most of the corresponding peaks in the theoretical  $S_{12}^*$  of Figure 6.1.3 increase in polarization.

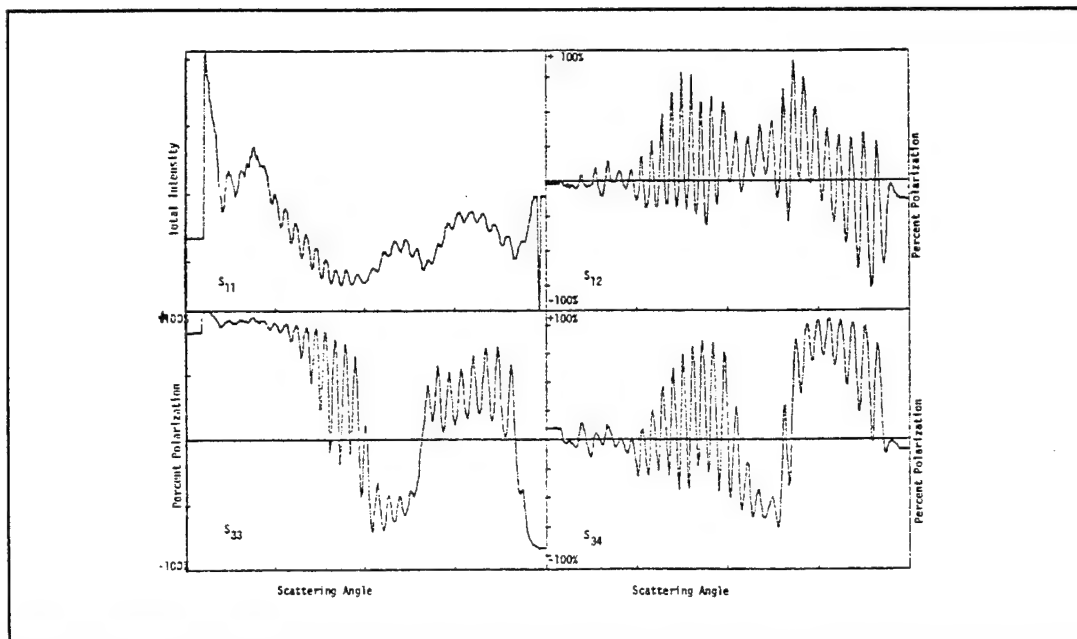


Figure 6.1.1. The Four Experimental Scattering Curves for Test Fiber F. The quartz fiber was cleaned with acetone and placed in the quartz chamber before the test.

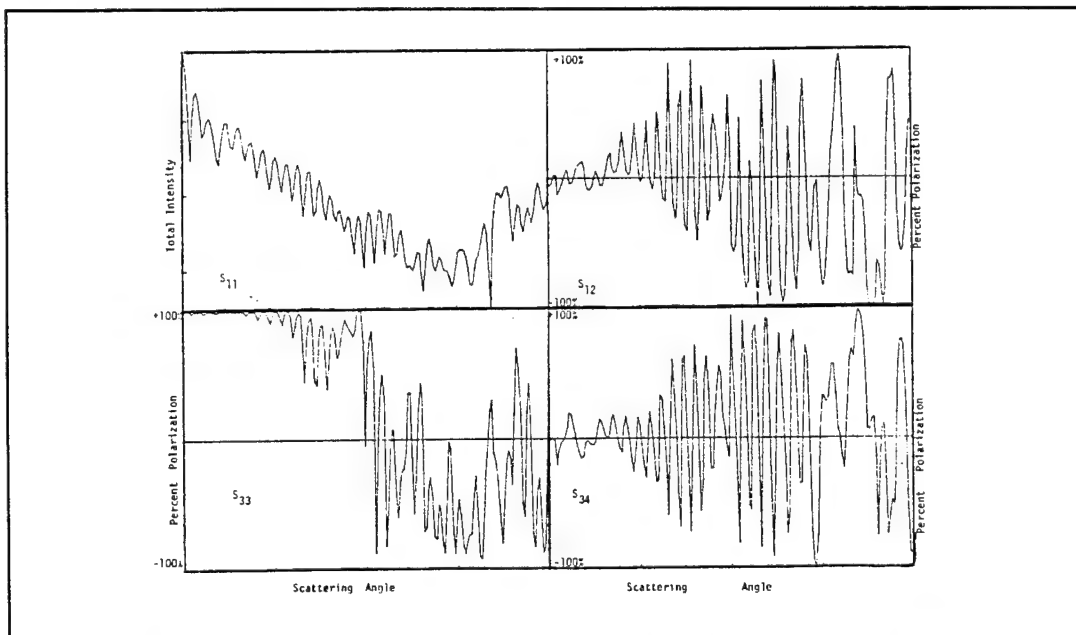


Figure 6.1.2. The Four Theoretical Scattering Curves for a 2.460  $\mu\text{m}$  Quartz Fiber. This radius produced solutions to Maxwell's equations whose matrix elements most closely matched the experimental matrix elements in Figure 6.1.1.

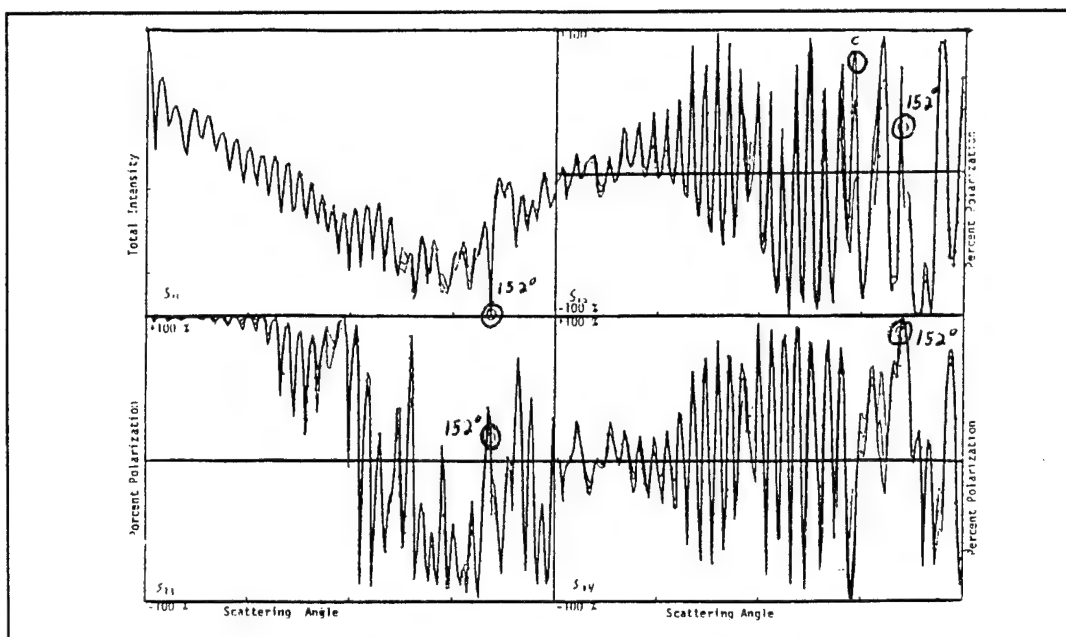


Figure 6.1.3. The Four Theoretical Scattering Curves for a 2.460  $\mu\text{m}$  Quartz Fiber with No Cladding, a 2.5 nm and a 5.0 nm Thick Water Layer. The curve with the dots overlaid is the solution for a 5.0 nm cladding layer. The 2.5 nm solution deviates a small amount in places, and the uncladded solution deviates a bit more from the dotted curve.

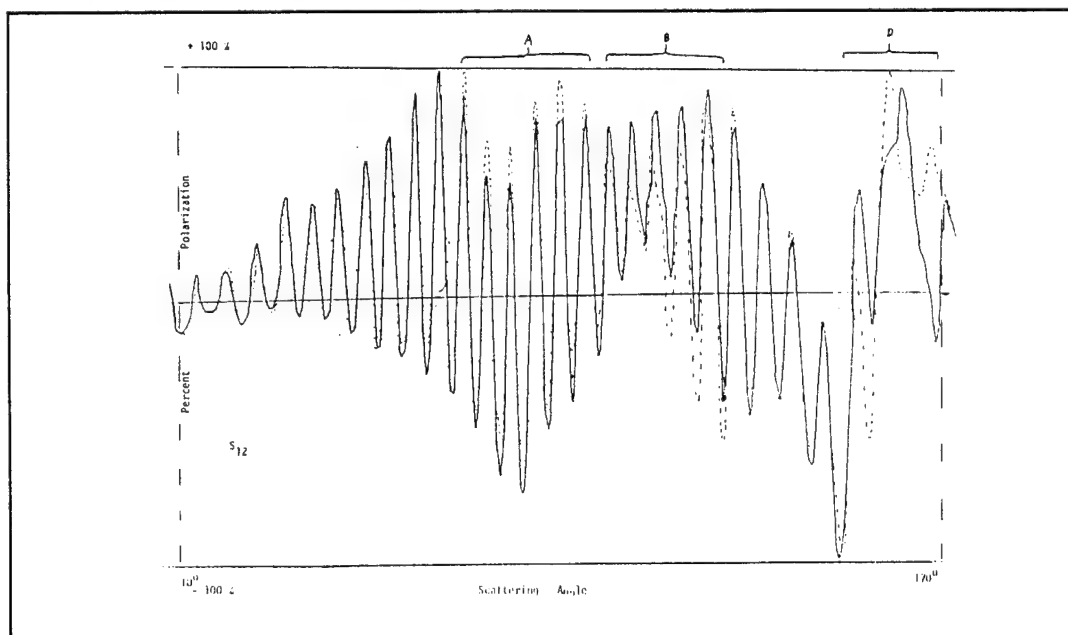


Figure 6.1.4. The Experimental  $S_{12}^*$  Scattering Curves for Fiber F Cleaned in Acetone and Dipped in Water. The solid line is the curve for the clean fiber, and the dotted line is the curve for the fiber after it was dipped in purified water.

The size of this increase lies between the 2.5 nm and the 5 nm theoretical curves. We estimate a 4 nm sheath thickness. Next the experimental curve section labeled B shows that most of the peak amplitudes decreased by about 15%. Figure 6.1.3 reveals only one major change in polarization of the theoretical  $S_{ij}$  for the fiber with the 5 nm sheath in this range (labeled C) which is larger than any single change in section B of the experimental curve. However, because there are more of the smaller changes in the experimental  $S_{ij}$ , we place the new estimate for the sheath thickness at 4-5 nm. Significant change in the percent polarization occurs in the extreme backscatter (section labeled D). Here, the experimental curve has not only changed amplitude (up to 60% in places), but also shifted phase. Comparing this to the corresponding section of the theory curve shows no match. However, because the other experimental sections matched the theory for the 5 nm water layer, the sheath thickness could be only slightly larger than 5 nm. Therefore, by comparing these two curves, we assign 8 nm as the water sheath thickness.

Another theoretical curve, Figure 6.1.5, also suggests a sheath thickness of about 8 nm. It shows how the  $S_{ij}$  varies at a fixed scan angle  $\theta$  as a function of the water sheath thickness on a theoretical 2.460  $\mu\text{m}$  fiber. The  $S_{ij}$  are calculated at three fixed angles ( $148^\circ$ ,  $150^\circ$ , and  $152^\circ$ ) for sheath thicknesses ranging from zero to 40 nm. The location of  $\theta = 152^\circ$  on each of the four curves in Figure 6.1.2 has been marked on the  $S_{11}$ ,  $S_{12}^*$ ,  $S_{33}^*$ , and  $S_{34}^*$  curves. Among the  $\theta = 152^\circ$  points, the one on the  $S_{12}^*$  curve in Figure 6.1.2 is the most sensitive. As the sheath thickness increases to 5 nm, the percent polarization at that angle increases by about 40%. This is also shown on the  $152^\circ$  curve of the  $S_{12}^*$

element in Figure 6.1.5. As the sheath thickness (the independent variable of Figure 6.1.5) increases from 0 to 5 nm, the percent polarization increases almost linearly from 40% to 80%.

Figure 6.1.5 suggests 8 nm as the best fit because large polarization changes occur for small changes in this sheath thickness. For example, the polarization of the  $152^\circ S_{12}^*$  curve drops from 80% to -10% with the addition of only one nanometer of water to a theoretical 2.460  $\mu\text{m}$  fiber with an 8 nm sheath already on it. This same degree of change was observed in section D of Figure 6.1.4. Therefore, even though the theoretical and experimental curves do not match exactly, they can be used to establish a range of water sheath thicknesses.

### 6.1.2 Static Humidity Contribution to Sheath Thickness

When the lid of the mount for Fiber F (2.460  $\mu\text{m}$ ) was filled with water, the fiber was exposed to a humidity close to 94% RH. Figure 6.1.6 shows the results. The  $S_{12}^*$  response is much smaller than for the fiber dipped in water. The experimental  $S_{12}^*$  matches the theoretical 2.5 nm  $S_{12}^*$  (see Figure 6.1.3) more closely than the 5 nm  $S_{12}^*$ . A sheath thickness is obtained by comparing the peak amplitudes in the experimental curve, which change uniformly by 10%, with those of the theoretical curve for the 2.5 nm water sheath, which change in places by 50%. Our best estimate in this case is 2 nm for the sheath thickness.

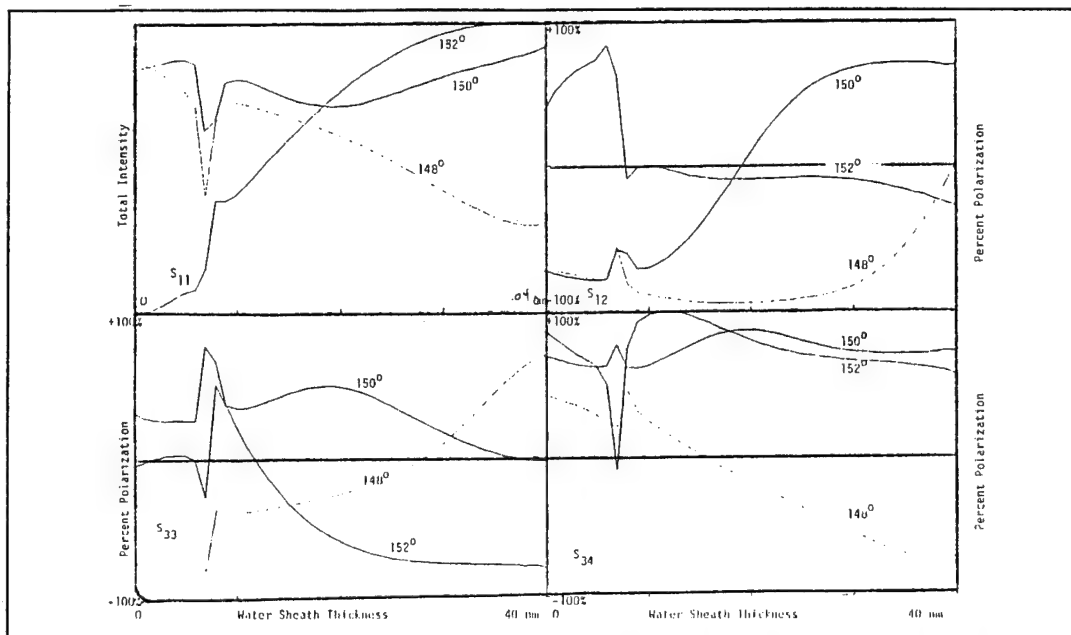


Figure 6.1.5. The Four Theoretical Curves for Changes in Total Intensity and Percent Polarization at a Fixed Angle as a Function of Water Layer Thickness on a 2.460  $\mu\text{m}$  Quartz Fiber. In this case, the x-axis gives the water layer thickness instead of the scattering angle  $\theta$ .

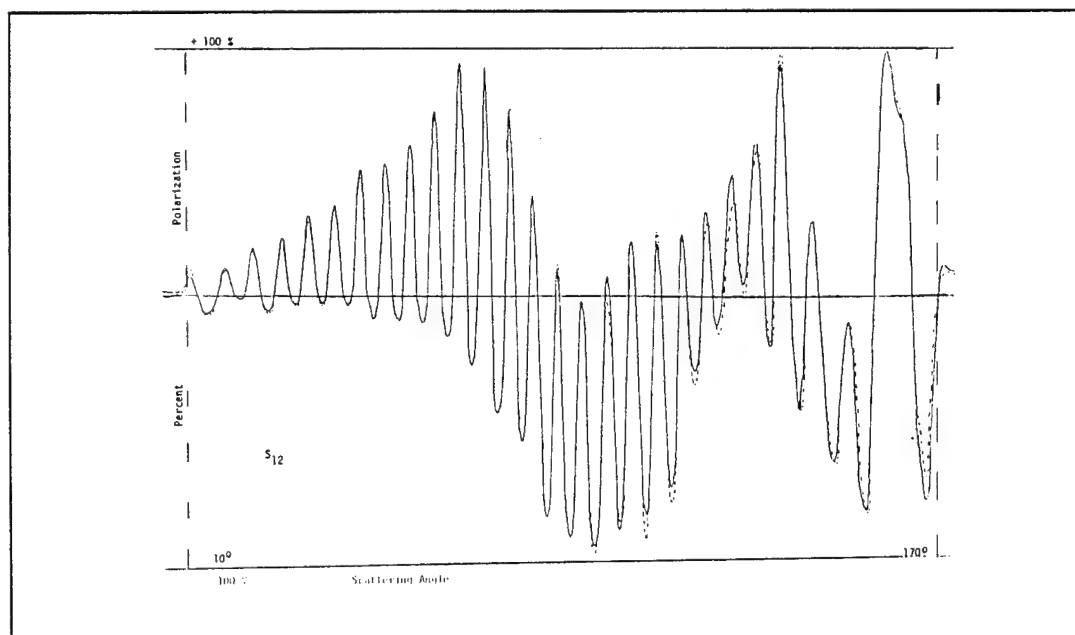


Figure 6.1.6. The Experimental  $S_{12}^*$  Scattering Curves for Fiber F Cleaned in Acetone and Exposed to High Static Humidity. The solid line is the scattering curve for the clean fiber, and the dotted line is the scattering curve for the fiber after its mount was filled with water. In both cases, the quartz chamber was in place attached to the fiber mount.

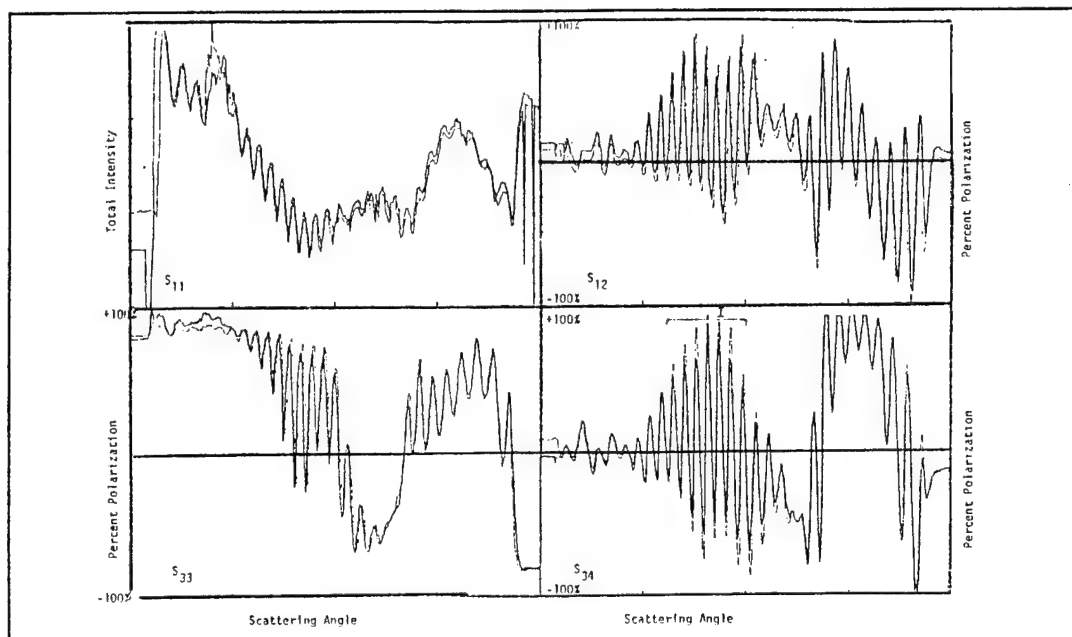


Figure 6.1.7. The Four Experimental Scattering Curves for Fiber F Exposed to 0% RH and 95%RH. The lightly shaded curves are the matrix elements for the low humidity, and the darker curves are the matrix elements for the high humidity.

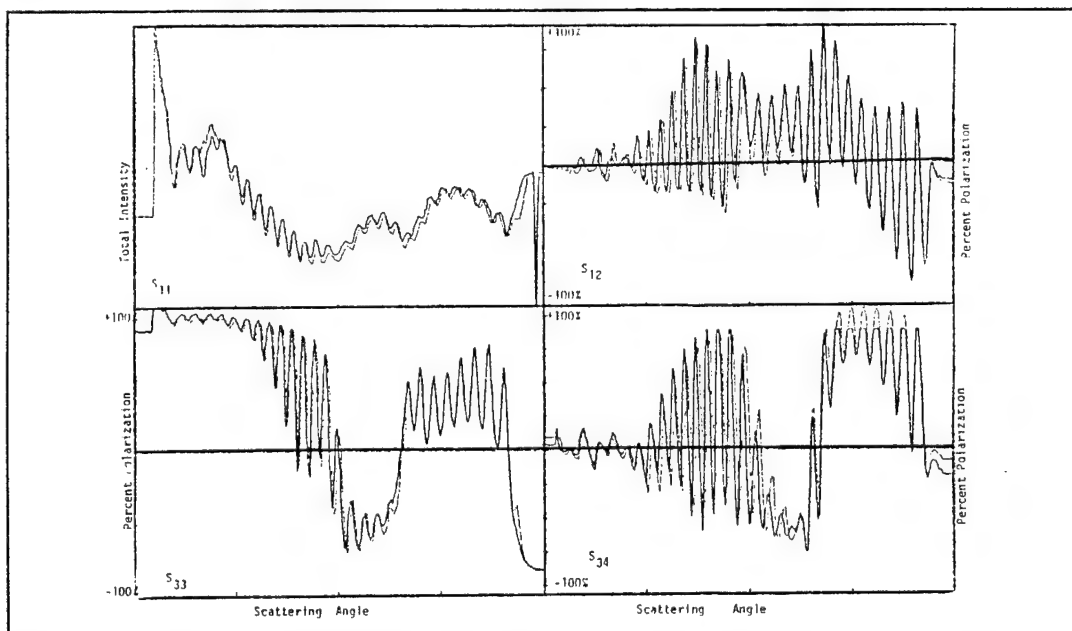


Figure 6.1.8. The Four Experimental Scattering Curves for Fiber F Exposed to 0% RH Initially and 0% RH after Three Consecutive 95% RH Exposures. The lightly shaded curves are the matrix elements for the clean fiber, and the darker curves are the matrix elements for the fiber after it was exposed to 95%RH.

### 6.1.3 Dynamic Humidity Contributions to Sheath Thickness

The  $S_{ij}$  were also measured for Fiber F as a function of humidity while a humid carrier gas was flowing through the chamber. Nitrogen was bubbled through a beaker filled with purified water and cotton balls at room temperature. Oxygen was also used because its higher molecular weight gave an improved water solubility, allowing more water molecules per unit volume of carrier gas to reach the chamber. The oxygen was bubbled through hot, then cold, purified water. Pure dry nitrogen was the drying agent.

Figure 6.1.7 shows two sets of experimental  $S_{ij}$  for Fiber F: one for 0% RH and one for 95% RH. Both sets of curves were measured while the humid gas was flowing through the chamber. The  $S_{ij}$  shows some horizontal displacement, but the only significant region of change is marked I on the two  $S_{34}^*$  curves of Figure 6.1.7. The smaller percent polarizations of the high humidity scattering curve, after comparison with the theoretical  $S_{ij}$  in Figure 6.1.3, are attributed to a water sheath. The sheath thickness which best fits the measurements is 1.5 to 2 nm.

Figure 6.1.8 shows two sets of experimental  $S_{ij}$  for Fiber F: one at 0% RH and at 0% RH after the fiber was exposed to 96% RH three times. The forward scatter of the  $S_{12}^*$  curve shows a 5% change in percent polarization. The last peak of the  $S_{33}^*$  curve disappears. A new peak forms on  $S_{34}^*$  at  $\theta = 110^\circ$ . These changes give a fit of 1.5 nm.

The humid oxygen gas gave  $S_{ij}$  measurements similar to those recorded when humid nitrogen gas was used. Figures 6.1.9, 6.1.10, and 6.1.11 show the data. Figure 6.1.9

shows two  $S_{12}^*$  for Fiber F: one for 37% RH (solid line) and one for 93% RH (dashed line). The curves are quite similar over all 180 degrees. A horizontal shift is evident and a significant amplitude change (greater than 5%) occurs near  $170^\circ$ .

Figure 6.1.10 shows two more  $S_{12}^*$  for Fiber F: one for 37% RH (solid line) and one for 96% RH (dashed line). For these cases the vapor entering the chamber is slightly hotter and is supplied at a higher flow rate, causing a significant change in the  $S_{ij}$ . The polarization amplitude of the forward scatter ( $\theta = 90^\circ$ ) is attenuated by about  $\pm 5\%$ . The angular displacement is more pronounced. The average amplitude change in the backscatter is 5%, except in the final peak, which changes by 10%.

Figure 6.1.11 shows two more  $S_{12}^*$  for Fiber F: one for 37% RH (solid line) and one at 40% RH after the fiber was exposed once to 96%RH. A slight difference in the  $S_{12}^*$  occurs near  $\theta = 10^\circ$ , while near  $\theta = 170^\circ$  the curves almost coincide. Exposure to 93% RH (Figure 6.1.9) caused a one-nanometer water sheath to form, and exposure to 96% RH (Figure 6.1.10) caused a 2-2.5 nm water sheath to form. After the chamber was flooded with dry nitrogen, the fiber retained a 1 nm water sheath.

#### 6.1.4 Percent Polarization at a Set Angle as a Function of Humidity

In these experiments we set the PMT at an angle where the  $S_{ij}$  was particularly sensitive to humidity changes. The  $S_{ij}$  and relative humidity are recorded simultaneously. In Figure 6.1.7, the letter J on the  $S_{12}^*$  curve marks a peak ( $\theta = 88^\circ$ ) which changes by 10% as the humidity is raised from 0% to 95% RH. Figure 6.1.12 shows how the  $S_{ij}$  at  $\theta$

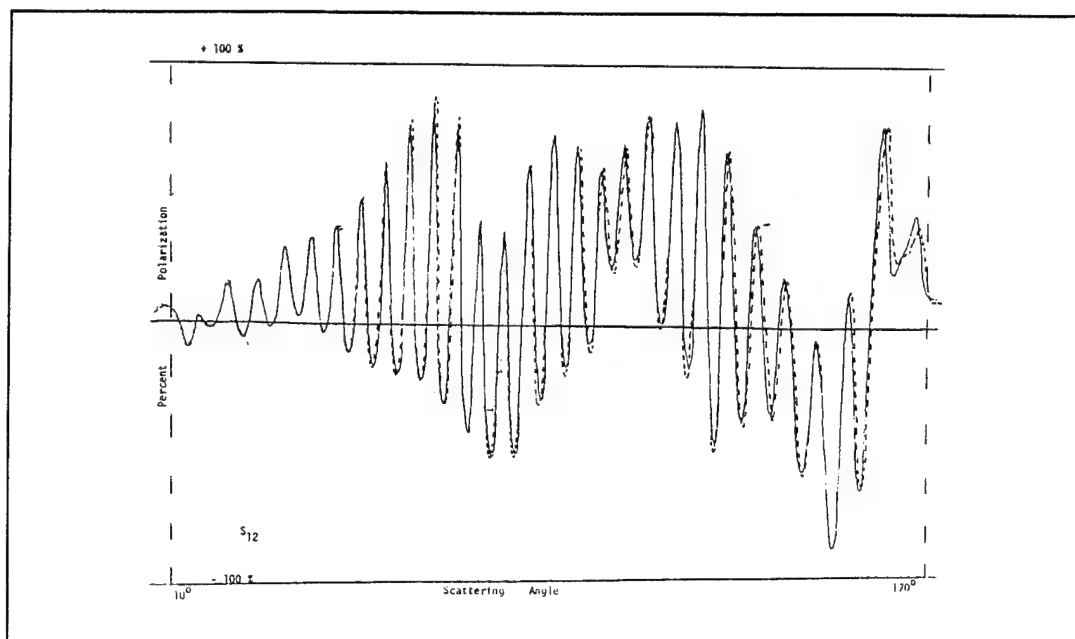


Figure 6.1.9. The Experimental  $S_{12}^*$  Scattering Curves for Fiber F Exposed to 37% RH and 93% RH (Second Test). The solid line is the matrix element for the dry fiber, and the dotted line is the matrix element for the fiber in high humidity.

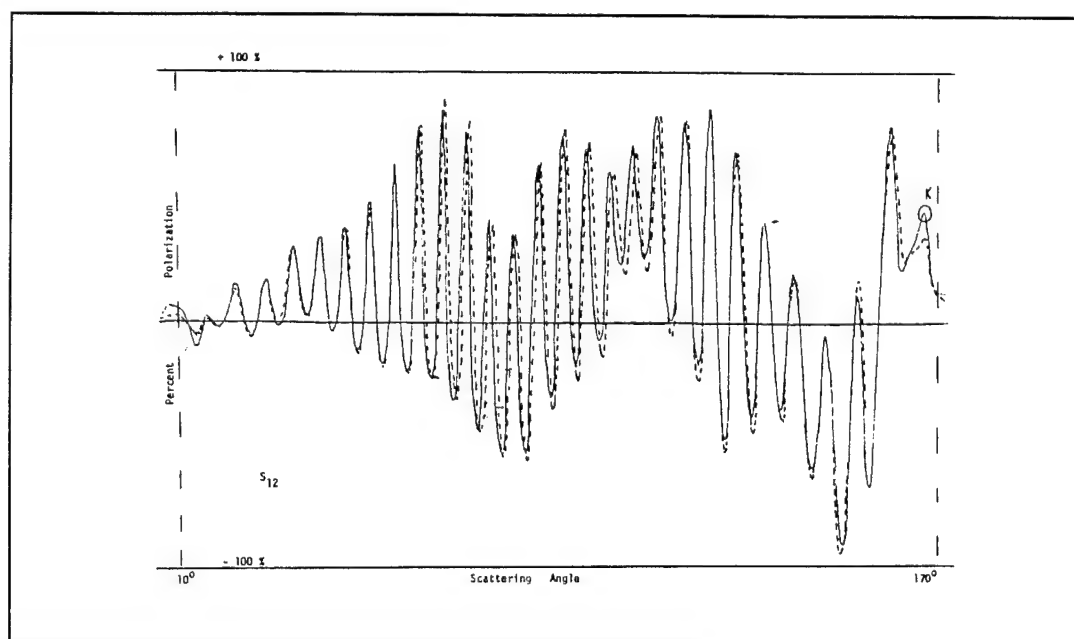


Figure 6.1.10. The Experimental  $S_{12}^*$  Scattering Curves for Fiber F Exposed to 37% RH and 96% RH (Second Test). The solid line is the matrix element for the dry fiber, and the dotted line is the matrix element for the fiber in high humidity.

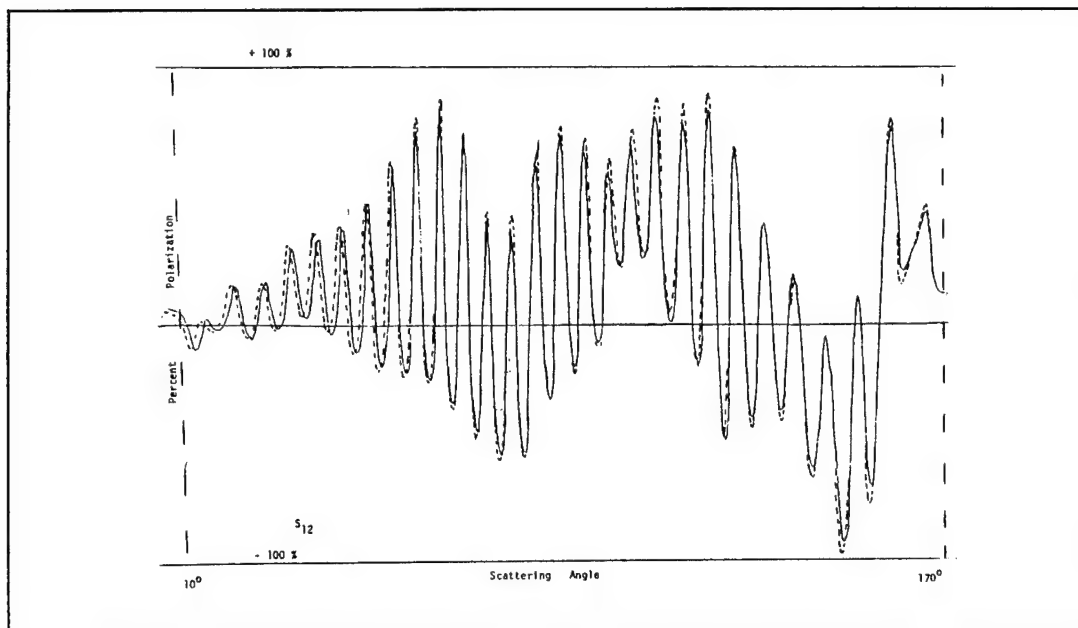


Figure 6.1.11. The Experimental  $S_{12}^*$  Scattering Curves for Fiber F Exposed to 37% RH and 40% RH after a 96% RH Exposure (Second Test). The solid line is the matrix element for the dry fiber, and the dashed line is the matrix element for the fiber after it was exposed to high humidity.

$= 88^\circ$  varies with humidity. However, there is a small lag in the  $S_{ij}$  response because the probe response is slow as the humidity approaches saturation (see Figure 5.8).

After correction, the  $S_{ij}$  is plotted against the relative humidity (shown in Figure 6.1.13). The  $S_{ij}$  increases linearly to 85% RH, then rises more rapidly to a maximum at 94% RH. When the flow is turned off, the  $S_{ij}$  drops slightly (see Figures 6.1.12 and 6.1.13). Either the flow rate forces water molecules onto the fiber, or the flow causes an increase in chamber humidity which is not immediately detected by the probe. The decrease of the water layer as the humidity is decreased proceeds at about the same rate as the increase, but the polarization does not return to its initial level. A thin sheath remains

on the fiber when the humidity is decreased to 0% RH. The sheath remained as long as nitrogen flowed through the chamber at the low rate used previously.

The same procedure was used for the oxygen humidity system. Here we measured the  $S_{12}^*$  at  $\theta = 170^\circ$  (see Figure 6.1.10, labeled point K). The polarization varied by about 10% between measurements at 37% RH and 96% RH. The humidity dependent data has been corrected for the humidity probe lag and plotted in Figure 6.1.14. Figure 6.1.15 shows the polarization as a function of the flow rate of the wet gas. The humidity reading was independent of flow rate.

The curves in Figure 6.1.14 are analogous to those in Figure 6.1.13, except that the  $S_{ij}$  at this angle decreases with increasing sheath thickness. The polarization change at this angle is linear up to 90% RH, after which it decreases more rapidly. Figure 6.1.15 shows that the flow rate strongly affects the  $S_{ij}$  for flow rates below  $13.4 \text{ cm}^3/\text{min}$ . As the flow rate was lowered from a maximum, the water sheath came off less readily than it went on.

We can assign sheath thicknesses based upon changes in  $S_{ij}$  if these changes are functions of the adsorbed water layer. Figure 6.1.5 shows that sheath thickness variations cause linear changes in  $S_{ij}$  (only at the angles shown) below 8 nm.

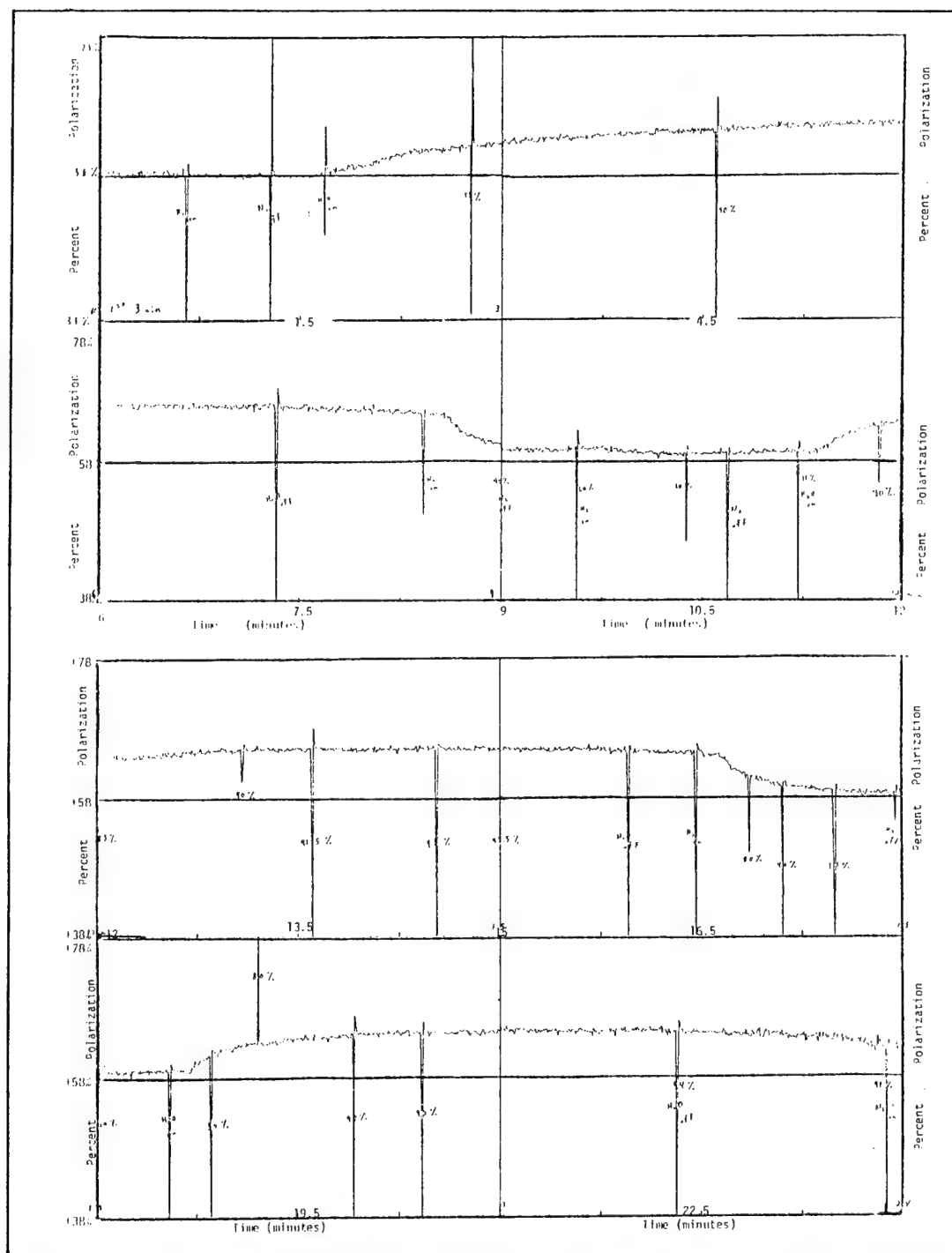


Figure 6.1.12. The  $S_{12}^*$  Percent Polarization Response of Fiber F at  $\theta = 88^\circ$  to Variable Humidities. The x-axis of these graphs is actually time, but the humidity was varied to different levels over that time. The approximate humidities are written directly on the graphs. The actual humidities were obtained by recording the instantaneous humidities on a strip chart record and correcting for the lag in the probe response.

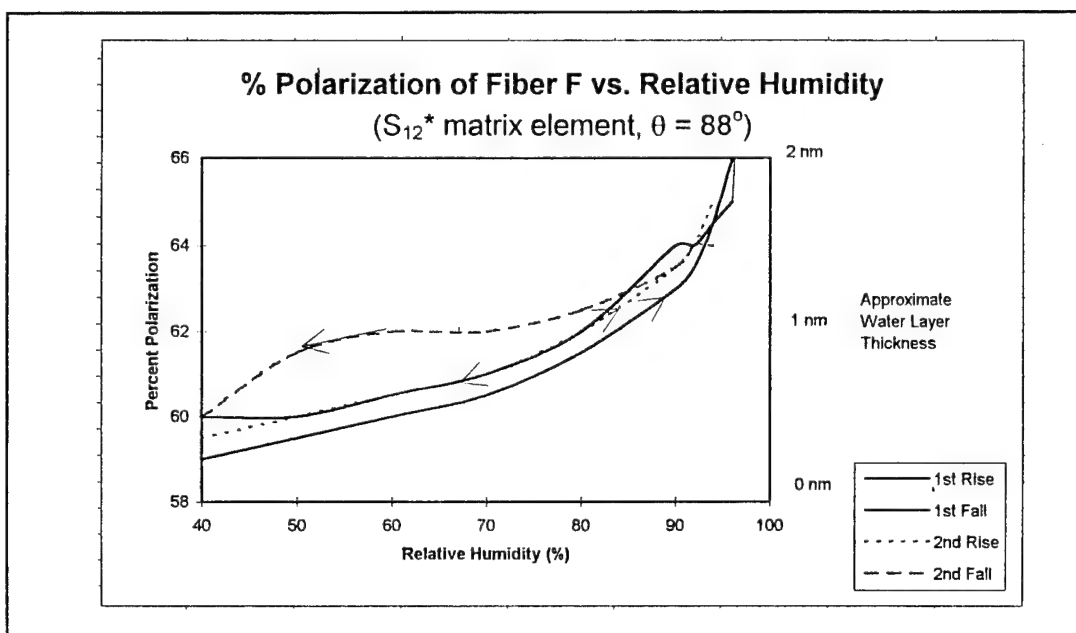


Figure 6.1.13. The Corrected  $S_{12}^*$  Percent Polarization Response of Fiber F at  $\theta = 88^\circ$  to Variable Humidities. The x-axis shows the humidities the fiber was exposed to, corrected for the lag in probe response.

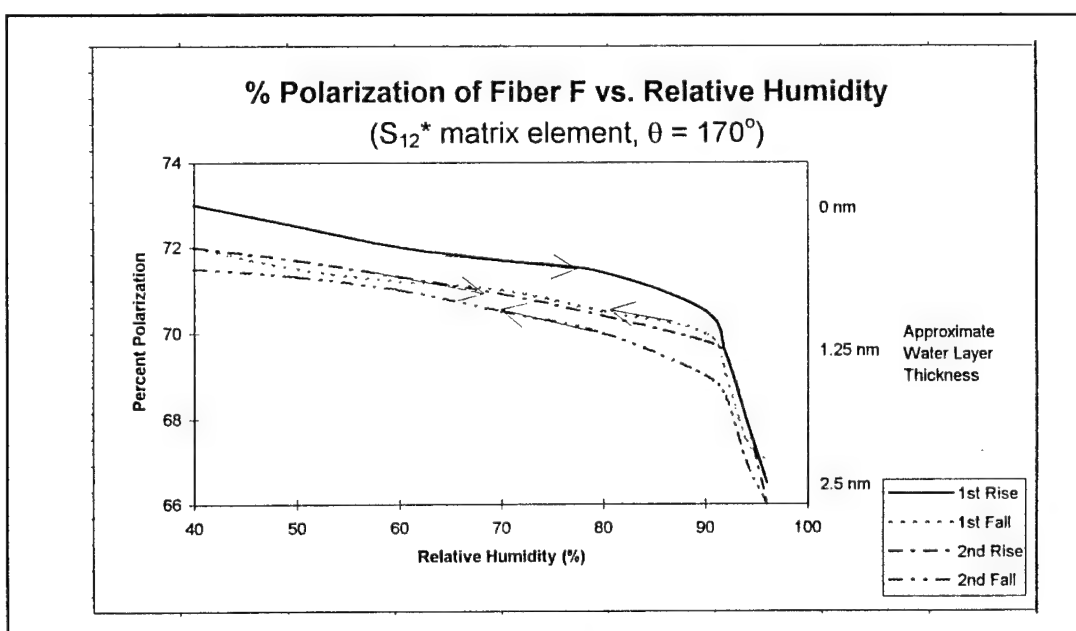


Figure 6.1.14. The Corrected  $S_{12}^*$  Percent Polarization Response of Fiber F at  $\theta = 170^\circ$  to Variable Humidities (Second Test). The x-axis shows the humidities the fiber was exposed to, corrected for the lag in probe response.

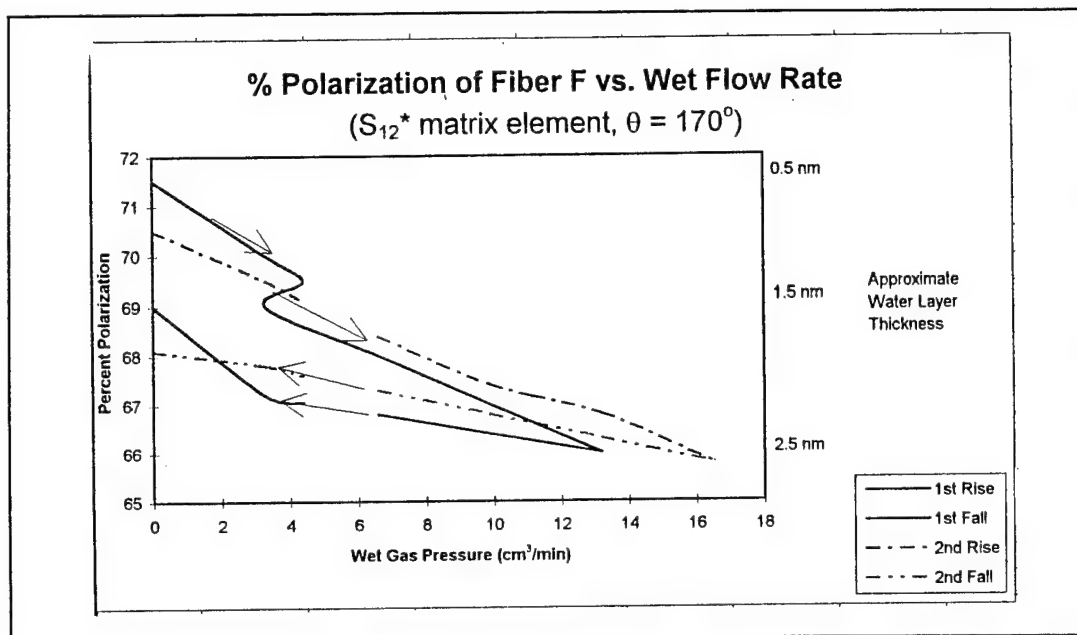


Figure 6.1.15. The Corrected  $S_{12}^*$  Percent Polarization Response of Fiber F at  $\theta = 170^\circ$  to Variable Flow Rates (Second Test). Humidity was read by the probe as between 93% and 96% for all flow rates.

## 6.2 The Intermediate Fibers (Fibers C, 1.3525 $\mu\text{m}$ , and D, 1.3890 $\mu\text{m}$ )

We chose two quartz fibers to investigate the  $S_{ij}$  as a function of relative humidity for the intermediate size category. The experimental  $S_{ij}$  for Fiber C and D are shown in Figure 4.6 and 6.2.1. The theoretical  $S_{ij}$  for Fiber C (1.3525  $\pm$  0.00025  $\mu\text{m}$ ) is given in Figure 4.6, and the theoretical  $S_{12}^*$  for Fiber D (1.3890  $\pm$  0.0003  $\mu\text{m}$ ) is given in Figure 6.2.2.

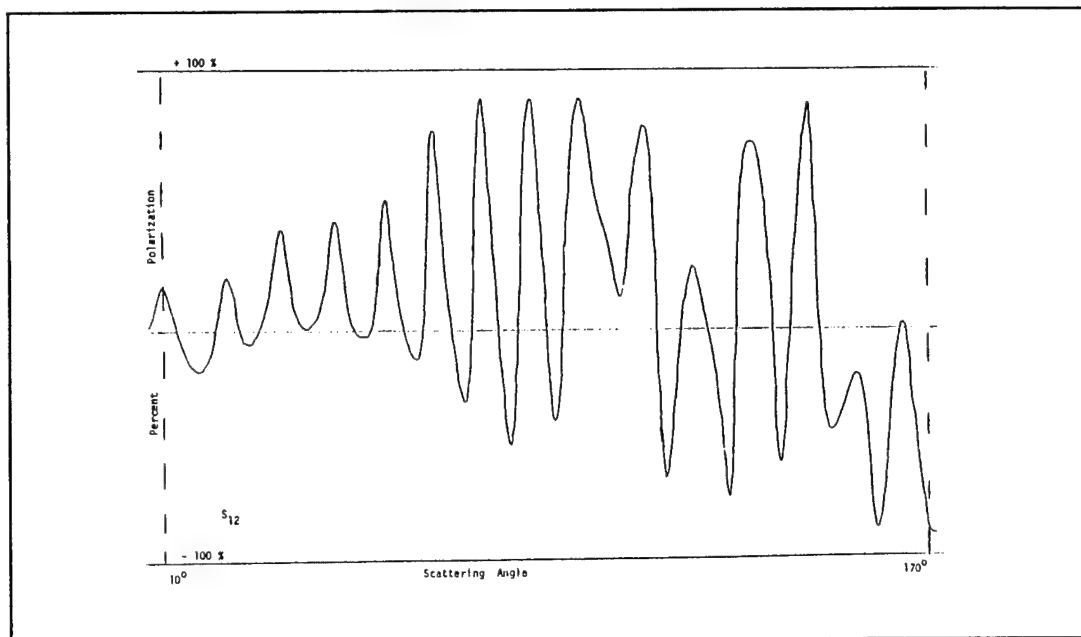


Figure 6.2.1. The Experimental  $S_{12}^*$  Scattering Curve for Test Fiber D. The quartz fiber was cleaned with acetone and placed in the quartz chamber before the test.

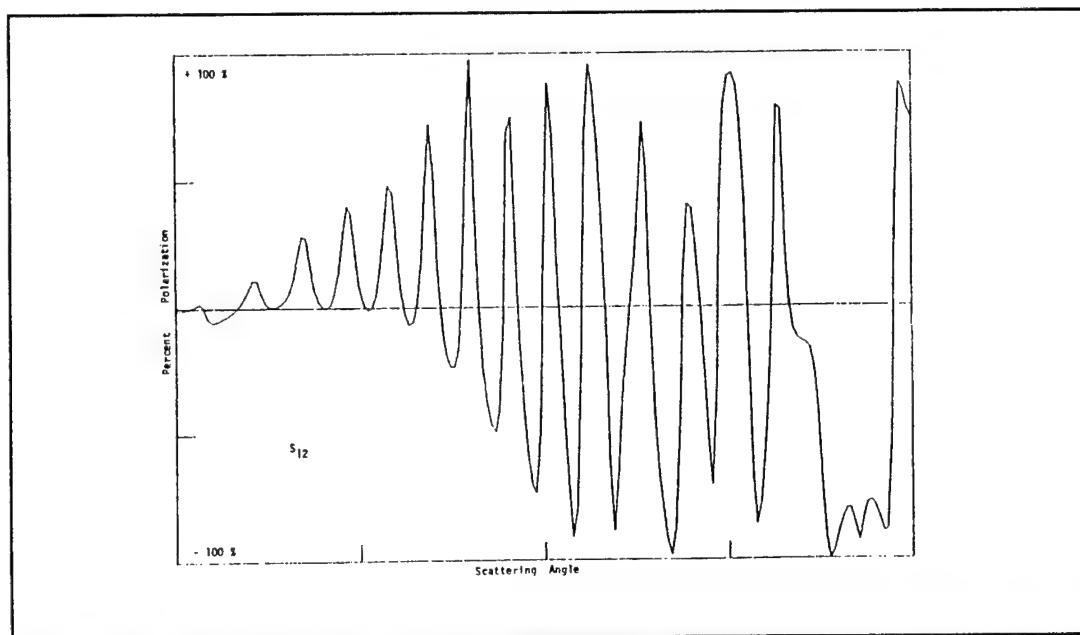


Figure 6.2.2. The Theoretical  $S_{12}^*$  Scattering Curve for a 1.3890  $\mu\text{m}$  Quartz Fiber. This radius produced solutions to Maxwell's equations whose matrix elements most closely matched the experimental matrix elements in Figure 6.2.1.

### 6.2.1 Direct Exposure Contribution to Sheath Thickness

Fiber D was cleaned with acetone and then dipped in water. The experimental  $S_{12}^*$  is shown in Figure 6.2.3. Near  $\theta = 110^\circ$  the polarization shifts by almost 100%. The amplitude of most peaks have changed. Figure 6.2.4 shows the theoretical  $S_{12}^*$  for an uncoated 1.3890  $\mu\text{m}$  fiber and that fiber with a 2.5 nm and a 5.0 nm water sheath. The experimental  $S_{12}^*$  most closely matches the theoretical  $S_{12}^*$  for a 1.3740  $\mu\text{m}$  quartz fiber with a cladding layer which is 10 nm thick (see Figure 6.2.5).

### 6.2.2 Static Humidity Contribution to Sheath Thickness

The  $S_{12}^*$  for Fiber D after the lid of the fiber mount was filled with water is shown in Figure 6.2.6. The changes in  $S_{12}^*$  do not match the corresponding changes in Figure 6.2.5. Most peaks are attenuated, and one large 50% decrease occurs near  $160^\circ$ . Therefore, the sheath thickness is close to 6 - 7 nm. The change in backscatter in the experimental curve is greater than that seen in the corresponding region of the 5 nm theoretical  $S_{ij}$  (50% polarization change in the experiment compared to a maximum of about 10% in the theory).

### 6.2.3 Dynamic Humidity Contribution to Sheath Thickness

Nitrogen supplied the water vapor for Fiber C, and oxygen supplied the water vapor for Fiber D. The same equipment was used as described in section 6.1.3. The

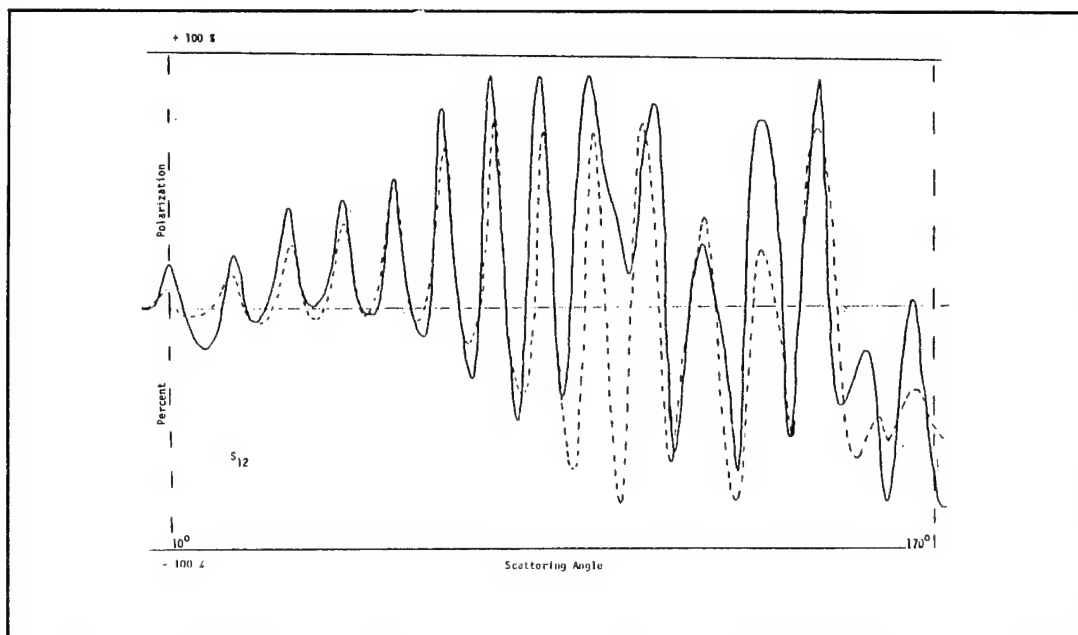


Figure 6.2.3. The Experimental  $S_{12}^*$  Scattering Curves for Fiber D Cleaned in Acetone and Dipped in Water. The solid line is the curve for the clean fiber, and the dotted line is the curve for the fiber after it was dipped in purified water.

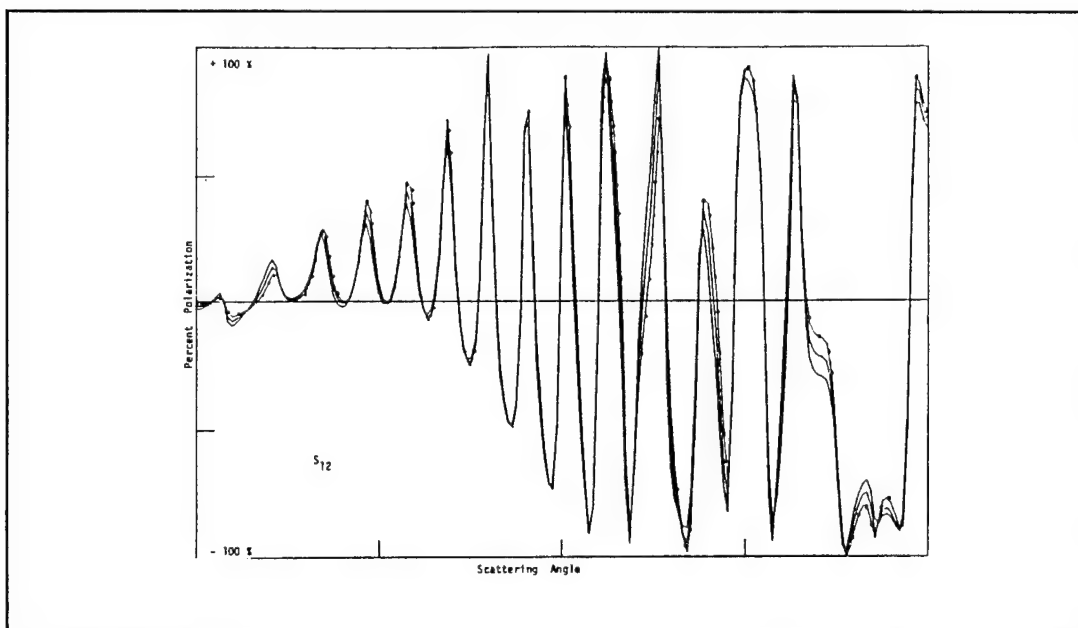


Figure 6.2.4. The Theoretical  $S_{12}^*$  Scattering Curves for a 1.3890  $\mu\text{m}$  Quartz Fiber with No Cladding, a 2.5 nm and a 5.0 nm Thick Water Layer. The curve with the dots overlaid on it corresponds to the theoretical fiber with no sheath. The 2.5 nm curve shows small changes, and the curve matching the 5.0 nm clad fiber showed larger changes.

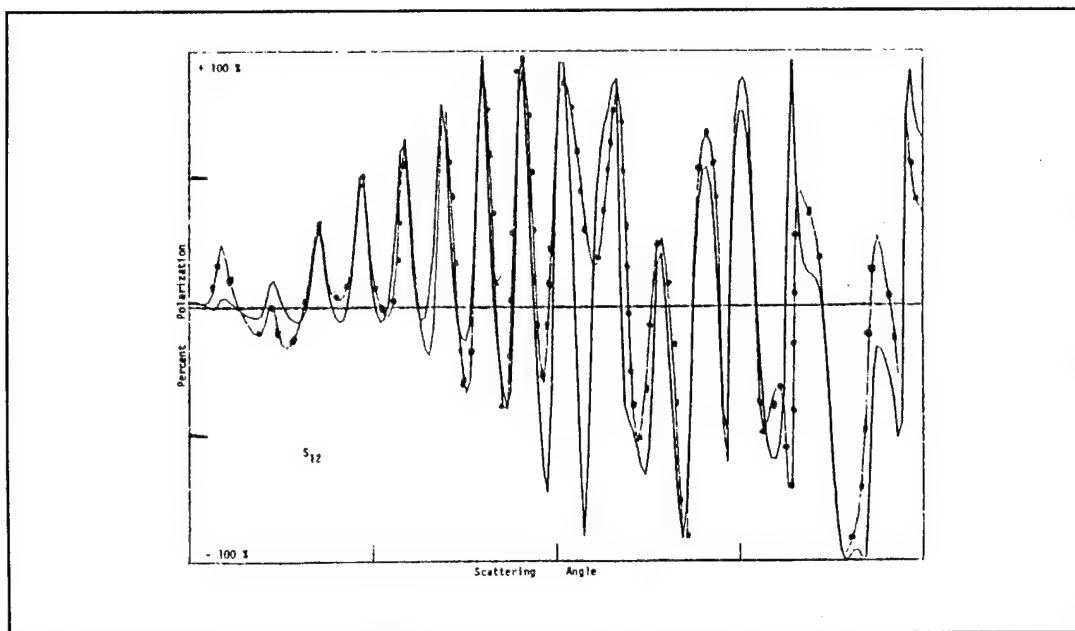


Figure 6.2.5. The Theoretical  $S_{12}^*$  Scattering Curves for a 1.3740  $\mu\text{m}$  Quartz Fiber with No Cladding and a 10 nm Thick Water Layer. The curve with the dots overlaid corresponds to the fiber with no water sheath.

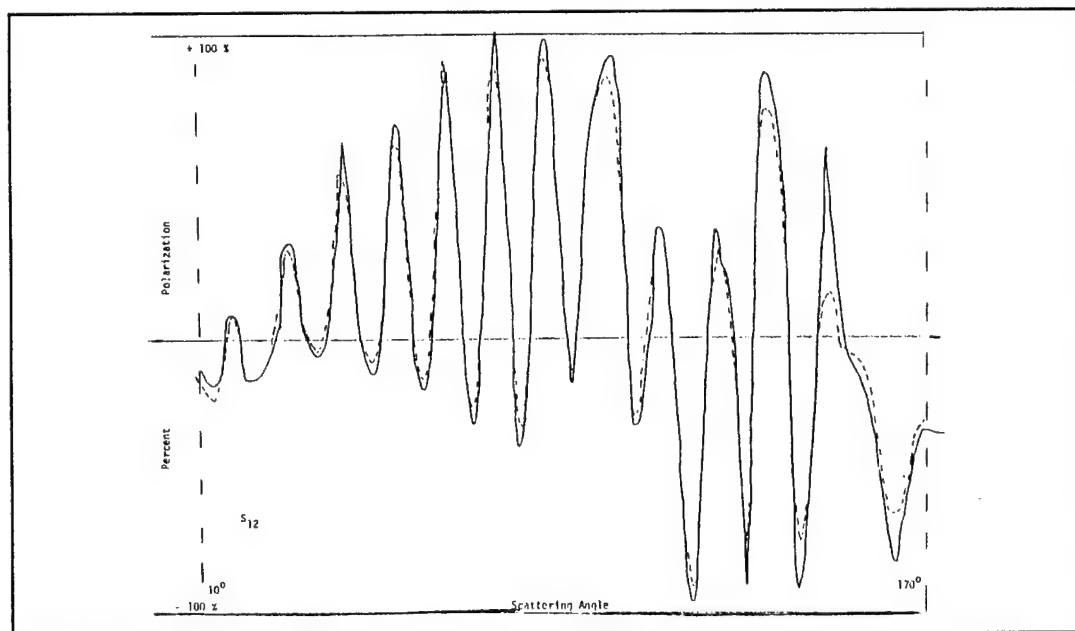


Figure 6.2.6. The Experimental  $S_{12}^*$  Scattering Curves for Fiber D Cleaned in Acetone and Exposed to High Static Humidity. The solid line is the scattering curve for the clean fiber, and the dotted line is the scattering curve for the fiber after its mount was filled with water. In both cases, the quartz chamber was in place attached to the fiber mount.

measurements using the wet nitrogen and Fiber C are shown in Figures 6.2.7 and 6.2.8. These curves are compared with the theoretical  $S_{ij}$  for an unclad 1.3525  $\mu\text{m}$  fiber and the same fiber with a 2.5 nm and 5.0 nm water sheath thickness, shown in Figure 6.2.9. Figure 6.2.7, shows two sets of  $S_{ij}$  for Fiber C: one at 15% RH and one at 96.5% RH. The sheath thickness is 4 nm. Figure 6.2.8 also shows two sets of  $S_{ij}$  for Fiber C: one at 15% RH, and one at 15% RH after the fiber was exposed to 95% RH twice. Figure 6.2.8 is almost identical to Figure 6.2.7.  $S_{33}^*$  and  $S_{34}^*$  indicate that all of the adsorbed water remained on the fiber, even after the chamber was flushed with dry nitrogen. Using data from all  $S_{ij}$  in Figure 6.2.8 gives a value of 3 nm for the sheath thickness.

Fiber D was given a water sheath with oxygen as the carrier gas. Figure 6.2.10 shows two  $S_{ij}$  for Fiber D: one at 28% RH (solid line) and one at 98.5% RH at a high flow rate (16.6  $\text{cm}^3/\text{min}$ , dashed line). The  $S_{ij}$  in the backscatter changes by as much as 50%. Since the experimental  $S_{ij}$  fit between the curves of the 5.0 nm water sheath in Figure 6.2.4 and the 10 nm water sheath in Figure 6.2.5, we estimate the water sheath thickness at 8 nm.

Figure 6.2.11 shows that sheath thickness does not decrease to zero after the humidity is reduced because many of the peaks, especially in the backscatter, do not return to their original polarization when the chamber is flushed with dry nitrogen. We estimate the water sheath thickness to be 2-3 nm.

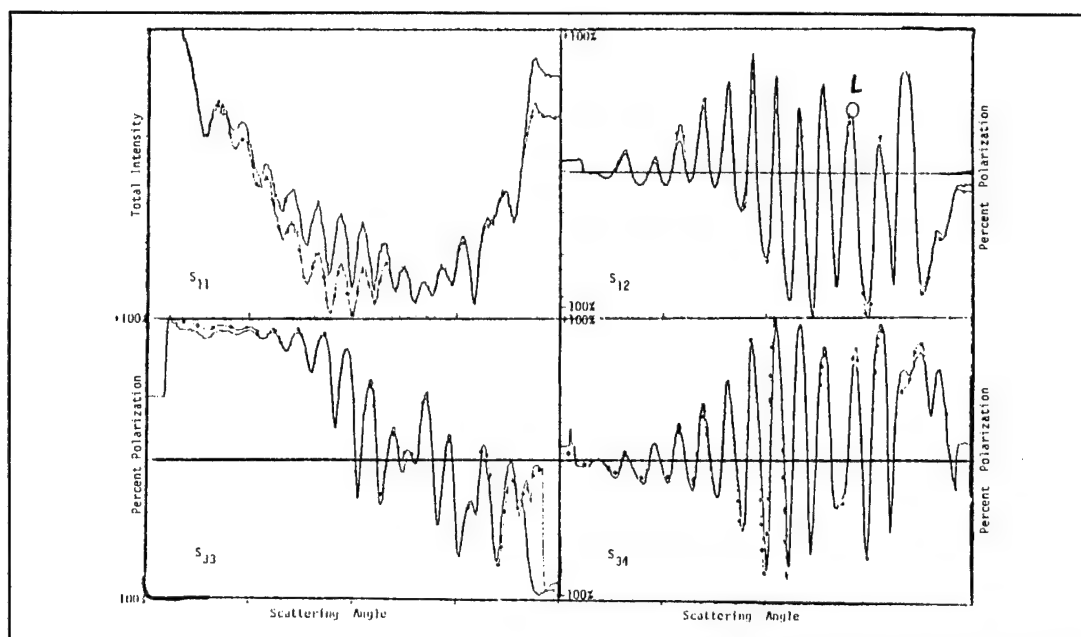


Figure 6.2.7. The Four Experimental Scattering Curves for Fiber C Exposed to 15% RH and 96.5% RH. The curves with the dots overlaid are the ones representing the fiber in the low humidity environment.

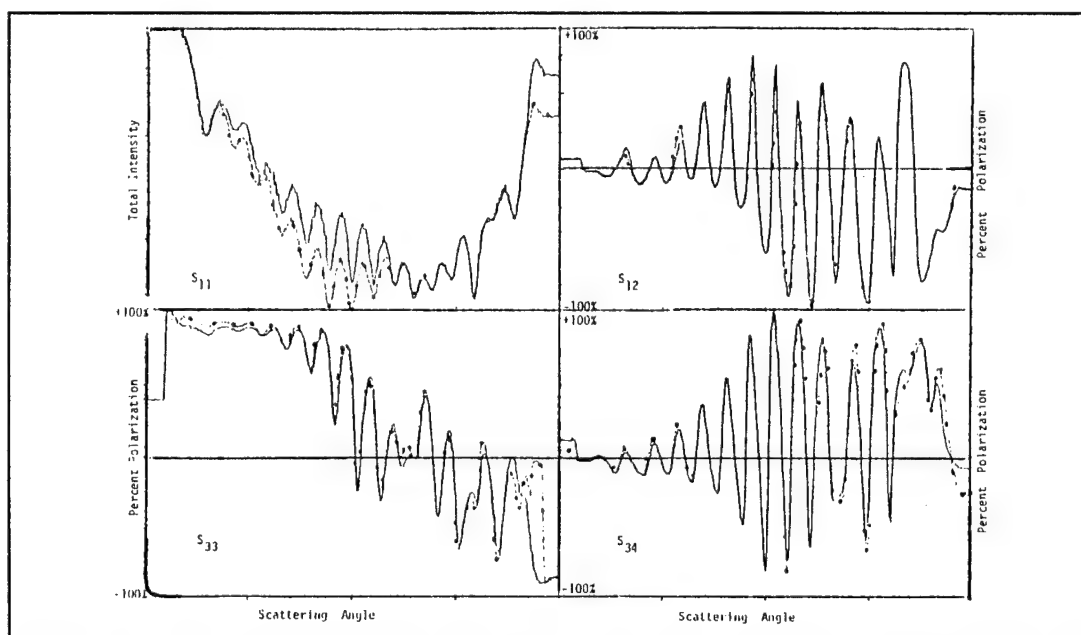


Figure 6.2.8. The Four Experimental Scattering Curves for Fiber C Exposed to 15% RH Initially and 15% RH After Two Consecutive 95% RH Exposures. The curves with the dots overlaid represent the fiber before exposure to high humidity.

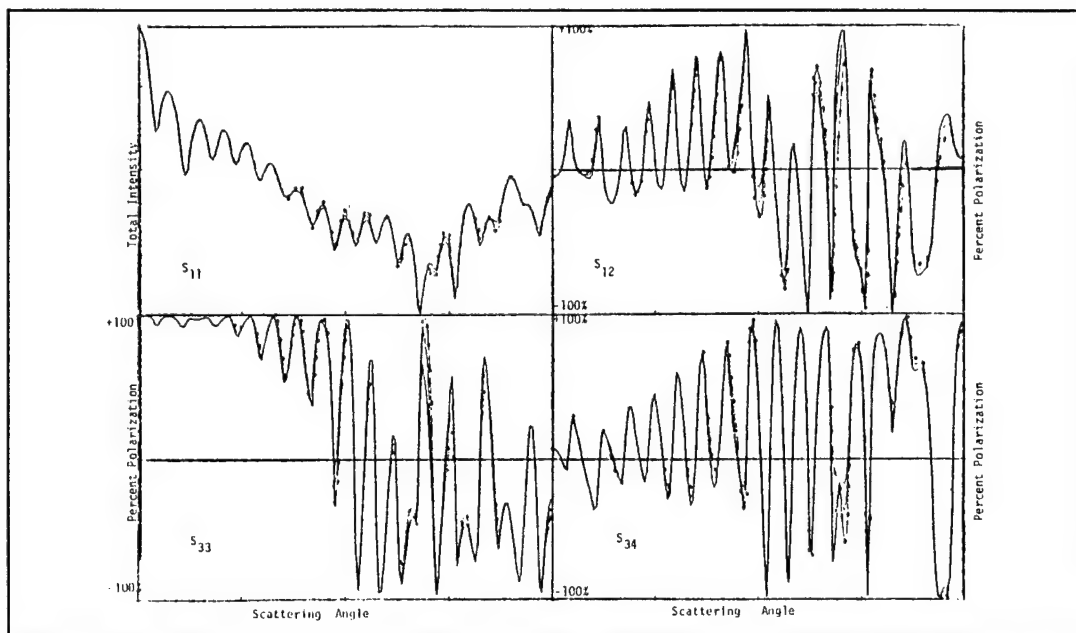


Figure 6.2.9. The Four Theoretical Scattering Curves for a 1.3525 μm Quartz Fiber with No Cladding, a 2.5 nm and a 5.0 nm Thick Water Layer. The curves with the dots overlaid are the ones representing the unclad fiber. The curves corresponding to the fiber with the 2.5 nm layer show small deviations, and the curves corresponding to the 5.0 nm layer show larger change.

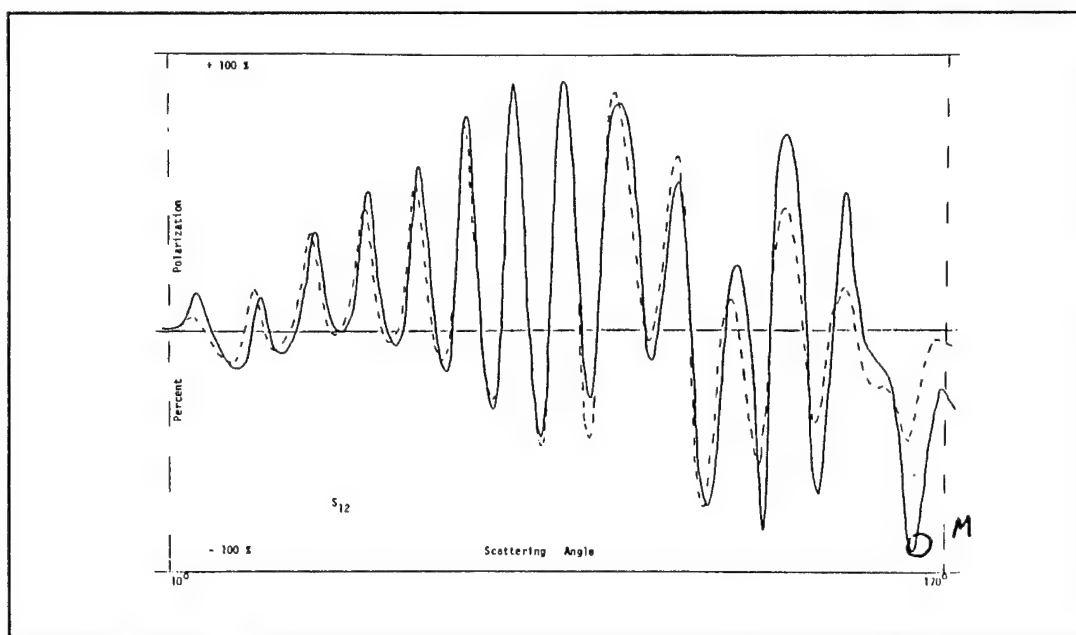


Figure 6.2.10. The Experimental  $S_{12}^*$  Scattering Curves for Fiber D Exposed to 28% RH and 98% RH. The dashed curve represents the fiber at 98% RH.

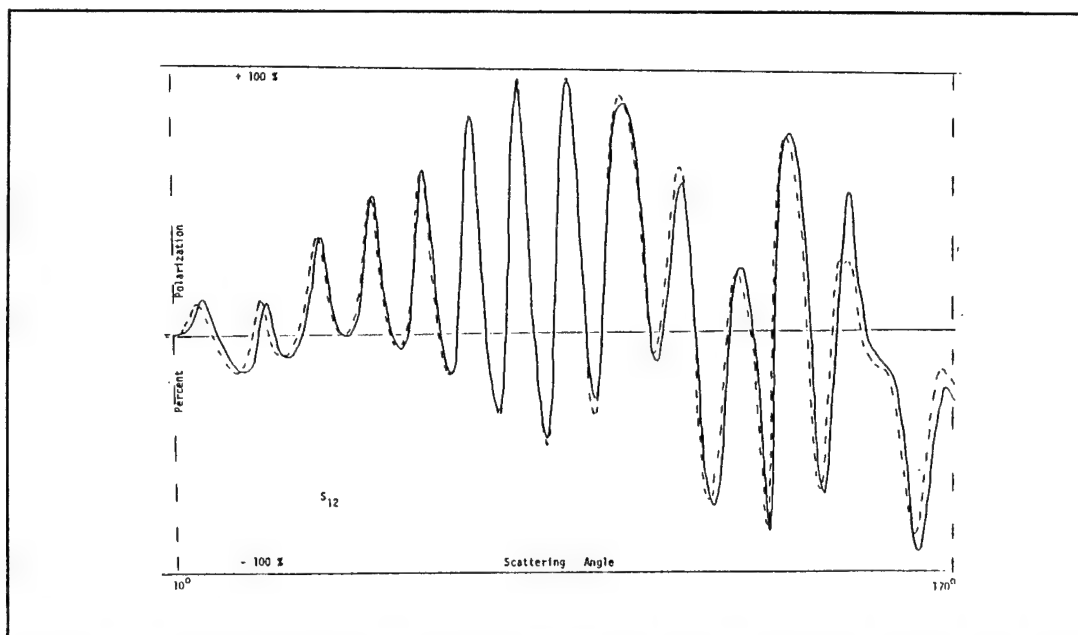


Figure 6.2.11. The Experimental  $S_{12}^*$  Scattering Curves for Fiber D at 20% RH Initially and 37% RH After a 98.5% RH Exposure. The dashed curve represents the fiber after the exposure to 98% RH.

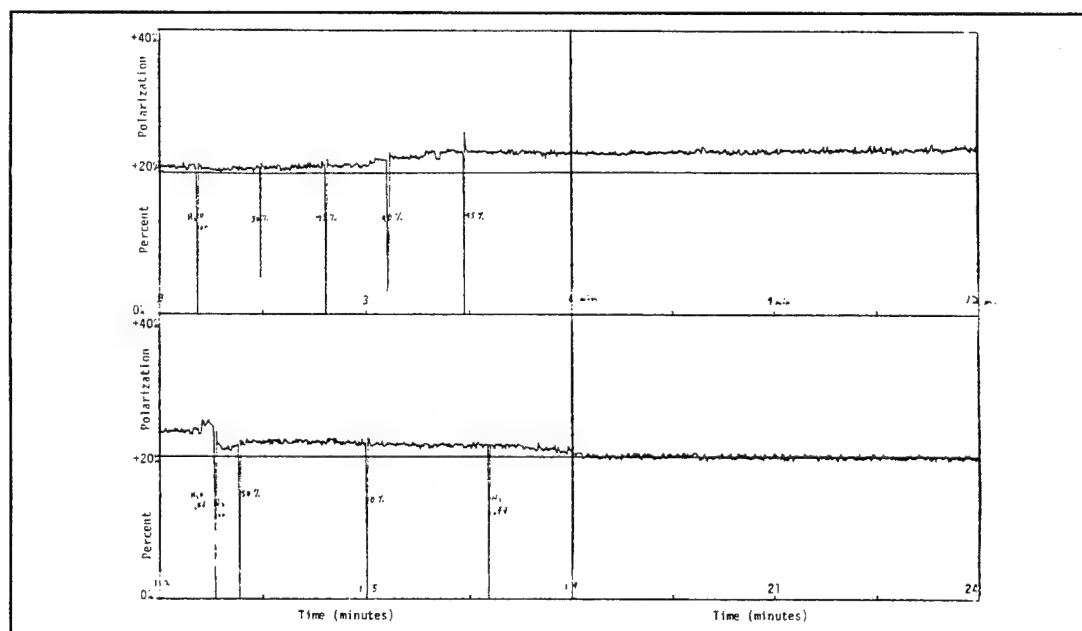


Figure 6.2.12. The  $S_{12}^*$  Percent Polarization Response of Fiber C at  $\theta = 131^\circ$  to Variable Humidities. The instantaneous values for the humidity are given at the spikes in the polarization curve.

#### 6.2.4 Percent Polarization at a Set Angle as a Function of Humidity

We conducted these measurements in the same way described in section 6.1.4. The peak at  $\theta = 131^\circ$ , the most sensitive angle for changes in Fiber C's radius, was isolated and marked with an L in Figure 6.2.7. Figure 6.2.12 shows how the  $S_{12}^*(\theta = 131^\circ)$  varied with humidity. Figure 6.2.13 shows  $S_{ij}$  as a function of relative humidity corrected for the lag in the probe detection. The approximate thickness of the water sheath thickness is listed on the right of the graph. The water sheath thickness shows a hysteresis with increasing and decreasing humidity; that is, the water sheath remains on the fiber at lower humidities if the humidity is decreasing from a maximum.

The process was repeated for Fiber D (1.3890  $\mu\text{m}$ ) using oxygen instead of nitrogen as the carrier gas. Figure 6.2.10 identifies the point M on  $S_{12}^*(\theta = 170^\circ)$  as an active angle. We show the  $S_{ij}$  as a function of relative humidity and flow rate. Figure 6.2.14 shows the variation of sheath thickness with relative humidity. A hysteresis is evident. In addition, the growth or decay of the sheath is accelerated beginning at about 90% RH. Figure 6.2.15 shows the variation of the sheath thickness with gas flow. A hysteresis is also evident here. The water sheath is thicker at a given flow rate if the rate is being decreased instead of increased. For example, during the first cycle of Fiber D in wet oxygen (indicated by the solid line in Figure 6.2.15), the sheath thickness was 5 nm when the flow rate was being increased through 6.6  $\text{cm}^3/\text{min}$ , but was about 7.5 nm when the flow was being decreased through the same flow rate. Therefore, a previously adsorbed layer has a tendency to remain thick, even if drier gas is flowing through the chamber.

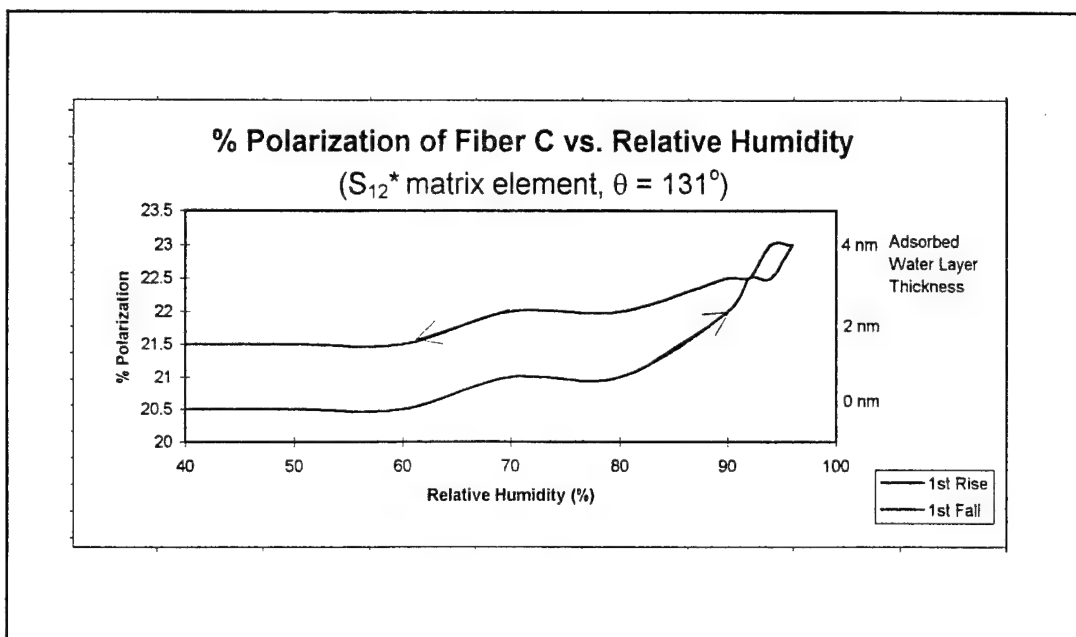


Figure 6.2.13. The Corrected  $S_{12}^*$  Percent Polarization Response of Fiber C at  $\theta = 131^\circ$  to Variable Humidities.

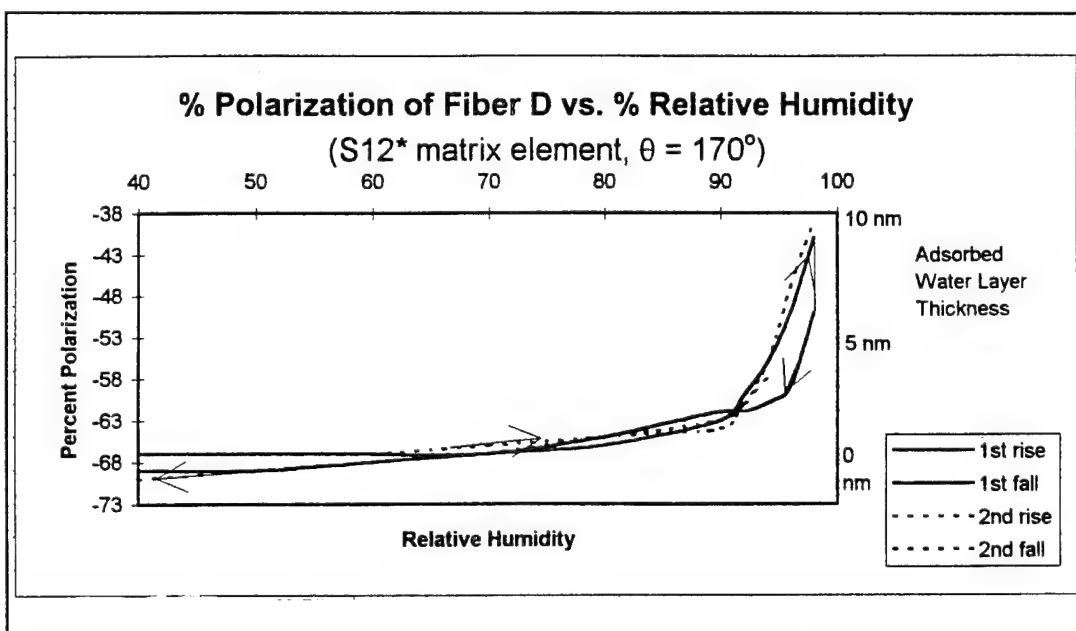


Figure 6.2.14. The Corrected  $S_{12}^*$  Percent Polarization Response of Fiber D at  $\theta = 170^\circ$  to Variable Humidities.

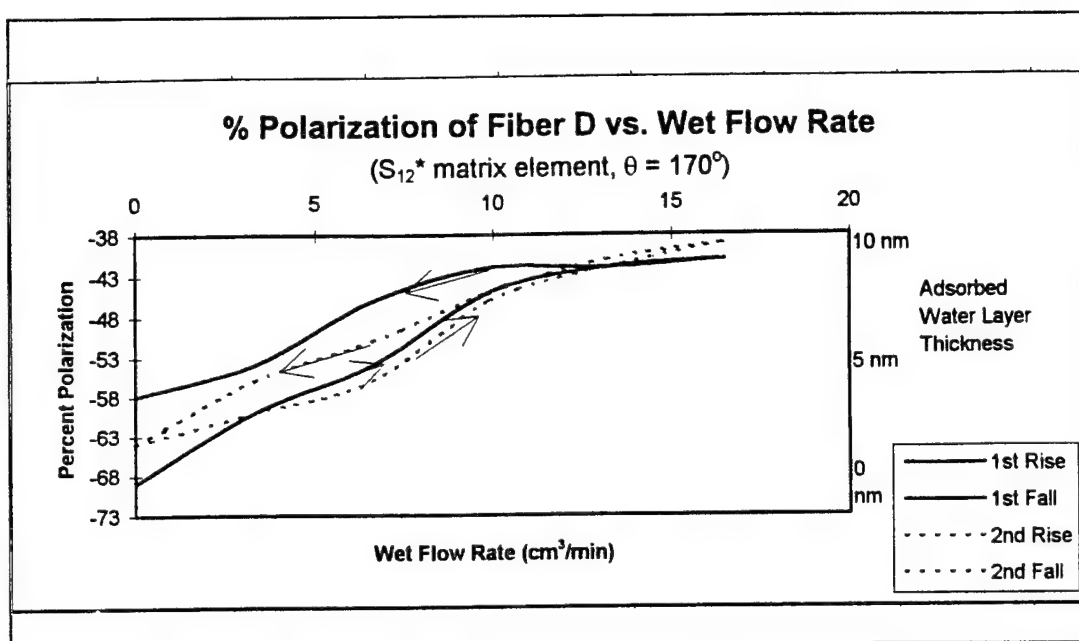


Figure 6.2.15. The Corrected  $S_{12}^*$  Percent Polarization Response of Fiber D at  $\theta = 170^\circ$  to Variable Flow Rates.

### 6.3 The Thin Fiber (Fiber X, 0.6280 $\mu\text{m}$ )

We measured the  $S_{ij}$  as before and matched them against various theoretical  $S_{ij}$ . Figure 6.3.1 shows the experimental  $S_{ij}$ , and Figure 6.3.2 the theoretical  $S_{ij}$  for scattering from a  $0.6280 \pm 0.0003 \mu\text{m}$  quartz fiber, the best fit to the experimental  $S_{ij}$ . The experimental  $S_{12}^*$  is used in all of the remaining measurements in this chapter and its theoretically determined fiber radius will be used for all of the sheath thickness modeling.

### 6.3.1 Water Layer Thickness due to Direct Exposure

Figure 6.3.3 shows how the  $S_{12}^*$  of Fiber X changed after being dipped in purified water. A significant change occurs at  $\theta = 120^\circ$ , where a peak amplitude shifts toward the backscatter region and grows by about 15%. Figure 6.3.4 gives the theoretical  $S_{12}^*$  corresponding to a 0.6415  $\mu\text{m}$  fiber with a 2.5 nm and a 5.0 nm water layer, but the  $S_{12}^*$  from the same theoretical fiber with a 10 nm sheath thickness, shown in Figure 6.3.5, is much closer to matching the experimental  $S_{12}^*$ . We assign a sheath thickness of 9-10 nm.

### 6.3.2 Static Humidity Contribution to Sheath Thickness

Figure 6.3.6 shows the experimental  $S_{12}^*$  of Fiber X before and after the lid of the fiber mount was filled with purified water ( $\sim 94\%$  RH). The static humidity did not change the  $S_{ij}$  as much as directly dipping the fiber into the water. The largest change, about 10%, comes near  $\theta = 85^\circ$ . Comparison with the theoretical  $S_{ij}$  shown in Figure 6.3.4 indicates a sheath thickness of 2 nm.

### 6.3.3 Dynamic Humidity Contributions to Sheath Thickness

Only oxygen was used as a carrier gas for this fiber. Figure 6.3.7 shows two  $S_{12}^*$  for Fiber X: one at 21% RH (solid line) and one at 98% RH (dashed line). Point N shows the largest change, about 5%. Comparison of the two experimental  $S_{ij}$  with the theoretical  $S_{ij}$  in Figure 6.3.4 indicate a sheath thickness of 0.5 - 1 nm. Figure 6.3.8 shows two  $S_{12}^*$  for Fiber X: one at 40% RH (solid line) and one at 40% after a 98% RH exposure. The

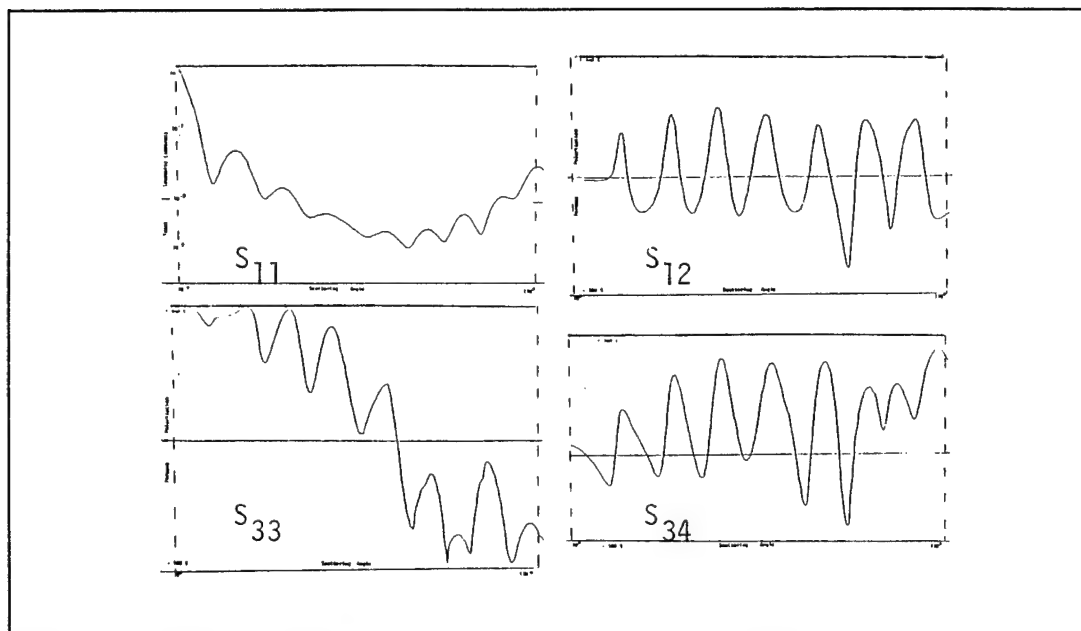


Figure 6.3.1. The Four Experimental Scattering Curves for Test Fiber X. The fiber was cleaned in acetone before the measurements were made.

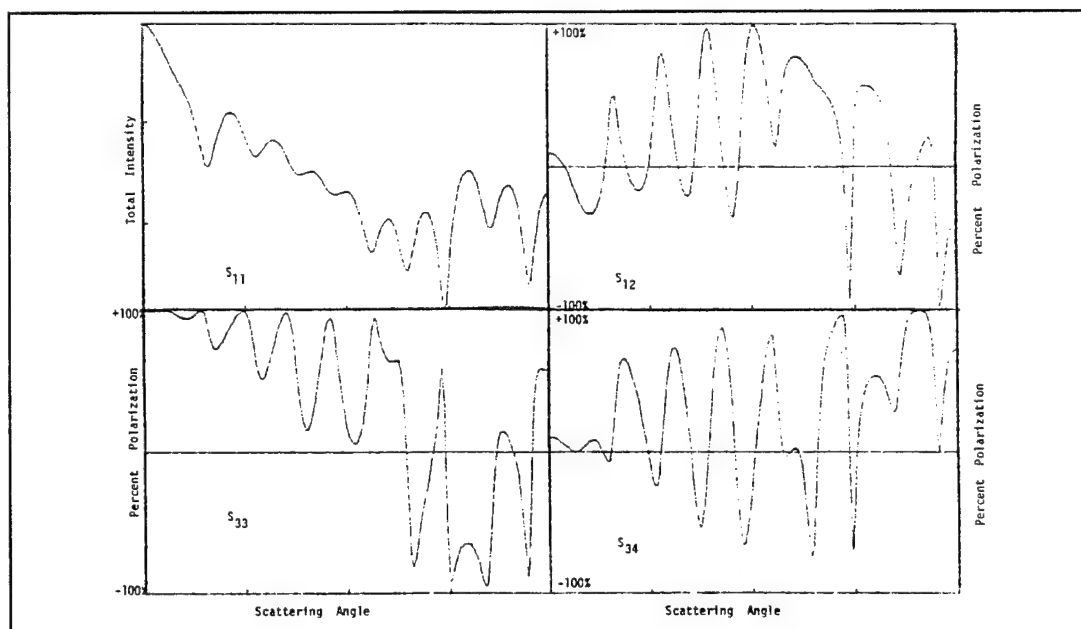


Figure 6.3.2. The Four Theoretical Scattering Curves for a 0.6280  $\mu\text{m}$  Quartz Fiber.

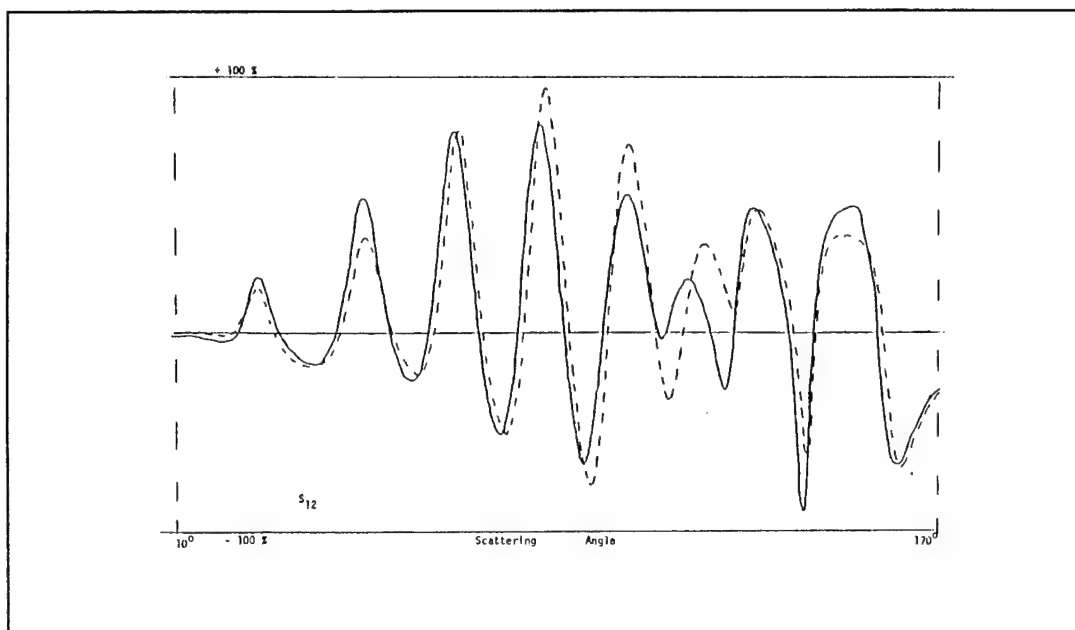


Figure 6.3.3. The Experimental  $S_{12}^*$  Scattering Curves for Fiber X Cleaned in Acetone and Dipped in Water. The dashed curve represents the fiber after being dipped in the water.

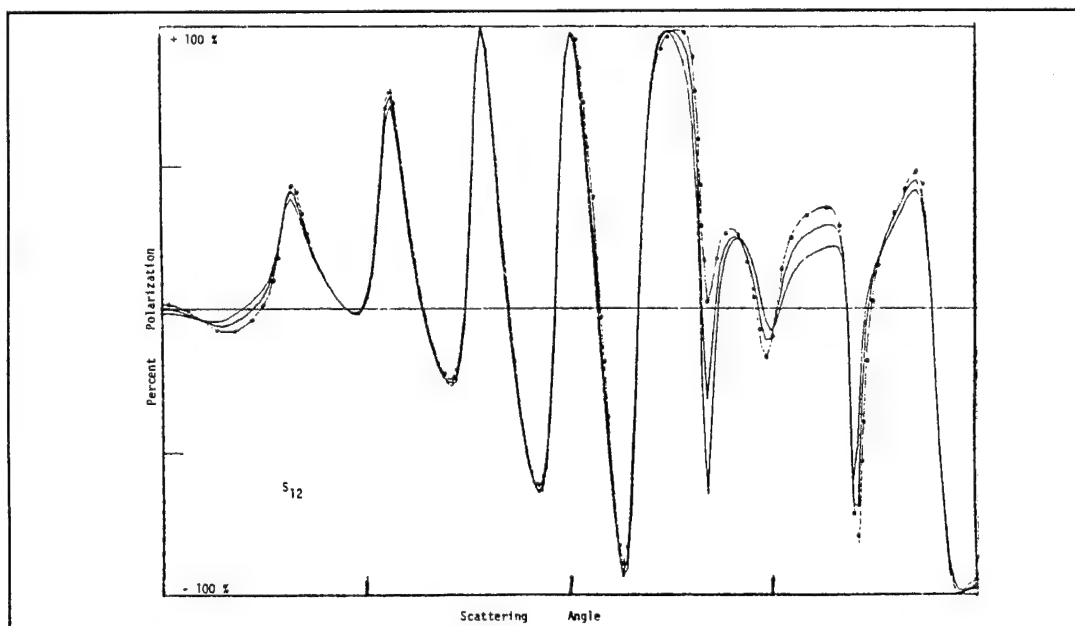


Figure 6.3.4. The Theoretical  $S_{12}^*$  Scattering Curves for a 0.6415  $\mu\text{m}$  Quartz Fiber with No Cladding, a 2.5 nm and a 5.0 nm Water Layer. The curve with the dots overlaid represents the unclad fiber, and the other curves represent the two degrees of coating. The more extreme changes are seen in the fiber with the larger coating.

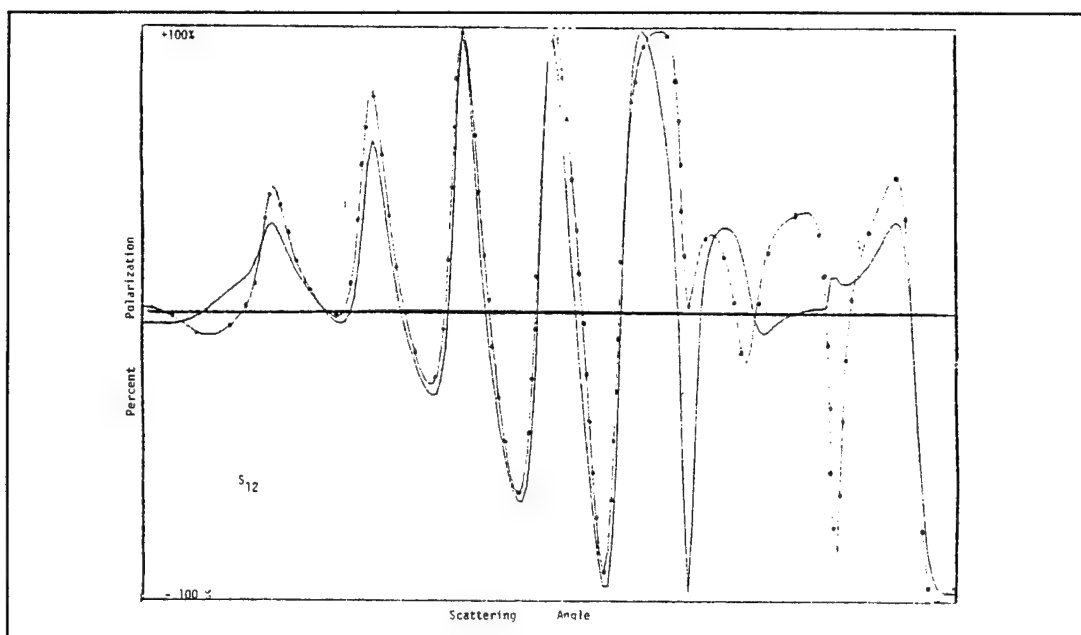


Figure 6.3.5. The Theoretical  $S_{12}^*$  Scattering Curves for a 0.6415  $\mu\text{m}$  Quartz Fiber with No Cladding and a 10 nm Thick Water Layer. The curve with the dots overlaid represents the unclad fiber.

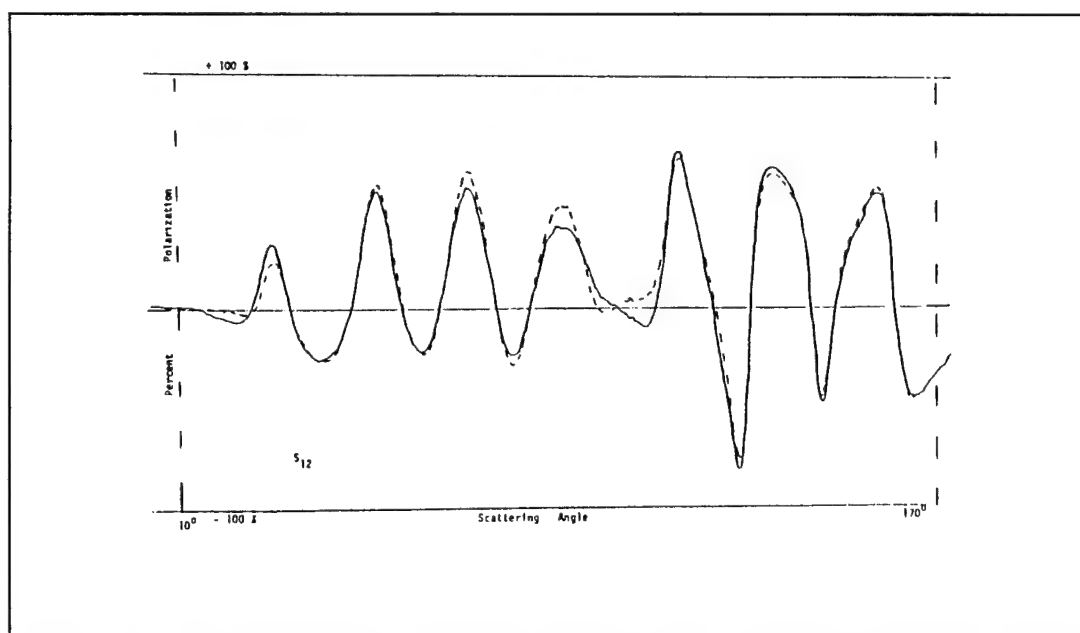


Figure 6.3.6. The Experimental  $S_{12}^*$  Scattering Curves for Fiber X Cleaned in Acetone and Exposed to High Static Humidity. The dashed curve represents the fiber exposed to high humidity.

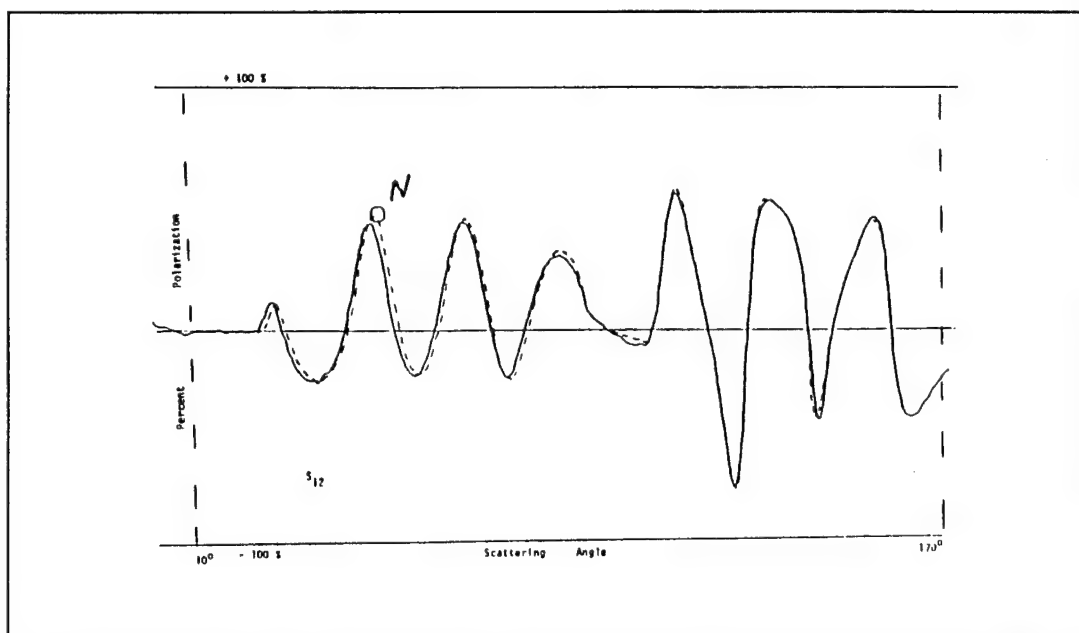


Figure 6.3.7. The Experimental  $S_{12}^*$  Scattering Curves for Fiber X Exposed to 21% RH and 98% RH. The dashed line is the curve for the fiber at 98% RH.

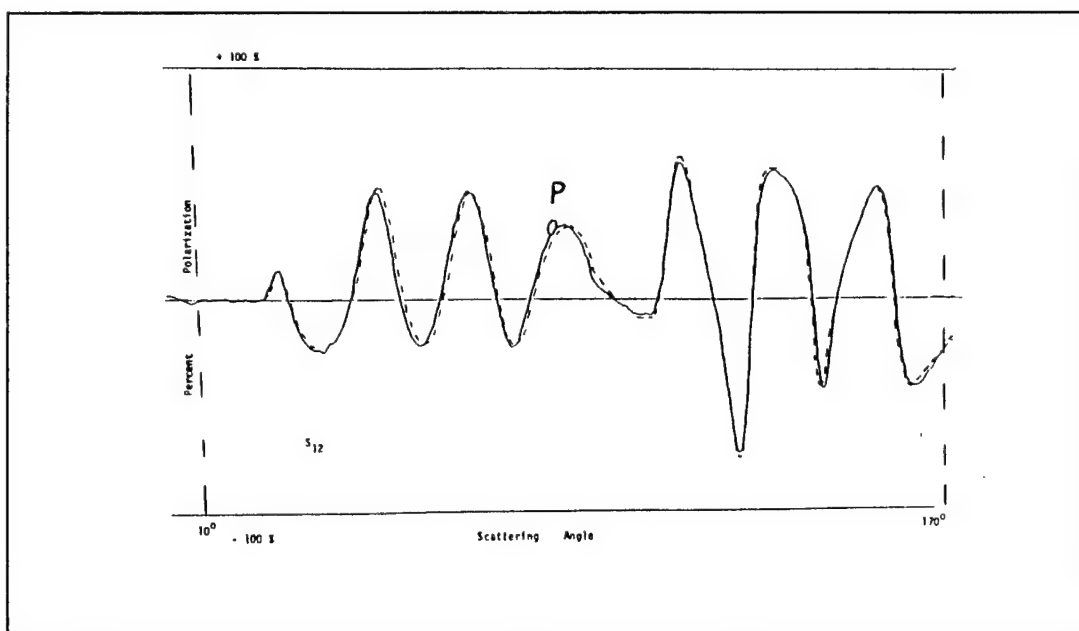


Figure 6.3.8. The Experimental  $S_{12}^*$  Scattering Curve for Fiber X at 20% RH Initially and 18% RH After a 98% RH Exposure. The dashed line is the curve for the fiber which was exposed to 98% RH.

curves indicate that the sheath thickness does not change. In both cases, the measured sheath thickness approaches the minimum resolution of the nephelometer system (0.5 nm).

#### 6.3.4 Percent Polarization at a Set Angle as a Function of Humidity

Few regions over  $S_{12}^*$  for Fiber X showed any significant change as a function of humidity. The angle selected for measurement is marked as point P in Figure 6.3.8 ( $\theta = 85^\circ$ ). Figures 6.3.9 and 6.3.10 do not indicate any significant changes in sheath thickness, but they do show that, at certain humidities and flow rates, small water sheaths appeared. Figure 6.3.9 shows that a 1 nm water sheath begins forming at about 90% RH, but does not fully come off until about 70% RH. Figure 6.3.10 shows a sheath thickness which builds when the gas flow is  $6.5 \text{ cm}^3/\text{min}$ , but does not come off until the flow is reduced to  $4.4 \text{ cm}^3/\text{min}$ .

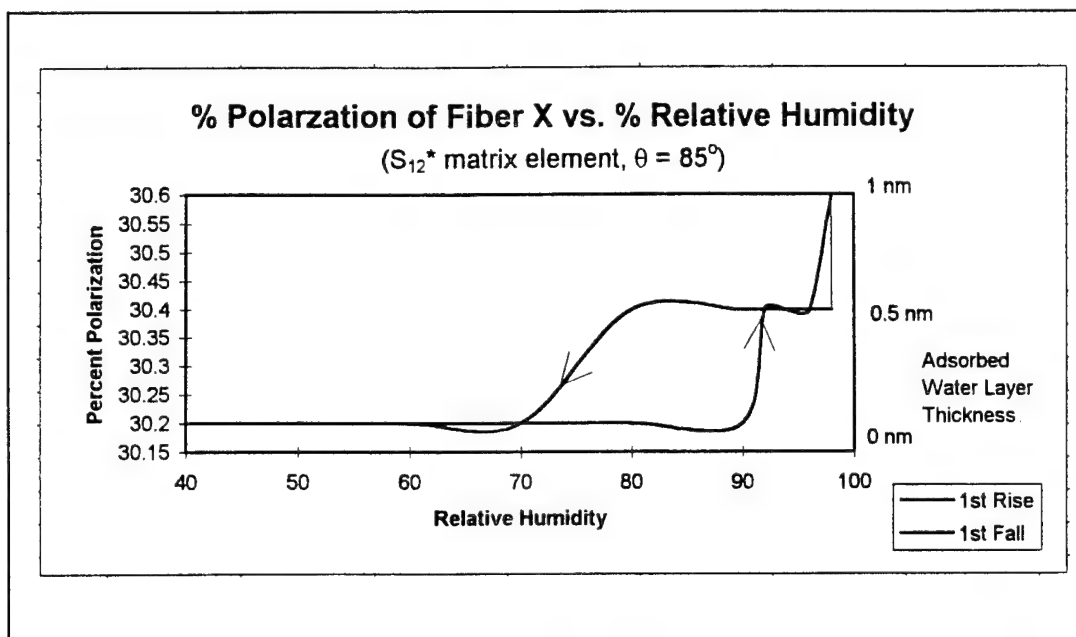


Figure 6.3.9. The Corrected  $S_{12}^*$  Percent Polarization Response of Fiber X at  $\theta = 85^\circ$  to Variable Humidities.

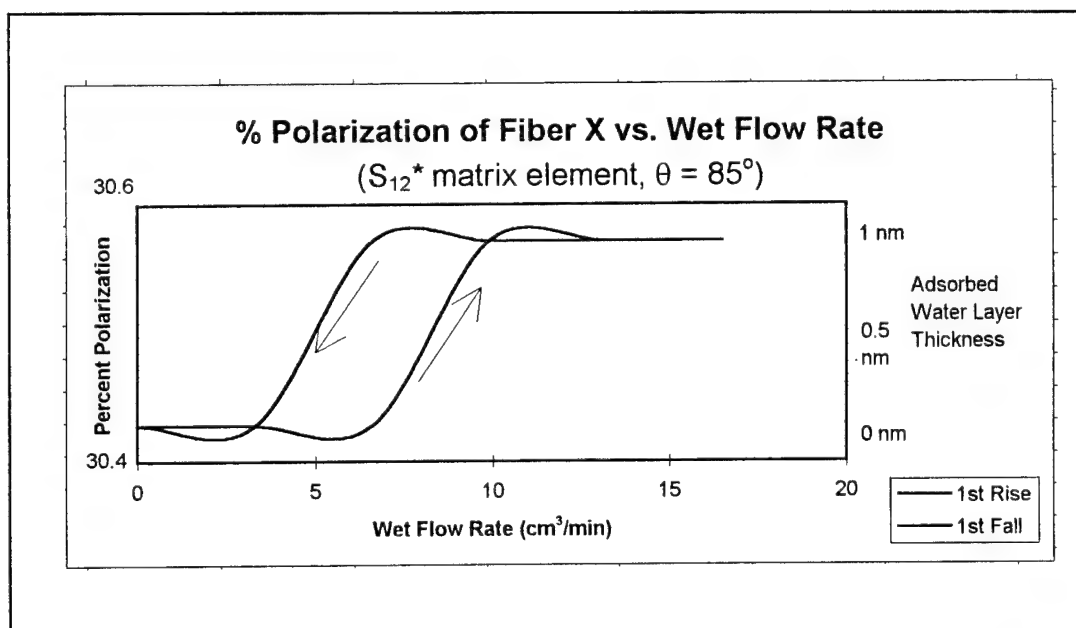


Figure 6.3.10. The Corrected  $S_{12}^*$  Percent Polarization Response of Fiber X at  $\theta = 85^\circ$  to Variable Flow Rates.

## CHAPTER 7

### CONCLUSION

One of the initial goals of this experiment was to repeat the data obtained by Wentzel and measure water sheath thickness as a function of relative humidity for several different sized fibers. Our preliminary work shows that a 640 nm fiber gained a sheath thickness of barely one-half of a nanometer, even at the maximum flow rates and humidities available, while a 1.3890 nm fiber gained a sheath thickness of almost 10 nm under the same conditions. Figure 7.1 shows the curves for water sheath thickness as a function of relative humidity for a planar surface (Fisher, *et al.*), the 0.62  $\mu\text{m}$  fiber that Wentzel used, and the four fibers of different sizes which we used. Our fibers did not accumulate water sheaths as large as Wentzel's, and nowhere near as large as Fisher's planar surface.

There are a number of possible explanations for this. A significant possibility is that there are variables in this experiment which have not been accounted for. The first and most obvious one discovered in the course of these experiments is the wet gas flow rate. Higher flow rates always gave thicker water sheaths. Evidently the flow rate affects the relative humidity near the fiber in a way the Vaisala probe does not record.

We attempted using a commercial humidifier at one point to increase the relative humidity at the fiber. Our carrier gas systems changed the liquid water into a vapor while

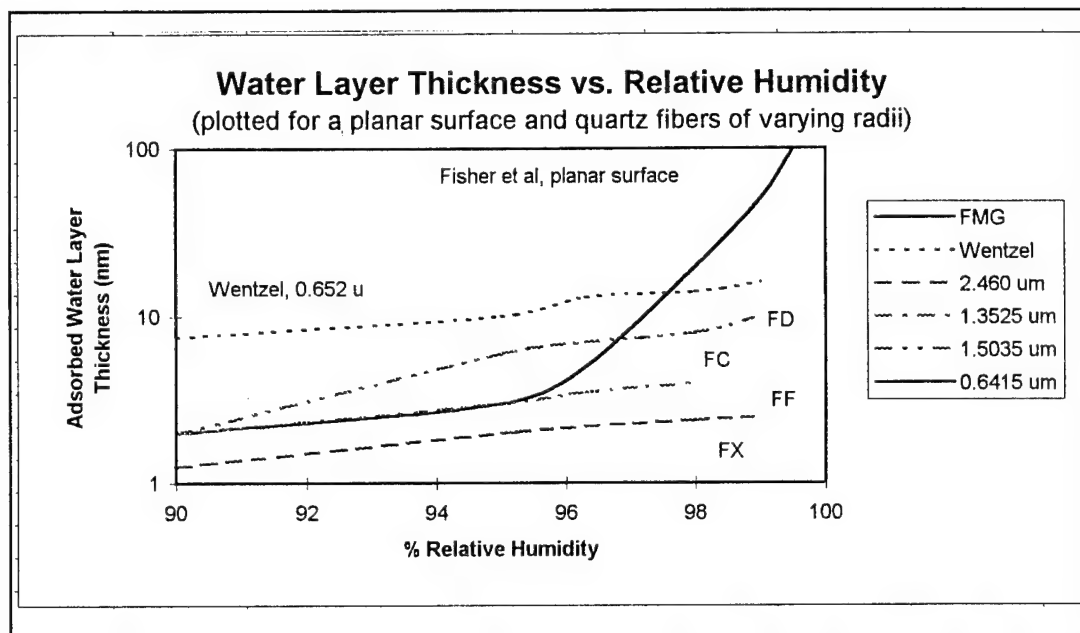


Figure 7.1. Adsorbed Water Layer Thickness as a Function of Relative Humidity for a Planar Surface and Quartz Fibers of Different Radii. The letters to the right of the lower four curves refer to the test fibers used in this project. Fiber X is on the x-axis.

transporting it to the chamber. A humidifier throws microscopic droplets of liquid water into the air, pulling the water out of a well and spinning it in a centrifuge. The humidifier could create only a 75% RH at the fiber, but the fiber (Fiber D, 1.3890  $\mu\text{m}$ ) still gained a water layer comparable to those accumulated near 93% with the oxygen carrier gas. The largest differences between the humidifier and our carrier gas sources are temperature and the method of vapor production. Higher temperatures tended to increase the sheath thickness on the fiber, so if the vapor temperature was the key variable, the humidifier should have been less effective at increasing the sheath thickness than the our carrier gas source. The humidifier, however, produces droplets which are still in liquid form. There

is a large difference between a water molecule in a liquid and a gaseous state, as discussed in Chapter Five. Possibly, water droplets adhere to surfaces more readily than water vapor.

Figure 7.2 is a summary of the water sheath thicknesses for each of the experiments done with the fibers. Each fiber retained a relatively large water sheath thickness after being dipped in purified water. In fact, Fiber X, the fiber with the worst performance after

Fiber Name	Size (um)	Adsorbed Water Layer (nm)			
		Direct Appl.	Water in Lid	Low / High Humid.	Before/After Exp
F	2.460	8.0	2.0	1.75 (N <sub>2</sub> ) 2.25 (O <sub>2</sub> )	1.5 (N <sub>2</sub> ) 1.0 (O <sub>2</sub> )
D	1.3890	10.0	6.5	8.0 (O <sub>2</sub> )	2.5 (O <sub>2</sub> )
C	1.3525	n/a	n/a	4.0 (N <sub>2</sub> )	3.0 (N <sub>2</sub> )
X	0.6415	9.5	4.0	0.75 (O <sub>2</sub> )	0.75 (O <sub>2</sub> )

Figure 7.2. Summary of Findings Involving Three Sizes of Test Fibers Receiving Water Layers by Various Means. O<sub>2</sub> and N<sub>2</sub> refer to the humidity systems which used oxygen and nitrogen as the carrier gases.

being coated in the humidity experiments, had the best performance in terms of the ratio of water sheath thickness to core radius when it was dipped directly in water (14.6 nm water per micron radius, as opposed to 7.2 for Fiber D and 3.2 for Fiber F). After being dipped in water, the fibers were exposed to the ambient 25% RH of Arizona air, which

undoubtedly removed some of the water. A high humidity environment would preserve the initial coating that the fibers receive. Therefore, regardless how a fiber obtains a water sheath, the water sheath will remain.

Figure 7.2 shows data obtained by placing water in the lid of the humidity chamber - a situation much like the calibration jars for the Vaisala probe without salts. The relative humidity of the air a very short distance from the surface of the water is, by definition, 100%. When measured with the Vaisala probe, the humidity at the fiber's position was about 94% RH. There is a marked difference between the water layers on the three fibers. The intermediate fiber seems to accept thicker water sheaths from static humidity than the other two fibers. This is an odd result, because the theory in Chapter Five predicts that the thickest fiber, having the lowest radius of curvature, would take the largest water layer, since it was a more planar surface. However, the smallest fiber still gains a water sheath which is comparable in terms of a cladding-to-core ratio.

The most effective humidity system (that is, the one that caused the most coating of the fiber) consisted of a beaker with heater and a second container through which the vapor and gas mixture were bubbled. Agitation of the water probably caused liquid droplets to fly free of the water and flow a short way down the rubber hose toward the chamber. If they reached the chamber, they would join the vapor particles in coating the fibers. The bubbling agitation may have an effect like that of the humidifier since higher flow rates always caused larger sheath thicknesses on the fiber. This would indicate that

water molecules, bound together in small liquid droplets are more prone to bind to surfaces than actual water vapor.

There are still some mysteries. We do not know why the intermediate fiber accepts a larger water sheath than fibers larger or smaller than it. The cladding to core ratio described earlier favors Fiber D for the dynamic humidity case, despite the fact that the thinnest fiber showed the best cladding to core ratio for water sheath thickness after dipping the fiber in water. There could be a "resonance" fiber radius where the fiber will build the thickest water sheath. There is certainly more research to do in this area. The first step would be to use humidity systems which generate different types and sizes of airborne water, such as the commercial humidifier. Different carrier gases such as carbon dioxide or sulfur hexafluoride have different levels of water solubility and viscosity. In any case, light scattering techniques make these measurements possible, and will certainly continue to do so in the study of small particles and systems.

## REFERENCES

- Barrett, Harrison, Class Notes, Mathematical Methods for Optics (Optical Sciences 504), Dept. of Optical Sciences, U. Arizona (Fall 1994).
- Bickel, William S. and Bailey, Wilbur M., "Stokes Vectors, Mueller Matrices, and Polarized Scattered Light," *Am. J. Phys.* **53**, 468 (1984).
- Bickel, William S., Davidson, J.F., Huffman, D.R. and Kilkson, R., "Application of Polarization Effects in Light Scattering: A New Biological Tool," *Proc. Nat. Acad. Sci. USA* **73**, 486 (1976).
- Bickel, William S. and Stafford, Mary E., "Biological Particles as Irregularly Shaped Particles," *Light Scattering by Irregularly Shaped Particles*, ed. Donald W. Schuerman (Pienum Publishing Co., 1980).
- Fisher, L.R., Gamble, R.A., and Middlehurst, J., "The Kelvin Equation and the Capillary Condensation of Water," *Nature* **290**, 575 (1981).
- Gilliar, Wolfgang G., Bickel, William S., and Bailey, Wilbur F., "Light Diffraction Studies of Single Muscle Fibers as a Function of Fiber Rotation," *Biophys. J.* **45**, 1159 (1984).
- Gilliar, Wolfgang G., Bickel, William S., Videen, Gordon, and Hoar, David, "Light Scattering from Fibers: An Extension of a Single-Slit Diffraction Experiment," *Am. J. Phys.* **55**, 555 (1986).
- Hecht, Eugene, *Optics*, 2nd ed. (Addison-Wesley, Reading Massachusetts 1987).

Hobbs, Peter V. and Wallace, John M., *Atmospheric Science: An Introductory Survey* (Academic Press, San Diego 1977).

Hsu, Jiunn-Yann, "The Polarized Light Scattering Matrix Elements for Rough Surfaces," M.S. Thesis, Dept. of Physics, U. Arizona (1992).

Iafelice, Vincent J., "The Polarized Light Scattering Matrix Elements for Select Perfect and Perturbed Surfaces," M.S. Thesis, Dept of Physics, U. Arizona (1985).

Jackson, John David, *Classical Electrodynamics*, 2nd ed. (Wiley, New York 1975).

Vaisala Instruction Manual for Humidity Transmitter HMT 14 / Sensing Heads HMT 14 (Vaisala, Helsinki Finland 1981).

Wentzel, Thomas M., "Measurement of Adhesion Force Due to Condensed Water Vapor in a Crossed Fiber System," Ph.D. Thesis, Dept. of Physics, U. Arizona (1994).